Title

Mechanisms of Energy Control and Failure in Neurodegeneration

Author

Liao, Szu-Chi

Publication Date

2024

Peer reviewed|Thesis/dissertation

Mechanisms of Energy Control and Failure in Neurodegeneration

By

Szu-Chi Liao

A dissertation submitted in partial satisfaction of the

requirements for the degree of

Doctor of Philosophy

in

Endocrinology

in the

Graduate Division

of the

University of California, Berkeley

Committee in charge:

Professor Ken Nakamura, Co-chair
Professor Gregory Aponte, Co-chair
Professor Helen Bateup
Professor Denis Titov

Summer 2024

Abstract

Mechanisms of Energy Control and Failure in Neurodegeneration

by

Szu-Chi Liao

Doctor of Philosophy in Endocrinology

University of California, Berkeley

Professor Ken Nakamura, Co-chair

Professor Gregory Aponte, Co-chair

Energy failure, or insufficient energy to maintain normal cellular functions, is implicated in numerous diseases, including cancer, degenerative diseases, and even aging. However, critical knowledge gaps still exist. First, the mechanisms through which cells maintain energy levels by balancing the two energetic pathways, glycolysis and respiration, remain to be elucidated. Second, the causative relationship between energy failure and disease pathogenesis needs to be established.

To gain insight into how energy levels are regulated, we performed CRISPRi-based screens to study the impact of cellular energy level under manipulations of a critical metabolic pathway, the HIF1 (hypoxia-inducible factor 1) pathway. Previously, our lab reported an unexpected normoxic function of the HIF1 pathway, which inhibits respiratory ATP production. Combining CRISPRi screening with metabolomics and Seahorse assays, we elucidated a prominent substrate diverting effect of HIF1 under normoxia and identified proteins critical to this metabolic shift, including a key neuronal protein implicated in neurodegeneration. This study not only provides vital mechanistic insight into cellular energy homeostasis, but also links energy imbalance and pathophysiology.

To investigate the role of mitochondrial dysfunction and energy failure in neurodegeneration, we also developed a new mouse model with a point mutation in the Parkinsonian gene CHCHD2. Considerable indirect evident supports a causative association between mitochondrial dysfunction and the pathophysiology of Parkinson's disease (PD). Mutations in the mitochondrial cristae protein CHCHD2, which cause a monogenic form of PD closely resembling sporadic PD, are considered critical for understanding this association. In this study, we extensively characterized the mouse model using histological analyses, metabolomics, spatial transcriptomics and proteomics. We identified a robust metabolic shift toward glycolysis, potentially secondary to mitochondrial dysfunction. Furthermore, the preferential protein aggregation in specific subpopulations of dopaminergic neurons suggests mechanisms of selective vulnerability.

Altogether, these studies provide new insights into the mechanisms of cellular energy homeostasis and failure, and support the causative relationship between energy failure and PD. I also anticipate that this work will lay the groundwork for developing novel

therapeutic strategies for Parkinson’s disease and other energy failure-associated diseases.

Dedication

To my parents, who gave me all the opportunities they never got to have.

Table of Contents

List of Figures

Main Figures:

Chapter 2

Chapter 3

Supplementary Figures:

Chapter 2

Chapter 3

Acknowledgements

My Ph.D. journey from UC Berkeley to Gladstone has been challenging, but I was fortunate to receive support from numerous incredible people who nourished me along the way. I am deeply be grateful for their contributions.

I would like to express my heartfelt thanks to my advisor, Dr. Ken Nakamura, who gave me a chance when I was facing with the toughest times. His commitment to science, mentoring and education has profoundly inspired me. He guided me to become a well-rounded researcher, enabling me to reach my full potential. Despite his busy schedule, he always made time for trainees, doing his best to meet everyone's needs. I would not be where I am today without his dedication and support.

Many thanks to my thesis committee members, Dr. Gregory Aponte, Dr. Helen Bateup and Dr. Denis Titov, for their unwavering support and insightful feedback during our meetings. They also cared about my well-being, wishing me the best in my personal development.

I am sincerely grateful for the financial support I received during my Ph.D. — the Government Fellowship for Study Abroad (Ministry of Education, Taiwan), and the Dr. and Ms. James C.Y. Soong Fellowship (UC Berkeley). These fellowships have significantly relieved my financial burden, allowing me to concentrate on my research, and have been an invaluable contribution to my academic career.

I was very fortunate to be part of the Nakamura lab, which is the best lab I could have ever asked for. All the labmates I have worked with—Erica, Gwen, Huihui, Jonathan, Joyce, Katie, Kohei, Lillie, Mai, Megan, Mie, Neal, Saeed, Wole, Yanilka, Yoshi and Zak—are fantastic people. Our game nights will always be among the highlights of my grad student life.

I am particularly grateful to Monica, who took care of all the troublesome administrative work in the program. She is one of the nicest people I have ever met, putting her heart into taking good care of all the students. She is kind, courageous, and acts with integrity.

I can never fully repay my family and life partners. Being focused on research for so many years, there were times I failed to cover other duties in daily life. Jeffery and Yuri took care of every other aspect in my life, both physically or emotionally, providing an environment where I could fully devote myself to my studies. My parents, despite the distance, supported me wholeheartedly, filling my heart with strength and courage.

There are many others I cannot mention here, but I will always keep them in my thoughts. This dissertation was accomplished with the help of those around me, who have shaped me into who I am today.

Chapter 1: Energy Failure in Neurodegeneration

1.1 The energetic pathways

Cells produce energy through two primary pathways: glycolysis and mitochondrial respiration. Glycolysis is a series of reactions that rapidly converts glucose to pyruvate, generating 2 ATP molecules. The pyruvate can be converted into lactate and excreted from the cell, or enter the mitochondria as a substrate for respiration. In respiration, over 30 ATP molecules are produced with the consumption of oxygen. However, due to the complex reactions involved, this process takes much longer than glycolysis. Therefore, respiration is considered substrate-efficient, while glycolysis is time-efficient. Depending on the circumstances, a cell can rely solely on one of these pathways. For example, when oxygen is limited, cells significantly reduce respiration by the activation of the hypoxia-inducible factor 1 (HIF1) pathway and generate energy from glycolysis. Cells can also survive on respiration alone by taking up extracellular lactate or using substrates other than glucose, such as amino acids and fatty acids. However, the way energy homeostasis is achieved through the coordination between glycolysis and respiration is complicated and requires further elucidation.

1.2 The role of energy failure in aging and age-related diseases

Aging is characterized by a progressive decline in cellular functions and the systemic deterioration of multiple tissues, with mitochondria playing a central role in this process [1]. As people age, accumulations of mitochondrial DNA mutations and oxidative stress, impaired mitochondrial quality control, genomic instability and cellular senescence all contribute to mitochondrial functional decline. Interventions that improve mitochondrial health are strongly associated with increased lifespan [1-3]. As respiration, the primary energetic pathway, is a major function of mitochondria, a growing body of evidence suggests a close association between aging and age-related diseases and disruptions in energy homeostasis. For instance, glycolysis is commonly elevated in Parkinson's disease (PD) patients, likely as a compensatory response to impaired oxidative phosphorylation [4]. The expression levels of critical glycolytic regulators such as HIF-1α and hexokinase 2 (HK2) are also increased in the dopaminergic (DA) neurons of these patients [5]. In contrast, glycolysis is reported to be impaired in Alzheimer's disease (AD), where reduced glycolytic flux correlates with the severity of the disease [6]. Nonetheless, whether energy failure is a direct contributor to the death of these vulnerable neurons remains to be validated.

1.3 Parkinson's disease and mitochondrial dysfunction

Parkinson's disease (PD) is the second most common neurodegenerative diseases, affecting around 6 million people globally [7]. PD is primarily characterized by the degeneration of dopaminergic (DA) neurons in the substantia nigra (SN) of the midbrain. The axons of these DA neurons project to another brain region known as the striatum,

where they release dopamine as a neurotransmitter and mediate motor functions and reward-seeking behavior.

Considerable evidence suggests energy failure, particularly mitochondrial dysfunction, plays an important role in PD [8]. DA neurons are known to have high energy demands due to their long and extensive branching, and their role as pace-making cells [9, 10]. Growing evidence also shows DA neurons are specifically vulnerable to mitochondrial stressors [11], including exposure to complex 1 inhibitors (rotenone [12], MPTP [13]), and mutations in mitochondrial or mitochondria-related genes (Parkin [14], PINK1 [15], DJ-1 [16], CHCHD2 [17], α-synuclein [18-20] and LRRK2 [21]). In sporadic PD patients, decreased function of mitochondrial complex I [22], reduced expression of the master mitochondrial biogenesis regulator, PGC-1α, and its downstream genes [23, 24], and accumulated mitochondrial gene mutations [25] are commonly observed. Given these findings, mitochondria-related energy failure as a causative factor in PD pathogenesis has become a long-standing hypothesis yet to be determined.

1.4 Current knowledge gaps in energy control and failure in neurodegeneration

Current knowledge gaps in our understanding of energy control and failure in neurodegeneration include:

1. Achieving energy homeostasis: How do the glycolytic and respiratory pathways together achieve energy homeostasis? If one is compromised, how does the other compensate for the deficits, and through which mechanisms?
2. Direct contribution to neurodegeneration: Does energy failure directly contribute to neurodegeneration? Are mitochondrial deficits sufficient to induce dopaminergic neuron death in Parkinson's disease?

To address the first question, we conducted a mechanistic study using CRISPRi screenings in Chapter 2. We restricted cells to use only glycolysis or respiration, and observed how the ATP levels changed under perturbations of different metabolic genes. In Chapter 3, we developed a new mouse model with the Parkinsonian gene, CHCHD2, mutation, extensively analyzing its impact on mitochondrial metabolic functions and how it led to DA neuron malfunction.

Chapter 2: The Consequential Role of Tau and Glycolytic Enzymes in HIF1's Normoxic Repression of Respiration

2.1 Abstract

Insufficient or dysregulated energy metabolism may underlie a variety of inherited and degenerative diseases, but a comprehensive understanding of intracellular energy maintenance remains elusive. In our prior work, we utilized genome-wide CRISPR-based screenings to identify genetic regulators of ATP levels and define an "ATPome". Among our findings, we identified a robust and unexpected role of HIF1 in repressing respiratory ATP production under normoxia, a state where the HIF1 pathway is traditionally considered inactive.

To gain insight into how the HIF1 pathway regulates energy homeostasis, we conducted two complementary CRISPRi screenings under HIF1 activation or inhibition to identify HIF1 pathway-dependent genes and their relative positions upstream or downstream to HIF1. First, we examined the effects of concurrent knockdown of ATP-modulating genes and HIF1. Among our findings, we found that knocking down mitochondrial genes led to a further reduction in ATP level under HIF1 inhibition, indicating the necessity of an intact respiratory chain for the observed respiratory ATP-boosting effect. In contrast, HIF1 activation-alone resulted in a drastic decrease in respiratory energy production, with mitochondrial gene knockdown showing no impact on energy levels in this context. Notably, the knockdown of certain genes rescued respiratory ATP levels under HIF1 activation, suggesting their requirement for HIF1's action.

Collectively, our data suggest that the HIF1 pathway regulates intracellular energy under normoxia, possibly by directing substrate flux into lactate production or the TCA cycle. Furthermore, genes that maintain relatively high respiratory ATP levels when knocked down under HIF1 activation are likely crucial for the substrate-redirecting function of the HIF1 pathway. These studies will provide new insights into the regulation and effects of HIF1 activation on energy metabolism and could pave the way to the development of new therapeutic interventions for energy failure.

2.2 Introduction

Cells generate energy through either cytoplasmic glycolysis and mitochondrial respiration, and a failure to maintain energy levels by balancing these energetic pathways is implicated in numerous diseases. However, our knowledge of how energy is maintained in cells and the compensatory interactions between these two pathways is limited. Aiming to identify genes and pathways critical to intracellular energy balance, our lab previously conducted genome-wide CRISPR interference/activation screenings incorporated with an ATP biosensor [26]. By restricting cells to use either glycolysis or respiration for energy production, we identified genes and pathways that robustly regulate ATP levels using

different substrates. Collectively, this comprehensive metabolic map is defined as the “ATPome” [27].

In the study, K562 cells with stable integration of dCas9-KRAB (CRISPRi) and dCas9-Suntag (CRISPRa) were first transduced with lentivirus expressing the Clover-mApple FRET ATP sensor and subsequently with CRISPRi/a libraries. Immediately prior to fluorescence-activated cell sorting (FACS) based on ATP levels, cells were treated with acute stressors to force reliance on either respiration or glycolysis for ATP production. Through this screening, we identified individual genes critical to intracellular energy balance when using different substrates. For instance, knockdown of mitochondrial ribosomal proteins or respiratory chain components such as *NDUFA8*, *COX11* and *COX16* led to decreases in ATP levels under respiratory condition. Conversely, knockdown of several glycolytic genes, including *HIF1A*, *ARNT* and *HK2*, increased respiratory ATP levels. This reciprocal inhibition between glycolytic and respiratory pathways was further confirmed at a systems level via pathway analyses, with the hypoxia-inducible factor 1 (HIF1) pathway emerging as the most robust ATP booster when inactivated under respiratory condition.

This finding was exciting because one would expect the HIF1 pathway to be inactive under normoxia, where the screenings were conducted. The HIF1 signaling pathway is a specialized cellular adaptation to hypoxic environments. Under normoxia, the central player in the pathway, HIF-1α, senses oxygen and is hydroxylated at a proline residue, leading to its degradation by proteasomes. Only under hypoxia is HIF-1α stabilized and translocated to the nucleus to dimerize with its partner ARNT (HIF-1β). Together, the dimer acts as a transcription factor and upregulates the glycolytic pathway at multiple points [28]. The HIF1 pathway also rewires cellular metabolism by directing metabolites away from the TCA cycle [29, 30], and is the central regulator of the Warburg effect [31].

Our ATPome study revealed an unexpected and robust function of the HIF1 pathway in inhibiting respiratory function under normoxia, further highlighting the central role of the HIF1 pathway in cellular energy metabolism. To understand HIF1’s mechanisms in regulating energy, we designed two complementary CRISPRi screenings under HIF1 activation or inhibition. To inhibit the HIF1 pathway, we adopted a dual sgRNA-expressing library, enabling the identification of genes that regulate ATP levels in a HIF1-dependent manner. By incorporating doxycycline-inducible proteins, we were able to activate the HIF1 pathway and determine the upstream or downstream position of the HIF1-dependent genes. Through these screenings, we gained a more in-depth understanding of HIF1’s role in balancing glycolysis and respiration.

2.3 Results

Knockdown of HIF-1α or ARNT robustly rewires metabolism under normoxia

Our previous study indicated that both HIF-1α and ARNT potently repress respiratory ATP production. To validate if inhibition of the HIF1 pathway rewires substrate flux, we

conducted metabolomics analyses using *HIF1A* or *ARNT*-knockdown (KD) K562 leukemia cells by CRISPRi. The cells were restricted to use either glycolysis (glycolytic condition, with [U-^{13}C]glucose and 2-DG), respiration (respiratory condition, with [U-^{13}C]pyruvate and oligomycin) or both (unrestricted, with [U-13C]glucose and non-labeled pyruvate) for energy production. A control line expressing a non-targeting sgRNA (NTG) was also included.

Under the unrestricted condition, the knockdown of *HIF1A* or *ARNT* robustly increased the relative levels of most metabolites in glycolysis, the pentose phosphate pathway (PPP) and the TCA cycle (Fig. 2.1, A). Interestingly, despite the similarity in relative metabolite amounts between the two groups, different labeling percentages from [U-^{13}C]glucose suggested distinct rewiring in each group (Fig. 2.1, B). While the *ARNT* KD group showed increased labeling in TCA cycle metabolites, *HIF1A* KD led to notable decreased labeling, which may suggest a disconnection between glycolysis and the TCA cycle. This disconnection might have led to elevated non-labeled pyruvate uptake for compensation in the *HIF1A* KD group.

Under the glycolytic condition, a similarly pattern of relative metabolite levels was observed in the *HIF1A* KD group. However, these increases became less robust in the *ARNT* KD group, particularly in the peripheral metabolites. Surprisingly, in the absence of pyruvate supply, the *HIF1A* KD group showed increased labeling in succinate, fumarate and malate, while citrate, aconitate and isocitrate displayed decreased labeling. This pattern suggests that [U-^{13}C]glucose entered the TCA cycle through an alternative pathway bypassing pyruvate import. In contrast, the *ARNT* KD group exhibited decreases in labeling across nearly all TCA metabolites.

The *HIF1A* KD and *ARNT* KD groups showed the most drastic differences under the respiratory condition. The *HIF1A* KD group exhibited mostly elevations in the TCA cycle metabolites, while these were reduced in the *ARNT* KD group. Remarkably, the *HIF1A* KD group had prominently lowered labeling of lactate (SFig. 2.1, A), aligning with its canonical function under hypoxia, but for the first time shown to influence the substrate flux under normoxia as well. Interestingly, the substrate divergence did not seem to facilitate increased influx into the TCA cycle, as labeling of TCA metabolites declined. Instead, an increase in influx toward PPP was observed (SFig. 2.1, B). Consistent with the rewiring under the glycolytic condition, an alternative route bypassing pyruvate import also appeared to occur under the respiratory condition.

Through this extensive metabolomics analysis, we have demonstrated the HIF1 pathway's central role in metabolism, particularly in determining substrate flux. This newly identified normoxic function of HIF1 has not been reported until now and requires further investigation.

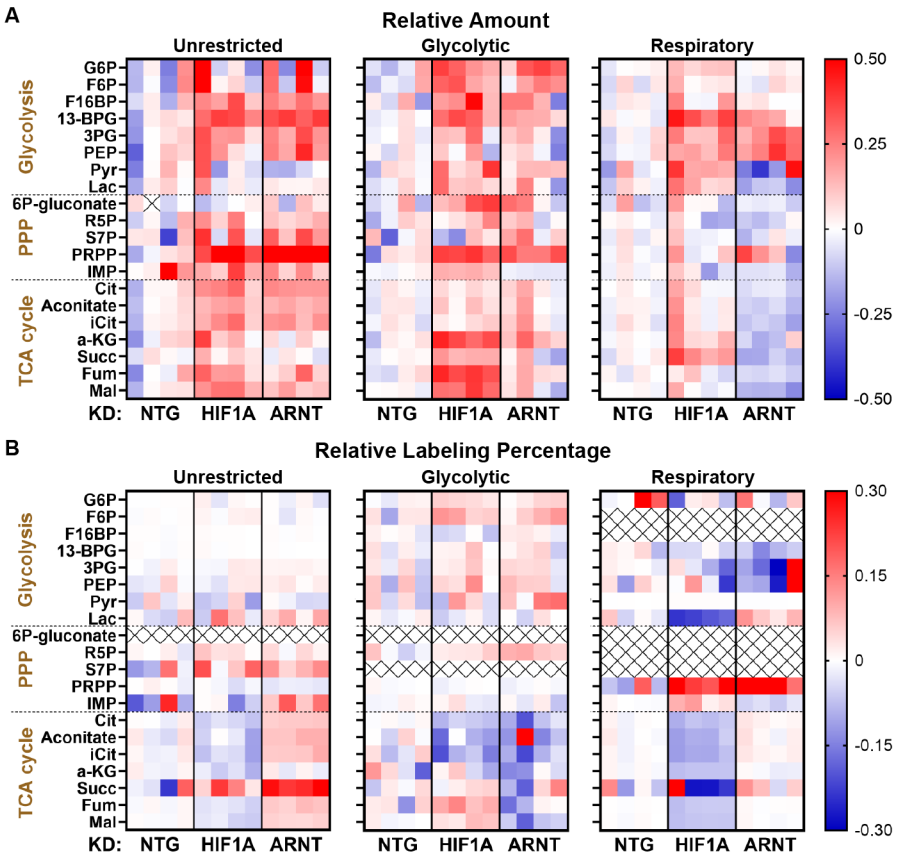

Figure 2.1: Significant metabolic reprogramming following knockdown of *HIF1A* or *ARNT* under normoxia. K562 cells with knockdown of *HIF1A* or *ARNT* were incubated in different metabolic conditions for 6 hours under normoxia before harvest. Cell metabolite extract was analyzed by an ion chromatography-mass spectrometry (IC-MS) detector. Heat map shows relative total levels of metabolomics determined by non-targeted metabolomic **(A)** and relative labeling percentage from ^{13}C-labeled substrate of each metabolite by targeted metabolomics **(B)**. Each square shows the log value of a metabolite level or labeling percentage in a repetition normalized to the mean of the non-targeting (NTG) group in respective condition. Metabolic conditions: unrestricted, [U-^{13}C]glucose and non-labeled pyruvate without inhibitors; glycolytic, [U-13C]glucose and oligomycin; respiratory, [U-^{13}C]pyruvate and 2-DG. G6P, glucose 6-phosphate; F6P, fructose 6-phosphate; F16BP, fructose 1,6-bisphosphate; 13BPG, 1,3-bisphosphoglycerate; 3PG, 3-phosphoglycerate; PEP, phosphoenolpyruvate; Pyr, pyruvate; Lac, lactate; R5P, ribose 5-phosphate; S7P, sedoheptulose 7-phosphate; PRPP, phosphoribosyl pyrophosphate; IMP, inosine monophosphate; Cit, citrate; a-KG, α-ketoglutarate; Succ, succinate; Fum, fumarate; Mal, malate. N = 4 repetitions/group/condition.

Dual sgRNA-expressing system exhibits sufficient knockdown to induce physiological impacts

To identify the energy-regulating genes acting through a HIF1-dependent manner, we developed a double-knockdown system, where two sgRNA-expressing cassettes are combined on a single construct (Fig. 2.2, A). One cassette expressed a mini-library of around 400 genes previously found critical to energy balance using an mU6 promoter,

while the other expressed an individual sgRNA targeting *HIF1A*, *ARNT* or NTG control using a hU6 promoter. This design ensured that each cell received both guides at a 1:1 ratio.

K562 leukemia cells with the dCas9-KRAB machinery and an ATP-FRET sensor were transduced with this double library. To validate the inhibition of the target genes, we performed qPCR analyses to measure the mRNA expression of *HIF1A* or *ARNT* in the corresponding groups. The knockdown efficiency in each group was around 50 – 55% (Fig. 2.2, B). Traditionally, we achieved over 90% inhibition of the target gene with a single sgRNA library. Therefore, we further measured the expression of downstream HIF1 pathway genes after a 3-day hypoxic incubation, including *HK2*, *LDHA*, and *PDK1*. All three genes were significantly downregulated in the *HIF1A* KD group, and *HK2* and *PDK1* showed a downward trend in the *ARNT* KD group (Fig. 2.2, C). This confirmed that the knockdown from the double library was sufficient to induce physiological impacts.

The respiratory ATP-boosting effect requires an intact respiratory chain

Transduced K562 cells were incubated in the three different metabolic media for 30 minutes prior to FACS sorting by ATP level, forcing the cells to use different substrates for energy production. We first examined the respiratory ATP phenotype of the top hits from our previous ATPome study to confirm reproducibility. *HK2*, *VDAC1*, *HIF1A* and *ARNT* were the top respiratory ATP booster, and *NDUFA8*, *COX16* and *TMEM261* were at the lowest end. Indeed, most of these high versus low ATP hits showed a good separation (SFig. 2.2, A). However, some did not exhibit as robust phenotype as in the prior study, likely due to suboptimal knockdown efficiency from the double construct.

We focused on the respiratory condition as it consistently showed a more prominent phenotype than the others and was where the HIF1 pathway's normoxic function was reported. In both *HIF1A* and *ARNT* KD groups, the ATP phenotype of *HIF1A* and *ARNT* sgRNAs in the mini-library was drastically decreased to nearly neutral levels (SFig. 2.2, B and C). This was expected and further confirmed sufficient knockdown from the individual *HIF1A* and *ARNT* guides. We then examined the differences in ATP phenotype between the HIF1 knockdown groups and the NTG control at a pathway level (Fig. 2.2, D and E). In the NTG group, all but one glycolytic gene knockdown led to a positive ATP phenotype as previously reported, while inhibition of the HIF1 pathway robustly neutralized their phenotype. This matched our expectation, as many of the glycolytic genes are regulated by the HIF1 pathway. In contrast, while around two-thirds of mitochondrial gene knockdowns (complex I, complex IV and mitochondrial ribosomal proteins) showed a negative phenotype, inhibition of the HIF1 pathway further lowered, rather than boosted, the ATP level in cells, particularly in the HIF1A KD group. This finding indicates that the HIF1's normoxic function requires an intact respiratory chain and is perhaps a result of metabolic rewiring.

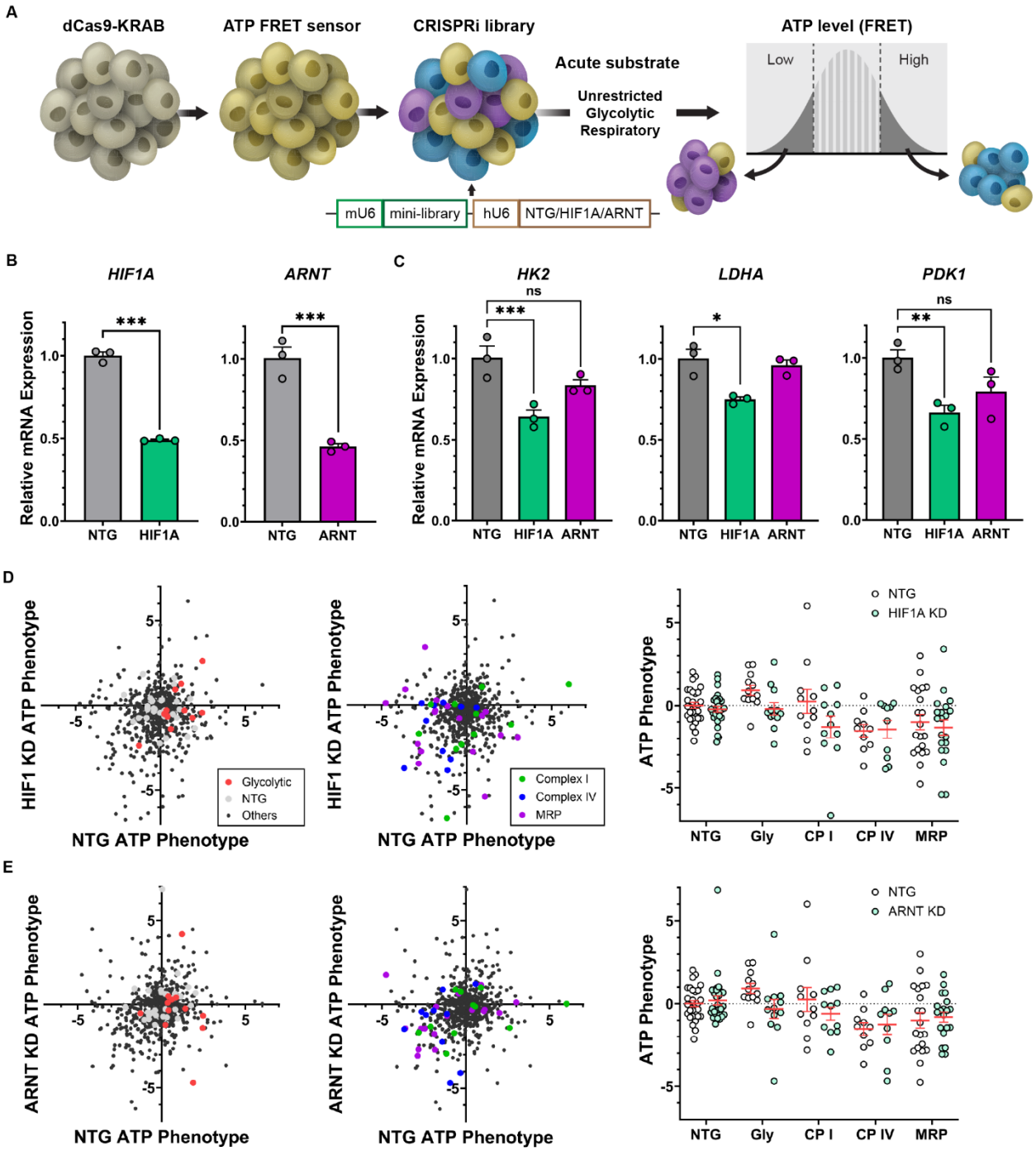

Figure 2.2: CRISPRi screening under HIF1 pathway inhibition reveals drastic decreases in ATP level of mitochondrial gene knockdown. (A) Schema shows single-cell detection and sorting based on ATP. K562 cells incorporated with dCas9-KRAB and an ATP FRET sensor were transduced with a dual guide-expressing mini library. In the double construct, the first cassette expresses the mini library, and the second expresses an individual guide of *HIF1A*, *ARNT* or non-targeting control. Cells were then incubated in different metabolic media for 30 minutes prior to sorting. The lowest and highest ATP quartiles were isolated by flow cytometry, and the relative enrichment of each sgRNA was quantified by deep sequencing. **(B)** Knockdown efficiency of the target gene in each group was evaluated by qPCR. **(C)** Downstream gene expression level under

HIF1 pathway inhibition was quantified by qPCR. Cells were incubated in 1% oxygen for 3 days before harvest. In (B) and (C), N = 3 repetitions/group. Data represent mean ± SEM. *$P < 0.05$, **$P < 0.01$, ***$P < 0.001$ by t-test with Welch's correction (B) or Welch's ANOVA test with Dunnett's T3 *post hoc* test. **(D)** and **(E)** Comparison plots of ATP phenotypes of a gene knockdown under HIF1A (D) or ARNT (E) inhibition (Y-axis) versus in the NTG control (X-axis) under the respiratory condition. N = 5 repetitions/group/condition from 2 independent experiments. Each dot represents an sgRNA in the mini library. Data represents the mean ATP phenotype in the comparison graphs (left and middle panel), and mean ± SEM in the column graphs (right panel). Gly, glycolytic; CP I, complex I; CP IV, complex IV; MRP, mitochondrial ribosomal protein.

Subtle effects of HIF1 inhibition under glycolytic and unrestricted conditions

Inhibition of glycolytic genes under *HIF1A* KD when cells were restricted to glycolysis led to a mild downshift in the ATP phenotype (SFig. 2.3, A), likely due to HIF1's systemic control over the pathway. However, this phenomenon was not observed in the *ARNT* KD group (SFig. 2.3, B). A mild decrease in ATP level with mitochondrial gene knockdown was seen in both groups, but overall, the pattern was not clear. Similarly, under the unrestricted condition, the effect of HIF1 pathway inhibition was subtle, with perturbation of most genes showing a nearly neutral phenotype, perhaps due to compensation from the other energetic pathway (SFig. 2.3, C and D).

Activation of the HIF1 pathway strongly inhibits respiratory ATP production

Given the broad impact of the HIF1 pathway on various physiological adaptations and its regulation of numerous gene, we employed an inducible HIF1 system to distinguish the genes upstream or downstream of the pathway. We generated a doxycycline-inducible, constitutively active HIF-1α protein by deleting its oxygen-sensing proline, as well as a doxycycline-inducible wildtype ARNT protein (Fig. 2.3, A). These proteins showed specific induction after 48 hours of doxycycline treatment (Fig. 2.3, B). HIF1 target gene expressions were also elevated (SFig. 2.4, A).

Following the same paradigm, we observed a significant downshift in ATP levels during FACS sorting, specifically in the inducible HIF-1α group under the respiratory condition (Fig. 2.3, C). This downshift was not observed in the ARNT group or the control group without inducible proteins (plain group).

Respiratory deficits do not decrease mitochondrial ATP beyond the effect of HIF1 activation alone

To exclude the effects of doxycycline treatment itself, we first compared the respiratory ATP phenotypes in the plain group with or without doxycycline. Most elements in the mini-library showed comparable ATP levels between the two conditions, indicating the impact of doxycycline treatment is negligible (SFig. 2.4, B).

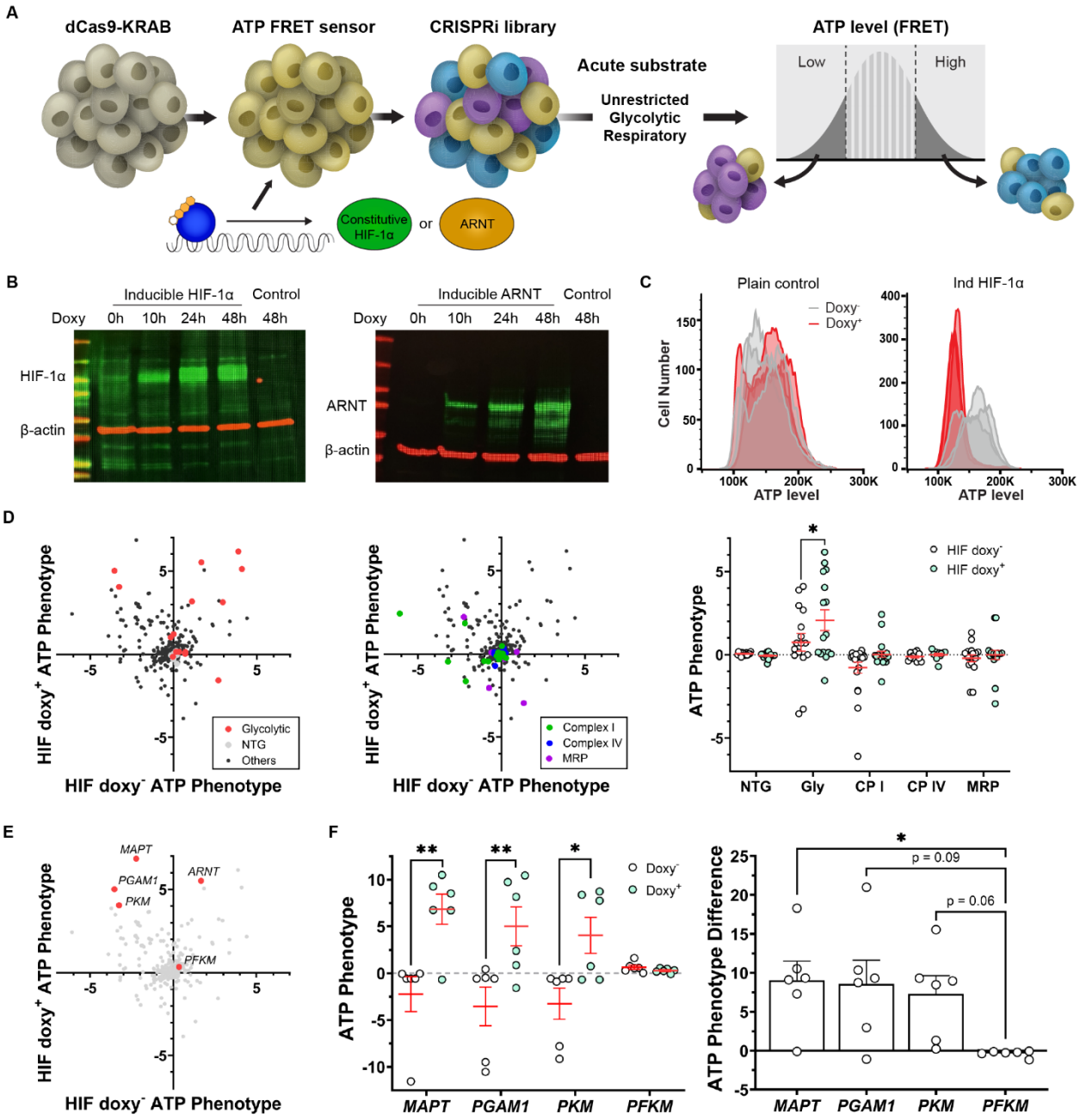

Figure 2.3: CRISPRi screening under HIF1 pathway activation identifies genes required for HIF1's normoxic repression on respiration. (A) Paradigm of CRISPRi screening incorporated with doxycycline-inducible constitutive HIF-1α or ARNT. Constitutive HIF-1α was generated by removing the oxygen-sensing region of the protein. HIF1-induced groups were treated with 300 ng/μL of doxycycline for 48 hours before incubation in metabolic media. **(B)** Doxycycline inducibility was validated using western blotting probing for HIF-1α or ARNT after treatment for varying duration. **(C)** Representative histograms of ATP FRET signal after doxycycline treatment in the inducible HIF1 and the control groups under the respiratory condition. N = 3 repetitions per group. **(D)** Comparison plots of ATP phenotypes of a gene knockdown with (Y-axis) or without (X-axis) doxy-induction in the inducible HIF-1α group under the respiratory condition. N = 6 repetitions/group/condition from 3 independent experiments. Each dot represents an sgRNA in

the mini library. Data represents the mean ATP phenotype in the comparison graphs (left and middle panel), and mean ± SEM in the column graphs (right panel). *$P < 0.05$ by two-way ANOVA with Sidak's *post hoc* test. **(E)** Comparison plot highlighting genes of which knockdown showing consistent and significant differences in ATP phenotype with or without doxy-induction in the HIF-1α group under the respiratory condition. **(F)** Column graphs showing the ATP phenotypes (left) or differences in ATP phenotype (right) of *MATP*, *PGAM1*, *PKM* and *PFKM* in each repetition. N = 6 repetitions from 3 independent experiments. Data represents mean ± SEM. Each dot represents one repetition. *$P < 0.05$, **$P < 0.01$ by two-way ANOVA with Sidak's *post hoc* test or Welch's ANOVA test with Dunnett's T3 *post hoc* test.

Under the respiratory condition, the majority of glycolytic genes sat within the first quadrant in the comparison graph (Fig. 2.3, D), exhibiting significantly higher ATP phenotype at a pathway level. This is expected as the glycolytic pathway is a known downstream target of the HIF1 pathway. However, it is important to note that the higher ATP level was relative to their own internal non-targeting controls. This does not necessarily mean that inhibiting glycolytic genes under HIF1 activation can further boost respiratory energy production. On the other hand, repression of mitochondrial genes appeared to have a neutral phenotype under HIF1 activation, indicating respiratory ATP production was massively diminished in this context. This can be explained by the HIF1 pathway directing pyruvate to lactate, resulting in little substrate reaching to the TCA cycle, thus rendering the presence of a functional respiratory chain irrelevant.

Interestingly, in the FACS data, HIF1 activation left a long tail at the higher ATP end (Fig. 2.3, B), indicating elements resistant to HIF1's substrate diverting function. We specifically looked for genes that consistently showed relatively high ATP levels across 6 independent sorting under HIF1 activation (Fig. 2.3, E). These genes include two distal glycolytic genes, *PGAM1* and *PKM*, and a well-known neuronal protein, tau (*MAPT*). In contrast, knockdown of a proximal glycolytic gene, *PFKM*, did not to show such an energy-retaining effect.

Lack of phenotypes under the glycolytic and unrestricted conditions

In contrast to the HIF1 group, the doxycycline-inducible ARNT group failed to show a clear impact on ATP levels under the respiratory condition (SFig. 2.4, C), with most elements aligning along a line with a slope of 1. This could result from leakage in the inducible system. However, due to the constitutive endogenous ARNT expression, it was difficult to assess the degree of leakage accurately.

Activation of the HIF1 pathway did not seem to exert a profound impact on glycolytic or mitochondrial genes under either the glycolytic or unrestricted condition (SFig. 2.4, D and E). Traditionally, it has been challenging for us to obtain consistent results from these two metabolic conditions, possibly due to numerous compensatory mechanisms and glycolytic enzyme isoforms that help maintain energy levels at a constant state.

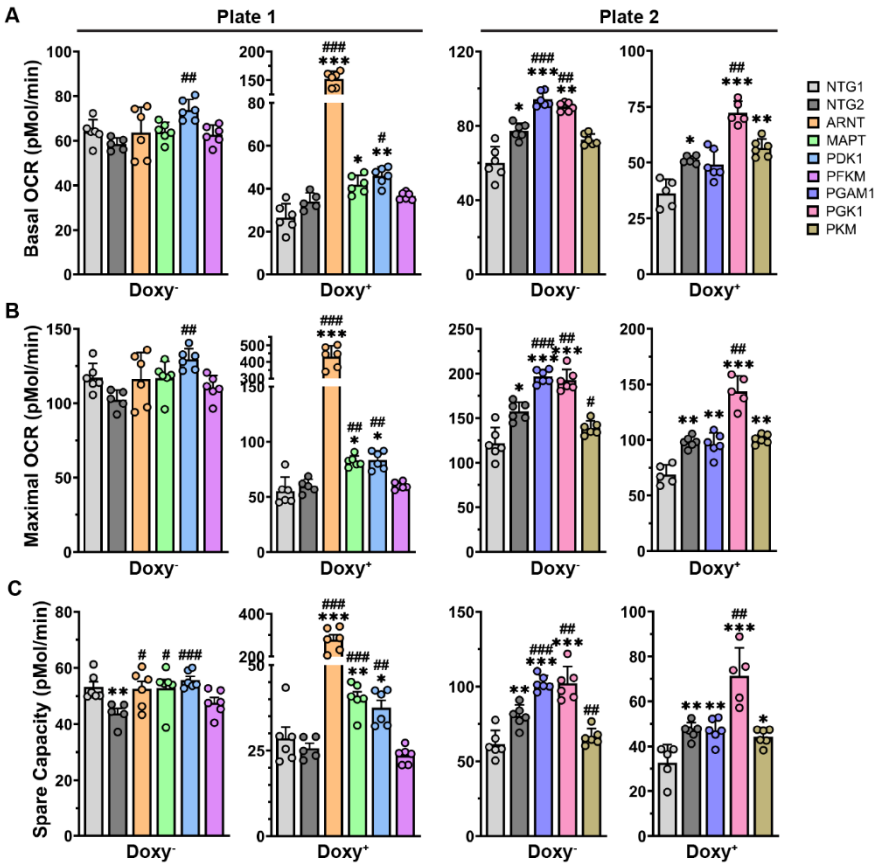

Figure 2.4: Knockdown of *ANRT*, *MAPT*, *PDK1* and certain glycolytic genes rescue respiratory capacity under HIF1 activation. (A) and **(B)** Basal and maximal respiratory capacity (pmol O_2/min) of K562 cells with selected gene knockdown were measured using a Seahorse Analyzer following the addition of the mitochondrial uncoupler FCCP (600 nM). **(C)** Spare capacity was calculated by subtracting the basal capacity from the maximal capacity. Each dot represents one repetition. Data represents mean ± SEM. **P* < 0.05, ***P* < 0.01, ****P* < 0.001 by Welch's ANOVA test with Dunnett's T3 *post hoc* test. Comparisons are made with the NTG1 group (*) and with the NTG2 group (#) in each plate.

Knockdown of MAPT and selected distal glycolytic genes rescues respiratory capacity under HIF1 activation

The observed relatively high ATP levels could be result from increased respiratory ATP production or decreased energy expenditure. Given HIF1's canonical function of directing pyruvate to lactate, we hypothesized that MAPT, PGAM1 and PKM might be important for inhibiting respiration under HIF1 activation. To validate this, we conducted a Seahorse assay to measure respiratory capacity. In addition to these hits, we included 3 other genes that play important roles in the HIF1 pathway or glycolytic regulation: ARNT, PDK1, and PGK1. PFKM was again included as a control.

Given the common variability in Seahorse assays, we put in two non-targeting guides on each plate. In each run, HIF1 activation significantly inhibited both basal and maximal oxygen consumption rates (OCRs) in the NTG groups (Fig. 2.4, A, B).

Notably, knockdown of *ARNT*, *MAPT*, *PDK1*, and *PGK1* significantly rescued both basal and maximal OCRs compared with both NTGs under HIF1 activation. Knockdown of *PKM* showed higher basal and maximal OCRs than NTG1, and *PGAM1* knockdown showed higher maximal OCRs than only NTG1. Interestingly, *PDK1*, *PGAM1* and *PGK1* knockdown exhibited higher respiratory capacity without HIF1 induction, suggesting HIF1-independent control over respiration.

In terms of spare capacity, knockdown of *ARNT*, *MAPT*, *PDK1*, *PGAM1*, *PGK1* and *PKM* all showed significant differences compared to at least one NTG group (Fig. 2.4, C), while *PFKM* knockdown did not lead to any changes. These data clearly show that HIF1's inhibition of respiratory capacity is mediated by *MAPT* and certain distal glycolytic enzymes.

Tau and glycolytic enzymes are required for HIF1-induced metabolic rewiring

To determine how decreased expression of tau and other distal glycolytic enzymes affects HIF1's metabolic rewiring, we again utilized metabolomics to observe substrate flux under different conditions. When cells were supplemented with [U-^{13}C]glucose and restricted to glycolysis, knockdown of distal glycolytic genes under normal condition led to a drastic buildup of glycolytic metabolites, precisely associated with the location of the blockage (Fig. 2.5, A). Similarly, *ARNT*, *MAPT* and *PDK1* knockdown also resulted in accumulation of these metabolites, but to a lesser extent. *PFKM* exhibited a different pattern from others, showing decreases in PPP metabolites. Nonetheless, perturbation of these genes did not significantly changed labeling across glycolysis (Fig. 2.5, B).

For TCA cycle metabolites, knockdown of distal glycolytic genes and *PDK1* led to mild increases in relative levels and robust increases in labeling under normal condition, while *ARNT* and *MAPT* knockdown did not show a clear impact in this context. As expected, labeling of TCA metabolites decreased when HIF1 was activated (NTG doxy+ versus NTG doxy-), with relative levels increasing, perhaps due to a blockage. Remarkably, *ARNT*, *MAPT* and *PKM* knockdown showed the most drastic increases in TCA labeling under HIF1 activation. *PGK1* and *PGAM1* exhibited a similar shift to a lesser degree. This indicates these genes are required to prevent glucose from entering the TCA cycle. In contrast, *PDK1* and *PFKM* inhibition did not seem to reverse HIF1's metabolic rewiring.

When cells were supplemented with [U-^{13}C]pyruvate and restricted to respiration, HIF1 activation caused decreased levels and labeling of metabolites across glycolysis, PPP and the TCA cycle. This could be due to the rapid removal of lactate from the cells after production (Fig. 2.5, C and D). Interestingly, opposite to the refusion of glucose into the TCA cycle, knockdown of *ARNT*, *MAPT*, *PDK1*, *PGK1* and *PKM* further decreased TCA labeling from pyruvate under HIF1 activation. This indicates an alternative route bypassing the direct entry of pyruvate, likely through α-ketoglutarate, as its level dramatically elevated. Notably, *PGAM1* showed a distinct

pattern from others in both relative amount and labeling, suggesting a unique role in HIF1 pathway function.

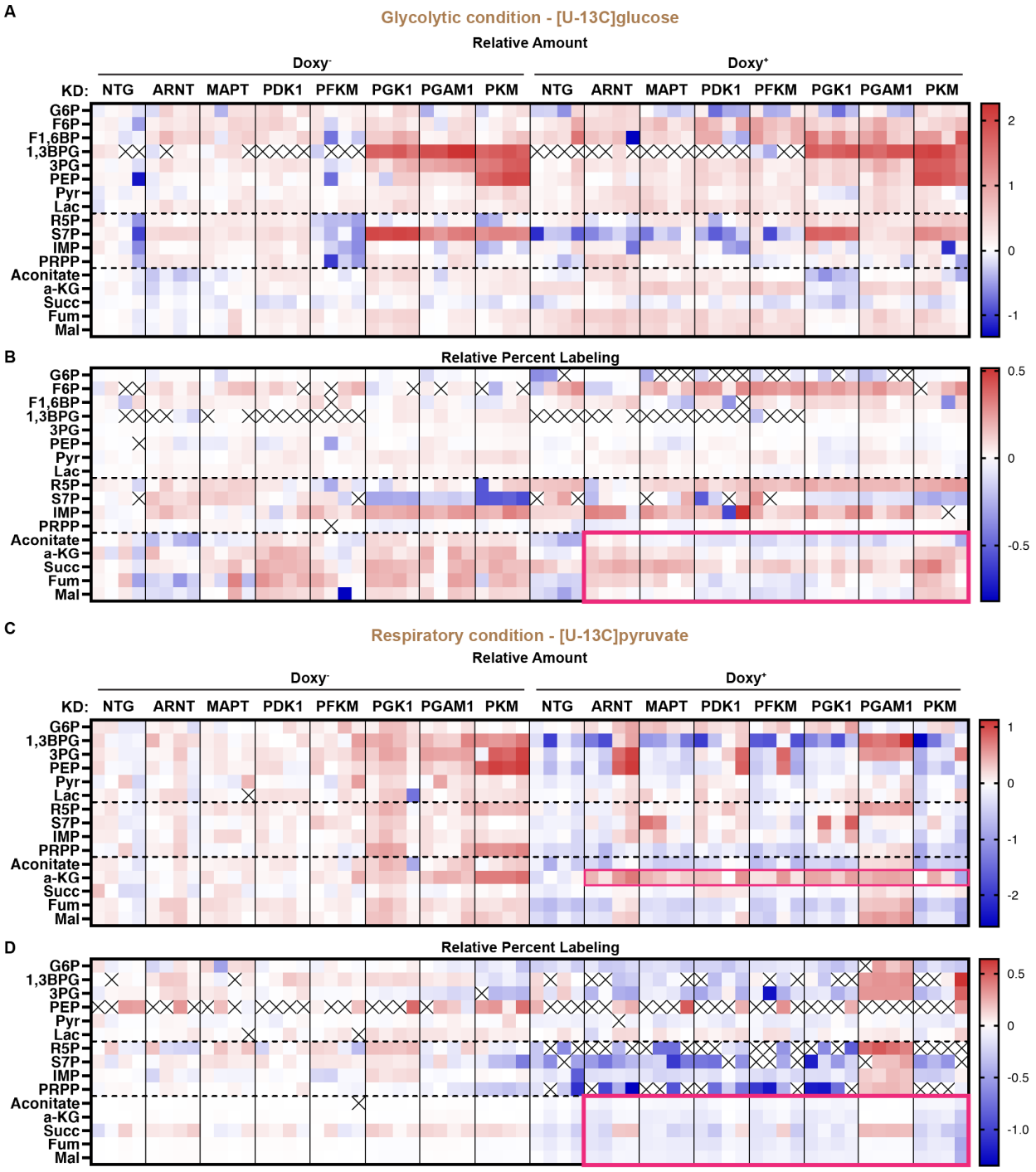

Figure 2.5: HIF1-induced metabolic reprogramming is mediated by tau and glycolytic enzymes. K562 cells with knockdown of selected hits were induced by doxycycline for 48 hours and incubated in different metabolic conditions for 6 hours under normoxia before harvest. Cell metabolite extract was analyzed by an ion chromatography-mass spectrometry (IC-MS) detector. **(A)** Heat map shows relative total levels (upper panel) and relative percent labeling (lower panel)

of metabolites under the glycolytic condition. **(B)** under the respiratory condition. Each square shows the log value of a metabolite level or labeling percentage in a repetition normalized to the mean of the non-targeting (NTG) group without doxy induction in respective condition. Metabolic conditions: glycolytic, [U-^{13}C]glucose and oligomycin; respiratory, [U-^{13}C]pyruvate and 2-DG.

2.4 Discussion

Ever since the discovery of the HIF1 pathway in 1991 [32], immerse efforts have been put into understanding its functions under hypoxia. The canonical hypoxic mechanism of HIF1 has been well-studied, primarily through the upregulation of two enzymes that direct substrate flow away from respiration: LDHA [33] and PDK1 [29]. LDHA facilitates the conversion of pyruvate to lactate, while PDK1 inhibits PDH, which facilitates the entry of pyruvate into the TCA cycle. Thus, the central role of the HIF1 pathway in coordinating glycolysis and respiration has been well-established, especially in cancer biology, due to the unique hypoxic microenvironment in tumors. Therapeutic interventions targeting the HIF1 pathway in cancer management have been extensively explored [34]. Additionally, studies have identified the significance of this pathway in the progression of other diseases, including cardiovascular diseases [35], metabolic diseases [36], neurological diseases [37] and aging [38]. However, the normoxic functions of the HIF1 pathway remain underexplored.

In our previous study, we reported an unexpected function of HIF1 in inhibiting mitochondrial respiration under normoxia [27]. Here, we dissect the normoxic mechanisms of HIF1's metabolic regulation. Using two complementary CRISPRi screenings, we discovered that despite HIF1's trace level and activity at normal oxygen level, it remains vital in controlling substrate fluxes and coordinating the intersection of glycolysis and respiration. Inhibition of HIF1 leads to an increased flux of pyruvate down to the TCA cycle. When the respiratory chain is intact, this increases respiratory capacity and results in a higher ATP phenotype. However, when the respiratory chain is dysfunctional due to the knockdown of mitochondrial genes, the elevated influx causes a buildup of substrates without producing energy, resulting in further decreased ATP phenotypes than in the control group. In contrast, activation of HIF1 forces the conversion of pyruvate to lactate. Since the substrate cannot be used for respiratory energy production, it no longer matters if the respiratory chain is intact. As such, knockdown of mitochondrial genes does not affect ATP levels beyond the effect of HIF1 activation alone. These data support HIF1's normoxic control over the balance between glycolysis and respiration.

Intriguingly, constitutive HIF1 overexpression did not increase either the relative level or labeling percentage of lactate compared with the non-induced control group in metabolomics analysis. This suggests a rapid removal of lactate after production, probably via MCT4, a monocarboxylate transporter downstream of the HIF1 pathway [39]. Nonetheless, when HIF1A was knocked down under normoxia, we observed a prominent accumulation of lactate with a significant decrease in labeling, indicating a baseline level of MCT4 expression or activity mediated by HIF1.

Both HIF1A knockdown and overexpression led to decreases in TCA metabolite labeling when cells were supplemented with [U-^{13}C]pyruvate. While it is more understandable in the case of HIF-1α overexpression, as pyruvate is converted into lactate, the decrease observed in the HIF1 knockdown group is contradictory to the canonical functions of the pathway. The direct entry of pyruvate into the TCA cycle seems to be blocked. It could be either a difficulty of pyruvate transportation into mitochondria, facilitated by MPC1 and MPC2, or a blockage in the conversion of pyruvate to acetyl-CoA, facilitated by PDH. However, both complexes have been reported to be negatively regulated by the HIF1 pathway, either directly or indirectly [40]. It would be interesting to further investigate if the HIF1 pathway also maintains a baseline level of the MPCs and PDH, or if other mechanisms of pyruvate transportation or metabolism are involved.

Through a series of experiments from CRISPRi screening to Seahorse assay and metabolomics, we determined the consequential role of tau and glycolytic enzymes in HIF1's normoxic repression on respiration. Knockdown of these genes rescued the decreased ATP level caused by HIF1 activation, likely through mitigating HIF'1 metabolic reprogramming. Recently, growing evidence has highlighted the importance of glycolytic complexes in determining substrate flow. Zhu and colleagues identified a long non-coding RNA, glycoLINC, acting as a scaffold for the assembly of the lower glycolytic metabolon [41]. This metabolon was found to be critical for maintaining glycolytic flux and cellular ATP levels. Similarly, the HIF1 pathway was recently found to enhance glycolysis not only by upregulating the expression levels of glycolytic genes, but also by promoting the formation of glycolytic complexes [42]. Notably, proteomics revealed that tau physically interacts with multiple glycolytic enzymes, including GAPDH, PGK1, PGAM1, Enolase, PKM and LDHA [43]. It is likely that tau plays a role in the assembly of the glycolytic metabolon under HIF1 activation.

However, knockdown of tau, PDK1 and the glycolytic genes did not fully rescue the respiratory capacity under HIF1 activation. Despite the reinfusion of glucose into the TCA cycle, knockdown of these genes was unable to improve the direct entry of pyruvate into the TCA. Alternatively, pyruvate might be converted into alanine in the cytoplasm, and α-ketoglutarate, as a byproduct of the reaction, in turn fuels the TCA cycle. This could explain the robustly elevated level of α-ketoglutarate and overall unaltered labeling of TCA metabolites in our metabolomics data. There seems to be a direct impact of HIF1 on PDH expression or activity, as knockdown of the primarily regulator PDK1 failed to rescue the deficit. In addition, the HIF1 pathway is also known to directly affect respiratory efficiency by modulating respiratory chain composition and mitochondrial turnover [44]. The complicated metabolic regulation requires future efforts to delineate.

In summary, our findings provide vital insights into HIF1's normoxic functions, particularly its repression of mitochondrial respiration. We demonstrate that despite generally considered inactive under normoxia, the HIF1 pathway still plays an important role in determining substrate flux, and this process requires tau and certain glycolytic enzymes. Our results also highlight a potential role of tau in the formation of glycolytic metabolon.

However, knockdown of these genes did not fully rescue HIF1's inhibition of respiration, indicating that other mechanisms are involved and require future investigation. Nonetheless, this study establishes a link between tau, neurodegeneration, aging and energy balance, suggesting promising potential avenues for therapeutic intervention.

2.5 Materials

Cell Lines

These studies were conducted with K562 human female leukemia cells provided by Jonathan Weissman's lab, identical to those used in our previously published ATP screens [26, 27]. The cells had stable expression of dCas9-KRAB enabling CRISPRi and a FRET ATP sensor (Clover-mApple). For cell culture, K562 cells were maintained in RPMI-1640 media with 25 mM HEPES, 0.3 g/L L-glutamine, 2.0 g/L $NaHCO_3$, and supplemented with 10% tetracycline-free fetal bovine serum (Takara Bio, 631106), 100 units/mL penicillin, 100 mg/mL streptomycin, and 2 mM glutamine.
Cells expressing doxycycline-inducible HIF-1α and ARNT were generated by lentiviral transduction followed by blasticidin selection. Constitutive HIF-1α was made by the removal of oxygen-sensing domain.

Lentiviral Transduction

Lentivirus expressing the CRISPRi sgRNA mini-library was produced by commercial resources and transduced with polybrene (8 μg/ml) into K562-dCas-KRAB cells via spinfection. 48 hours after transduction, puromycin selection (1 μg/ml or 2 μg/ml for cells expressing inducible HIF-1α or ARNT) was maintained for 5 days.

Metabolomics

K562 cells were incubated for 6 hours under normoxia in either (1) respiratory condition: 2% FBS, 10mM [U-^{13}C]pyruvate + 10mM 2DG, (2) glycolytic condition: 2% FBS, 2mM [U-^{13}C]glucose + 5μM oligomycin + 3mM 2-deoxyglycose, or (3) unrestricted condition: 2% FBS, 10mM [U-^{13}C]glucose + 5mM pyruvate with no drugs, before metabolite extraction in 80% methanol. Samples were then sent to UCLA Metabolomics Core for metabolites detection and quantification.

Gene Knockdown Validation by qPCR

Gene expression quantifications were performed using qRT-PCR on a 7900HT Fast Real-Time PCR System (Applied Biosystem), using VIC-MGB human ACTB as an endogenous control (β-actin, ThermoFisher 4326315E) and FAM-MGB TaqMan Gene Expression Assays (ThermoFisher, assay IDs: Hs00153153_m1-HIF1A, Hs01121918_m1-ARNT, Hs00606086_m1-HK2, Hs01378790_g1-LDHA, Hs01561847_m1-PDK1, Hs00902194_m1-MAPT, Hs01075411_m1-PFKM, Hs01652468_g1-PGAM1, Hs00943178_g1-PGK1, Hs00761782_s1-PKM). RNA was extracted using the Qiagen RNeasy kit (Qiagen, 74106), and cDNA and qPCR reactions were prepared using the Cells-to-CT kit (Invitrogen, A25605), following their protocol with a standard reverse transcription cycle (37 °C for 6 min, followed by 95 °C for 5 min and holding at 4 °C), and standard qRT-PCR conditions (UDG incubation of 50 °C for 2 min, enzyme activation at

95 °C for 10 min, and PCR cycles of 95 °C for 15 s, 60 °C for 1 min, repeated for 40 cycles). All reactions were performed in a 384-well plate with an N of at least 3 repetitions. Fold changes in expression were calculated using the 2−ΔΔCT method.

Flow Cytometry

To acutely force reliance on respiration and/or glycolysis prior to flow cytometry, cells were resuspended in PBS-based metabolic media, including: (1) respiratory condition: 2% FBS, 10mM pyruvate + 10mM 2DG, (2) glycolytic condition: 2% FBS, 2mM glucose + 5 μM oligo + 3 mM 2-deoxyglycose, or (3) unrestricted condition: 2% FBS, 10mM glucose + 5mM pyruvate with no drugs. Screenings under HIF1 inhibition were conducted on a BD FACS Aria II, and the ones under HIF1 activation were conducted on a BD FACS Aria Fusion I. The donor fluorophore (Clover) was excited using a 488-nm laser and detected using a 525/50-nm filter. FRET was detected by excitation from the 488-nm laser and emission via a 610/20 or 615/30-nm filter. mTagBFP fluorescence from the CRISPRi library was excited by a 405-nm laser and detected by a 450/50-nm filter. Donor and FRET channels were detected on a linear scale, and mTagBFP fluorescence was detected on a logarithmic scale. Sorting was conducted using four-way purity into two tubes and an 85-μm nozzle. At least 500 cells/sgRNA in the mini-library were collected in each repetition.

DNA Preparation and Sequencing

Genomic DNA was extracted using the Macherey-Nagel NucleoSpin Tissue kit (Macherey-Nagel, 740952.250). The sgRNAs were amplified and adaptors attached in a single PCR step. No more than 3 μg of undigested genomic DNA was used per 100 μL PCR reaction, and sufficient reactions were performed to include all isolated genomic DNA. PCR was conducted using Q5 HotStart High Fidelity Polymerase (NEB, M0493) using primers including necessary adaptor and indexing sequences. PCR parameters were 98 °C for 30 s, followed by 26 cycles of 98 °C for 15 s, 62.5 °C for 15 s, 72 °C for 20 s, and ending with 72 °C for 6 min; samples were then ramped down to 4 °C and held. The resulting PCR product from multiple reactions were pooled, and unincorporated primers were removed using the GeneRead Size Selection Kit. Quality and purity of the PCR product was assessed by bioanalyzer (Agilent) and sequencing was performed on an Illumina HiSeq 2500.

Western Blot Analysis

The HIF1 pathway was induced by 300 ng/mL doxycycline treatment for 48 hours. Whole cell extract was performed with RIPA buffer (Thermo Scientific, 89900) supplemented with protease inhibitor cocktail (Thermo Scientific, 87786). For inducible HIF-1α and ARNT validation, nuclear and cytosolic fractions were separated by the NE-PER extraction kit (Thermo Scientific, 778833). Protein extract was loaded on to polyacrylamide gels (Bio-Rad, 4569033) and electrophoresis was carried out using standard SDS-PAGE procedures. Protein was then transferred from the gel on to a PVDF membrane (Invitrogen, IB24001) using the iBlot™ 2 rapid transfer system (Invitrogen, IB21001). The PVDF membrane was blocked for 1 h in a 1:1 mixture of 1X phosphate-

buffered saline (PBS) and Li-Cor's Odyssey PBS blocking buffer (P/N 927-40000). Membrane was incubated overnight with primary antibodies: rabbit anti-hif-1α (Novus Biologicals, NB100-134, 1:1000) and rabbit anti-arnt (Cell Signaling, 5537, 1:1000). After incubation in secondary antibodies, Alexa Fluor 647 anti-mouse (Invitrogen, A31571, 1:10000) and Alexa Fluor 488 anti-rabbit (Invitrogen, A11008, 1:10000), membrane was imaged by Bio-Rad's ChemiDoc Imaging System.

Seahorse Assay

Oxygen consumption rate (OCR; to assess mitochondrial respiration) were measured in inducible HIF-1α K562 lines using a 96-well Seahorse XF96 Extracellular Flux Analyzer (Seahorse Bioscience). A Seahorse assay cartridge was calibrated with calibration medium overnight in a CO_2-free incubator. 200,000 cells/well were seeded and attached to XF96 microplates with Cell-Tak coating (Corning, 354240). Prior to measurement, cells were incubated for 1 hour in Seahorse XF RPMI assay media supplemented with 10mM pyruvate and 10mM 2-DG in a CO_2-free incubator. OCR was measured at baseline and again after sequential addition of the respiratory inhibitors FCCP (1 μM, carbonyl cyanide-4-(trifluoromethoxy) phenylhydrazone, a protonophore that uncouples oxidative phosphorylation and then rotenone (1 μM, an inhibitor of complex I)). After each run, cells were fixed with 4% paraformaldehyde, and the OCR signal was normalized to the number of cells in each well, estimated using DAPI staining. Spare capacity was calculated by subtracting basal OCR from maximal OCR.

2.6 Supplementary Figures

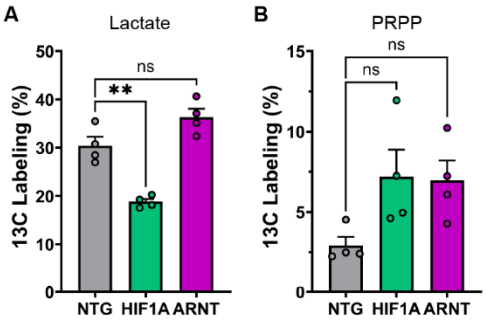

SFigure 2.1: *HIF1A* KD diverts [U-^{13}C]pyruvate to PPP from lactate under the respiratory condition. (A) Labeling percentage of lactate was significantly decreased in the *HIF1A* knockdown group under the respiratory condition. **(B)** Significant increase in PRPP (phosphoribosyl pyrophosphate) labeling percentage in both the *HIF1A* and *ARNT* knockdown groups under respiratory condition. N = 4 repetitions/group. Data represents mean ± SEM. ***P* < 0.01 by Welch's ANOVA test with Dunnett's T3 *post hoc* test.

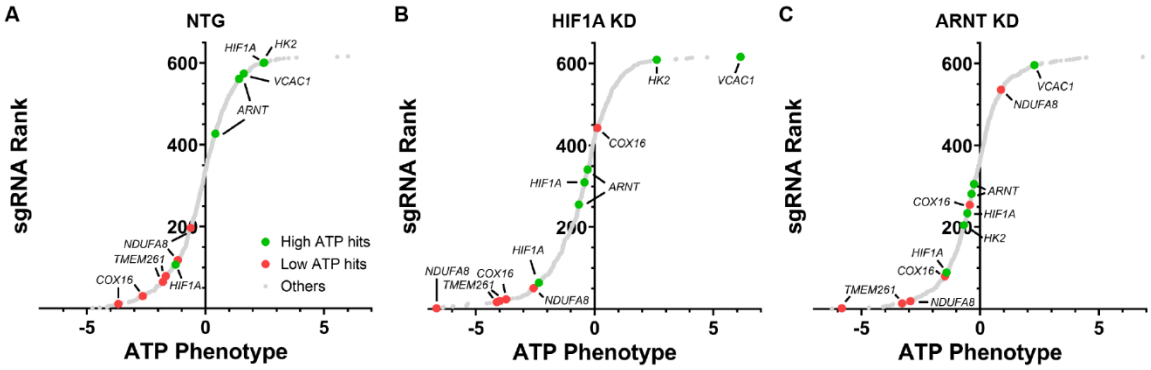

SFigure 2.2: The dual sgRNA library reproduces ATP phenotypes of previously identified hits. (A) S-curve ranking plot of the NTG group showing ATP phenotypes of selected hits identified from our previous study were reproduced under the respiratory condition. **(B)** and **(C)** ATP phenotypes of these hits were altered under *HIF1A* (B) or *ARNT* (C) knockdown, validating impactful knockdowns from the double library. Each dot represents the mean ATP phenotype of an sgRNA in the mini library of 5 repetitions from 2 independent experiments.

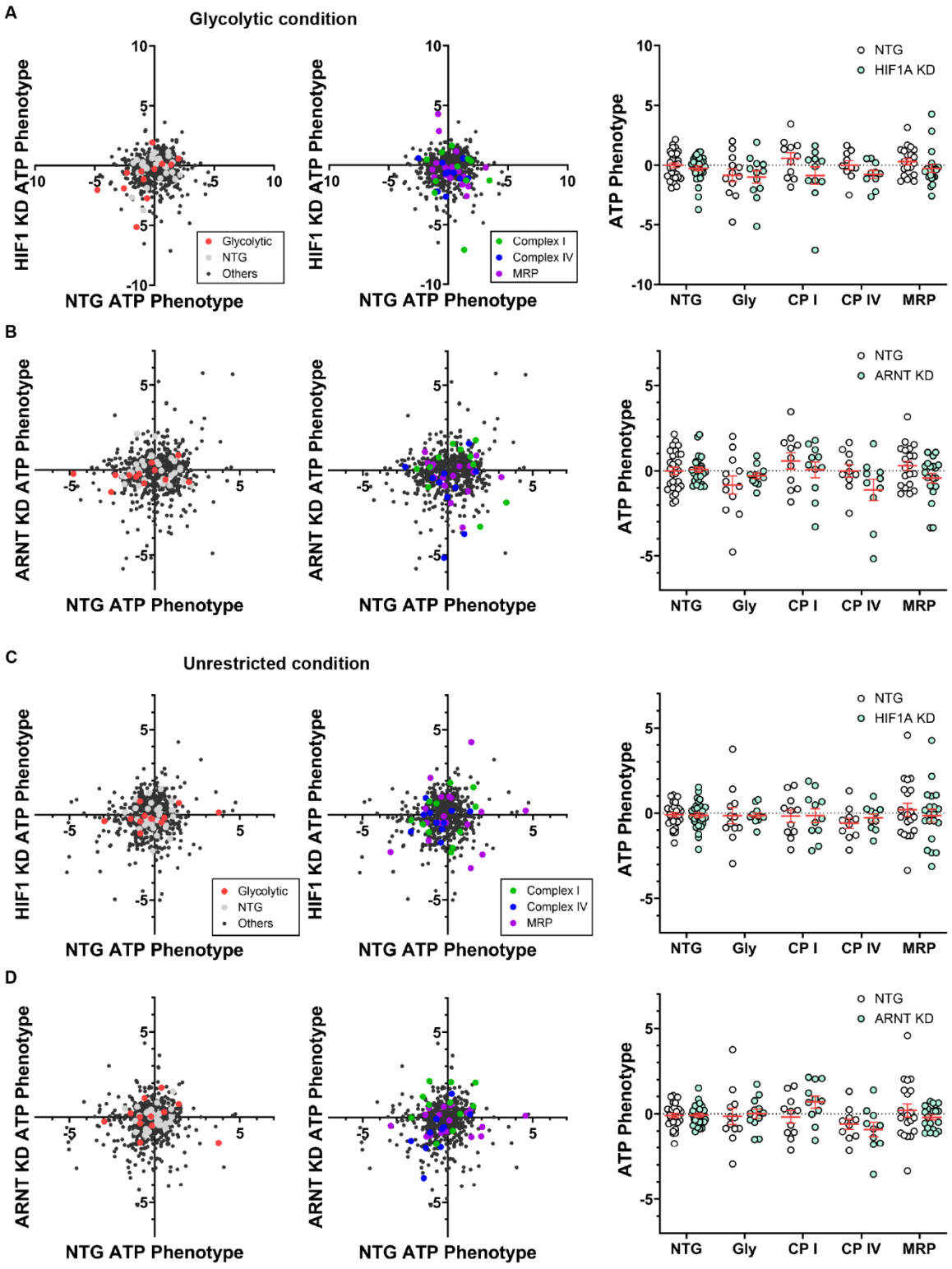

SFigure 2.3: Inconclusive impacts on ATP phenotypes of *HIF1A* or *ARNT* knockdown under the glycolytic or unrestricted conditions. (A) and **(B)** Comparison plots of ATP phenotypes of a gene knockdown under *HIF1A* (A) or *ARNT* (B) inhibition (Y-axis) versus in the NTG control (X-

axis) under the glycolytic condition. **(C)** and **(D)** Comparison plots of ATP phenotypes of a gene knockdown under *HIF1A* (C) or *ARNT* (D) inhibition (Y-axis) versus in the NTG control (X-axis) under unrestricted condition. N = 5 repetitions/group/condition from 2 independent experiments. Each dot represents an sgRNA in the mini library. Data represents the mean ATP phenotype in the comparison graphs (left and middle panel), and mean ± SEM in the column graphs (right panel).

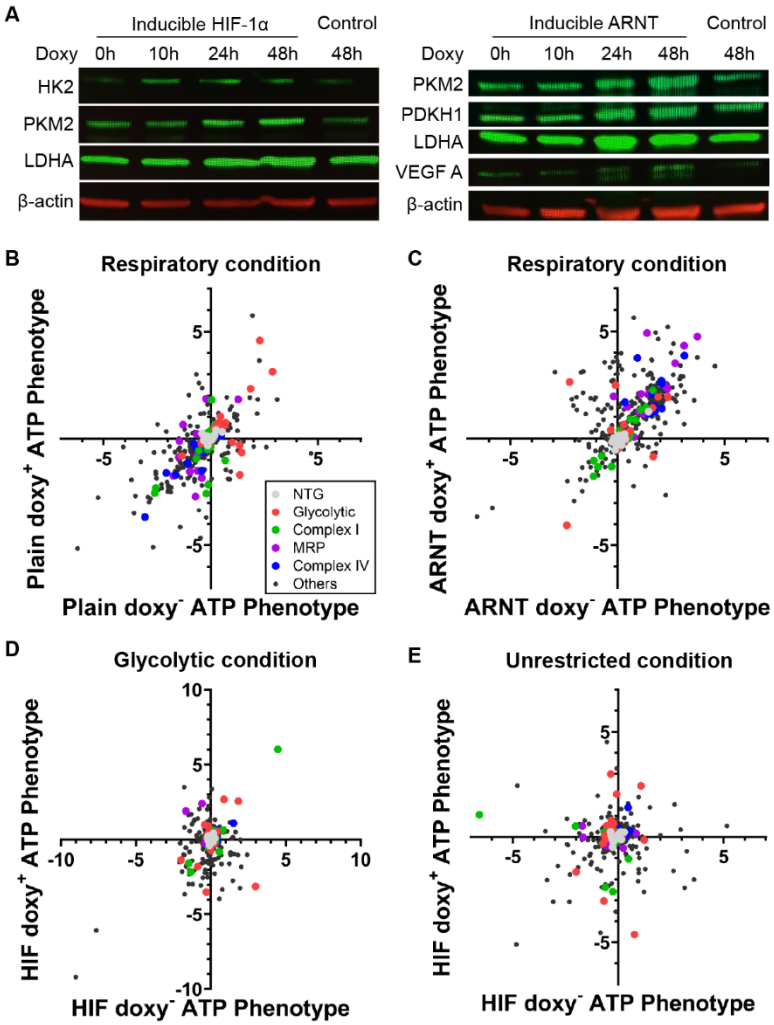

SFigure 2.4: ATP phenotype alterations in the inducible HIF-1α group are not attribute to chronic doxycycline treatment. (A) Downstream protein expressions were time-dependently elevated after doxy-induction of constitutive HIF-1α (left panel) or ARNT (right panel) by western blotting. **(B)** ATP phenotypes with (Y-axis) or without (X-axis) doxycycline treatment strongly correlated in the plain control group, suggesting inconsequential effects from doxycycline treatment alone. **(C)** Linear correlation between doxy- and doxy+ ARNT groups. **(D)** and **(E)** Comparison plots of the inducible HIF-1α group under the glycolytic (D) or unrestricted (E) condition. In (B) to (E), N = 6 repetitions/group/condition from 3 independent experiments. Each dot represents the mean ATP phenotype of an sgRNA in the mini library.

Chapter 3: CHCHD2 Mutant Mice Display Mitochondrial Protein Accumulation and Disrupted Energy Metabolism

3.1 Abstract

Mutations in the mitochondrial cristae protein CHCHD2 lead to a late-onset autosomal dominant form of PD which closely resembles idiopathic PD, providing the opportunity to gain new insights into the mechanisms of mitochondrial dysfunction contributing to PD. To begin to address this, we used CRISPR genome-editing to generate CHCHD2 T61I point mutant mice. CHCHD2 T61I mice had normal viability, and had only subtle motor deficits with no signs of premature DA neuron degeneration. Nonetheless, CHCHD2 T61I mice exhibited robust molecular changes in the brain including increased CHCHD2 insolubility, accumulation of CHCHD2 protein preferentially in the substantia nigra (SN), and elevated levels of α-synuclein. Targeted metabolomics revealed an increase in glucose metabolism through glycolysis relative to the TCA cycle, and immunoEM revelated disrupted mitochondria in DA neurons. Moreover, spatial genomics revealed decreased expression of mitochondrial complex I and III respiratory chain proteins, while proteomics revealed increased respiratory chain and other mitochondrial protein-protein interactions. As such, the CHCHD2 T61I point-mutation mice exhibit robust mitochondrial disruption and a metabolic shift likely secondary to respiratory failure. These findings thus establish CHCHD2 T61I mice as a new model for mitochondrial-based PD, and implicate disrupted respiratory chain function as a likely causative driver.

3.2 Introduction

Mitochondria have long been hypothesized to play a central role in the pathophysiology of PD. In PD, mitochondrial complex I and other respiratory chain enzyme function decrease specifically in the substantia nigra pars compacta (SNc), including DA neurons that degenerate. Additionally, mutations in mitochondrial DNA accumulate at a faster rate in SNc DA neurons in PD than in normal aging. These changes show that mitochondria are disrupted in PD. Moreover, neurotoxin data suggest that SNc DA neurons are preferentially vulnerable to mitochondrial complex I dysfunction. Exposure to the mitochondrial complex I inhibitor rotenone increases the risk of developing PD, and promotes selective DA neuron death in rats, while exposure to another mitochondrial complex I inhibitor (1-methyl-4-phenyl-1,2,3,6-tetrahydropyridine, MPTP) produces a parkinsonian syndrome in humans, monkeys and rats.

Although the above neuropathologic and neurotoxin data implicate mitochondria in PD pathophysiology, they do not establish that changes in mitochondria actually cause PD. As such the discovery that mutations in the mitochondrial protein PINK1, and the mitochondria-associated proteins Parkin and DJ-1 cause familial forms of PD are particularly important in proving that mitochondrial dysfunction can cause PD. Moreover, the roles of PINK1 and Parkin in promoting mitochondrial turnover, mitochondrial respiration and bioenergetics reveal potential mechanisms by which mitochondria may

cause PD. Nonetheless, patients with autosomal recessive PD due to mutations in Parkin usually lack Lewy bodies, while there are very few neuropathologic reports from patients with PINK1 and DJ1 mutations and have relatively benign disease courses with few if any cognitive deficits, leading many investigators to hypothesize that autosomal recessive forms of PD are distinct disease subtypes from autosomal dominantly-inherited and sporadic forms of PD that more closely resemble each other [45].

As such, the discovery that mutations in the mitochondrial cristae protein CHCHD2 (coiled-coil-helix-coiled-coil-helix domain containing 2) cause an autosomal dominant form of late-onset PD that closely resembles sporadic PD [17], including widespread synuclein deposition [46], provides a potentially critical link proving that mitochondrial dysfunction can indeed cause a late onset form of PD that is typical of both sporadic PD and autosomal dominant PD, while also providing an important opportunity to learn how mitochondrial dysfunction can cause PD. Understanding how mutations in CHCHD2 promote PD has proven challenging, however. Although CHCHD2 may in some way support respiration [47-49], its physiologic functions remain unknown, especially in vivo. Moreover, mice lacking CHCHD2 have only subtle phenotypes [50, 51], suggesting that CHCHD2 mutations may produce toxicity through a gain of a toxic function. Indeed, mutations in CHCHD10, CHCHD2's paralog and binding partner, appears to produce toxicity through gain of function, suggesting that CHCHD2 may have similar effects [52].

A major factor limiting PD research continues to be a lack of mouse models of monogenic PD that produces dysfunction and preferential degeneration in nigrostriatal dopamine neurons, the pathologic hallmark of PD.

3.3 Results

CHCHD2 T61I mice generation and genotyping

CHCHD2 p.T61I mice were made with CRISPR/Cas9 genome-editing (Fig. 3.1, A). Specifically, two sgRNAs were used to remove the entire exon 2 and exon 3, and a targeting donor vector was used to deliver the cytosine-to-thymine mutation, resulting in the codon change from threonine to isoleucine. This approach allowed us to specifically target CHCHD2 without affecting Zbed5, which has significant homology to CHCHD2 in rodents [53]. A silent cytosine-to-guanine mutation 2 nucleotides immediately upstream was also introduced for genotyping purpose.

Due to signal overlap from Zbed5 in Sanger sequencing, we used qPCR to perform SNP genotyping of the mice (Fig. 3.1, B). Different genotypes were distinguished using WT and mutant probes based on clustering. We also used LC-MS/MS of total brain protein lysates as an orthogonal approach to distinguish WT and mutant peptides (Fig. 3.1, C).

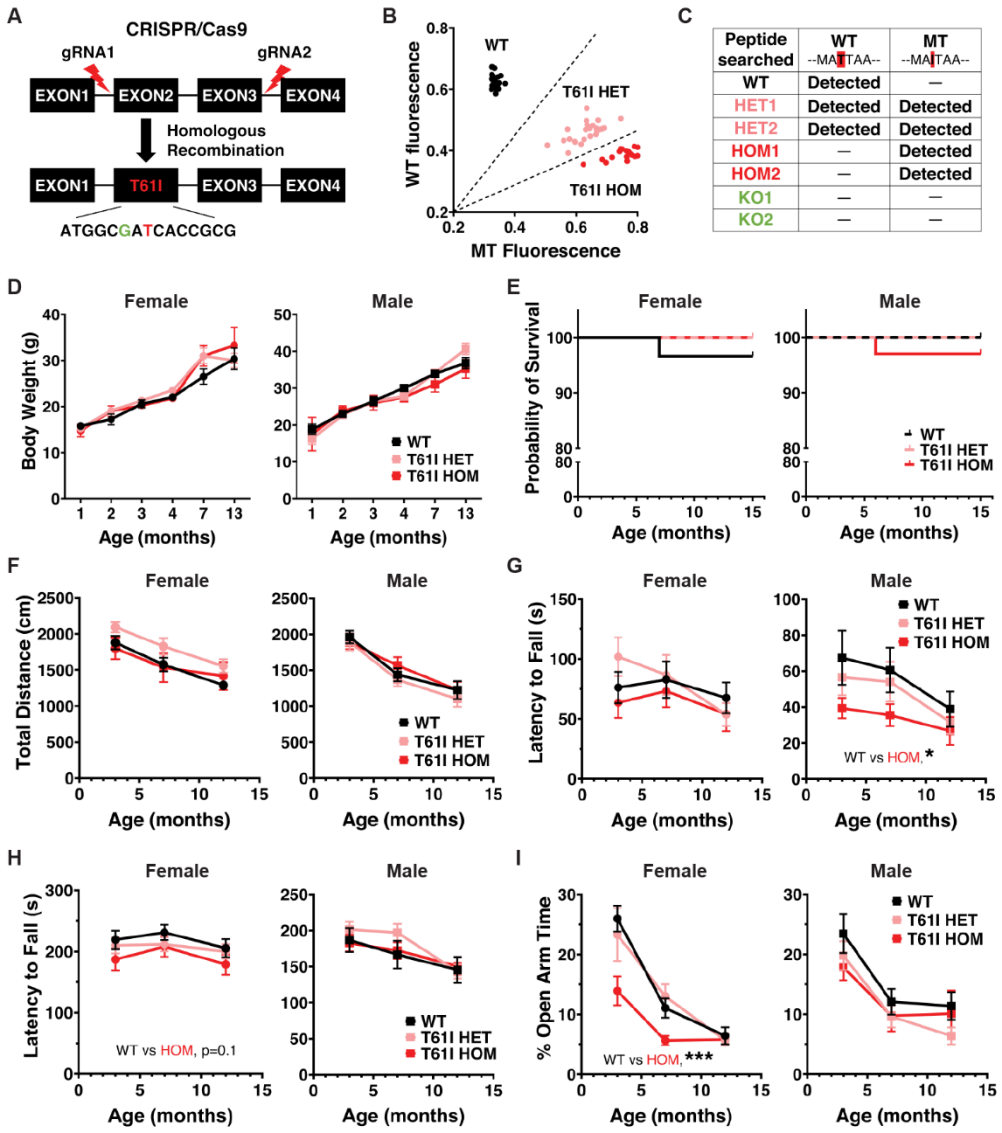

Figure 3.1: CHCHD2 T61I mice exhibit normal survival and subtle motor deficits. (A) Insertion of CHCHD2 T61I point mutation by CRISPR/Cas9 gene editing and homologous recombination. **(B)** CHCHD2 T61I mouse SNP genotyping by qPCR. 3 clusters were autogenerated by allelic discrimination in the analysis software, including WT (black), T61I HET (pink) and T61I HOM (red). **(C)** WT peptide (MAQMA**T**TAAGVAVGSAVGHTLGHAITGGFSGGG SAEPAKPDITYQEPQGAQL) and mutant peptide (MAQMA**I**TAAGVAVGSAVGHTLGHAITGGF) were searched in brain lysates of 7 mice of different genotypes (1 WT, 2 T61I HET, 2 T61I HOM and 2 CHCHD2 KO). WT peptide was found in WT and HET mice, while mutant was found in HET and HOM mice. Neither peptide was found in KO mice. **(D)** CHCHD2 T61I mice showed similar body weights compared with WT through 13 months of age. Data represent mean ± SEM. N = 5-9 mice/genotype/gender. **(E)** T61I mice showed normal survival compared with WT in Kaplan-Meier survival curve through 16 months of age. Left, females (n = 30 WT, 18 HET and 17 HOM); right, males (n = 21 WT, 20 HET, 34 HOM). **(F)** Total movements of T61I mice were normal in open field test. **(G)** Male T61I HOM mice showed a significant decrease in latency to fall in inverted grid hang (WT vs HOM $P = 0.046$, *). **(H)** Female T61I HOM mice showed a trend toward a decrease in latency to fall in the accelerating rotarod test at (WT vs HOM $P = 0.12$). **(I)** Female

HOM showed significantly lower time spent in the open arms (WT vs HOM $P < 0.001$, ***). In all behavioral studies (F-I), data represent mean ± SEM. N = 16 WT, 16 HET and 13 HOM (female), or 14 WT, 18 HET and 17 HOM (male). *$P < 0.05$, ***$P < 0.001$ by linear mixed effects analysis.

CHCHD2 T61I mice show normal lifespan and subtle motor deficits

CHCHD2 p.T61I mice were born in normal Mendelian proportions (WT: 26.9%, HET: 42.6%, HOM: 30.6%, n=108), and had similar body weights to littermate controls through 13 months of age (Fig. 3.1, D). Survival was also unchanged through 16 months (Fig. 3.1, E). A small subset of mice tracked for 23 months also failed to show any effects on survival (SFig. 3.1, A). We next assessed if the CHCHD2 T61I mutation disrupts motor function. T61I homozygous and heterozygous mutation had no overall effects on total movement in open field testing across the three time points (3, 7 or 12 months) (Fig. 3.1, F). Repeat open field testing with the automated tracking system, EthoVision XT, on a small cohort of 23-month-old male mice also failed to show differences in total movement or time spent moving (SFig. 3.1, B and C). Although total movement wasn't affected, male (but not female) homozygous T61I mice exhibited a significantly shorter latency to fall in inverted grid hang test (Fig. 3.1, G). In rotarod testing, CHCHD2 homozygous T61I females (but not males) had a trend for decreased latency to fall versus controls (Fig. 3.1, H). In the elevated plus maze, female T61I homozygous mutants showed a trend level decrease in distance traveled (SFig. 3.1, D). Overall, these findings are consistent with subtle motor deficits in the T61I mice, with no evidence of progression with older age. In contrast, analysis of the motor function of CHCHD2 T61I heterozygous mice failed to uncover any significant differences in the various behavioral assessment (Fig. 3.1, F and G; SFig. 3.1, B and C).

Notably, mice with the T61I mutation also showed evidence of nonmotor changes. In elevated plus maze testing, female homozygous T61I mice spent significantly less time in the open arms, showed decreased open arm/total distance percentage, and entered the open arms fewer times, consistent with increased anxiety (Fig. 3.1, I; SFig. 3.1, D).

Electrophysiology reveals changes in response to dopamine receptor agonist in CHCHD2 T61I point mutation mice

We next assessed if the T61I mutation impacts the somatodendritic physiological health of SNc DA neurons. Ex vivo whole cell recordings in 23-month-old male mice blind to genotype showed that basic physiological properties of SNc DA neurons in PM mice were similar to those in control SNc neurons. Most DA neurons fired spontaneously in a regular, pacemaker fashion both in cell attached and whole cell configuration (Fig. 3.2, A; SFig. 3.2, A, B and C). However, SNc DA neurons from CHCHD2 T61I mice lacked dopamine D2 receptor (D2R) autoreceptor hyperpolarization (Fig. 3.2, B). On average, action potentials in DA neurons from the T61I mice also had a less depolarized peak compared to controls (Fig. 3.2, C). A parallel but not significant pattern was observed in action potential threshold (Fig. 3.2, D). A small population of DA neurons from the T61I mice showed less regular firing (and increase in the coefficient of variation of interspike

intervals) compared to WT DA neurons (Fig. 3.2, A). I_h magnitude and input resistance distributions were also similar between SNc DA neurons from WT and T61I mice (SFig. 3.2, E and F).

The lack of D2R agonist induced hyperpolarization may be due to one or more of the following factors: downregulation of D2R, downregulation of G protein receptor gated inwardly rectifying K+ channels, or D2R coupling changing to an alternative signaling pathway. Kikima *et al* showed that dopamine release in the SNc functions specifically in an autoinhibition manner, activating D2Rs on the receptor that released the dopamine [54].

To further assess the impact of the CHCHD2 T61I mutation on dopamine metabolism, we assessed catecholamine levels in the dorsal striatum. T61I homozygous mice at 16 months showed a trending lower level in dopamine level compared with WT mice, but was significantly lower than T61I heterozygous mice (SFig. 3.2, G).

CHCHD2 T61I mutation does not lead to significant DA neuron degeneration

We next examined if the T61I mutation leads to DA neuron degeneration. First, to assess the integrity of DA neuron terminals, we quantified TH expression in the striatum using DAB staining. There was no significant effect of either heterozygous or homozygous T61I mutation on TH optical density in the striatum of 16 months old mice (Fig. 3.2, E). A repeat on 23-month-old male mice also revealed no difference between the T61I and WT mice (SFig. 3.2, H). We then performed stereology to quantify the number of DA neurons in the midbrain, and similarly there was no significant loss of DA neurons in either the SN or VTA (Fig. 3.2, F).

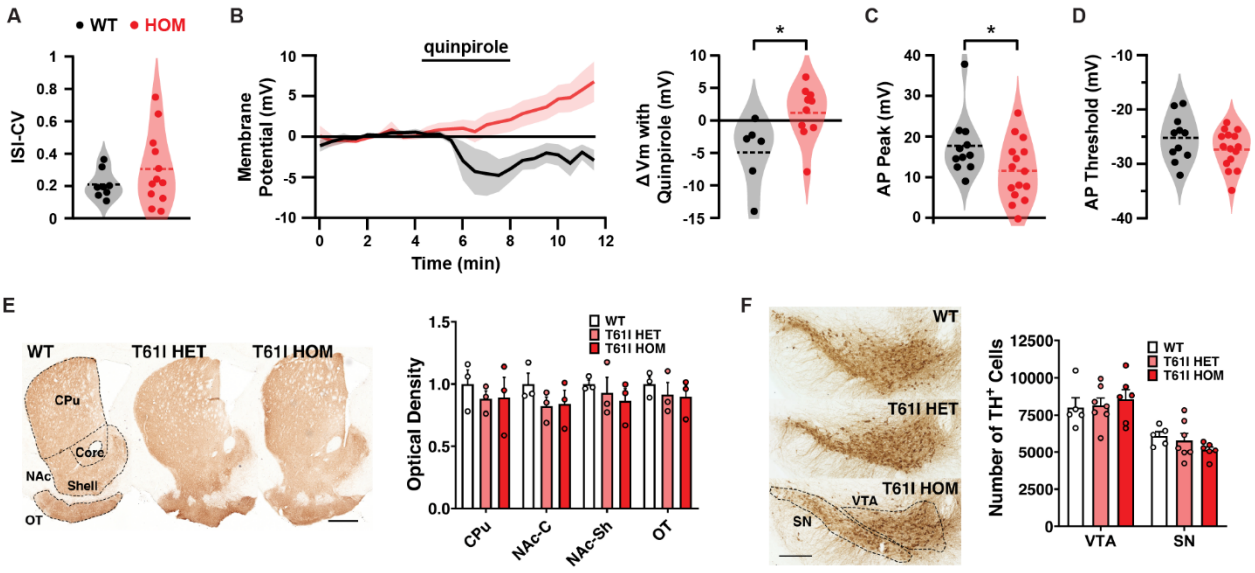

Figure 3.2: CHCHD2 T61I point mutation disrupts response to dopamine receptor agonist without DA neuron degeneration at 16 months. (A-D) SNc dopamine neurons from CHCHD2 T61I mice lack a D2R induced hyperpolarization. **(A)** Regularity of spontaneous firing in whole cell current clamp configuration was evaluated by measuring the coefficient of variation of 100

consecutive interspike intervals at the initiation of whole cell access. ISI-CV, coefficient of variation of interspike intervals. **(B)** The D2R selective agonist quinpirole (1 uM) was bath applied during whole cell recordings of SNc DA neurons. Quinpirole caused hyperpolarization in most WT neurons but not T61I mutant neurons. Left, time course of response; right, summary of individual responses. **(C, D)** Spontaneous AP waveforms were recorded in whole cell configuration and quantified from each genotype including AP peak (C) and threshold (D). AP, action potential. N = 5 WT and 4 HOM male mice at 23 months. Data represent mean ± SEM or with kernel density estimations. For all data parametric assumptions were tested to choose between t-test (parametric) or permutation (non-parametric) analysis. *P < 0.05. **(E)** Representative images of TH immunoreactivity in striatal sections of WT, T61I HET and HOM mice at 16 months. DA neuron projection areas in dorsal and ventral striatum are indicated with dotted lines. CPu, caudate putamen; NAc, nucleus accumbens; OT, olfactory tubercule. Quantification for TH immunoreactivity showed no difference in WT, HET and HOM by two-way ANOVA with Tukey's *post hoc* test. Data represent mean ± SEM. N = 3 animals/group, 4 sections/animal. Scale bar indicates 300 µm. **(F)** Representative images of TH immunoreactivity in midbrain sections of WT, HET, and HOM mice at 16 months. DA neuron projection areas in the midbrain are indicated with dotted lines. SN, substantia nigra; VTA, ventral tegmental area. Stereology estimating the number of DA neurons showed no difference between each group by two-way ANOVA with Tukey's *post hoc* test. N = 5-7 animals/group. Data represent mean ± SEM. *P < 0.05, **P < 0.01, ***P < 0.001, Scale bar indicates 300 µm.

T61I point mutation preferentially increases the mitochondrial accumulation of CHCHD2 and CHCHD10 in SN but not VTA DA neurons

CHCHD2 forms soluble homodimers and heterodimers with CHCHD10 in mitochondria under physiological conditions [55]. Moreover, homodimers and heterodimers containing T61I CHCHD2 are less soluble and more prone to aggregate [48, 49, 55, 56]. To assess the effects of the T61I mutation on the level and spatial organization of CHCHD2, we used super-resolution microscopy. First, we found that T61I point mutation did not change the overall level of CHCHD2 expression in either SN or VTA DA neurons (Fig. 3.3, A and B). Similarly, the total level of CHCHD10 expression was comparable in T61I CHCHD2 and WT controls.

However, both heterozygous and homozygous T61ICHCHD2-expressing DA neurons had markedly increased numbers of CHCHD2 and CHCHD10 punctae, specifically in the SN, and not the VTA. Here punctae are defined as foci of CHCHD2 or CHCHD10 immunofluorescence that are significantly brighter than adjacent areas, and hence could represent either CHCHD2 and CHCHD10 aggregation, or focal areas of increased CHCHD2 and D10 levels in mitochondria.

Since both CHCHD2 and CHCHD10 are predominantly localized to the mitochondrial intermembrane space [55], we next assessed if T61ICHCHD2 impacts the mitochondrial content in either SNc or VTA DA neurons. However, T61CHCHD2 heterozygous and homozygous DA neurons had similar mitochondrial content (Fig. 3.3, C and D) as controls, based on immunofluorescence against the inner mitochondrial marker PDH. In addition, essentially all T61ICHCHD2 and wtCHCHD2 co-localized with mitochondria (SFig. 3.3,

B). Interestingly, there was an increase in the number of CHCHD2 punctae within mitochondria in T61ICHCHD2 DA neurons specifically in the SNc.

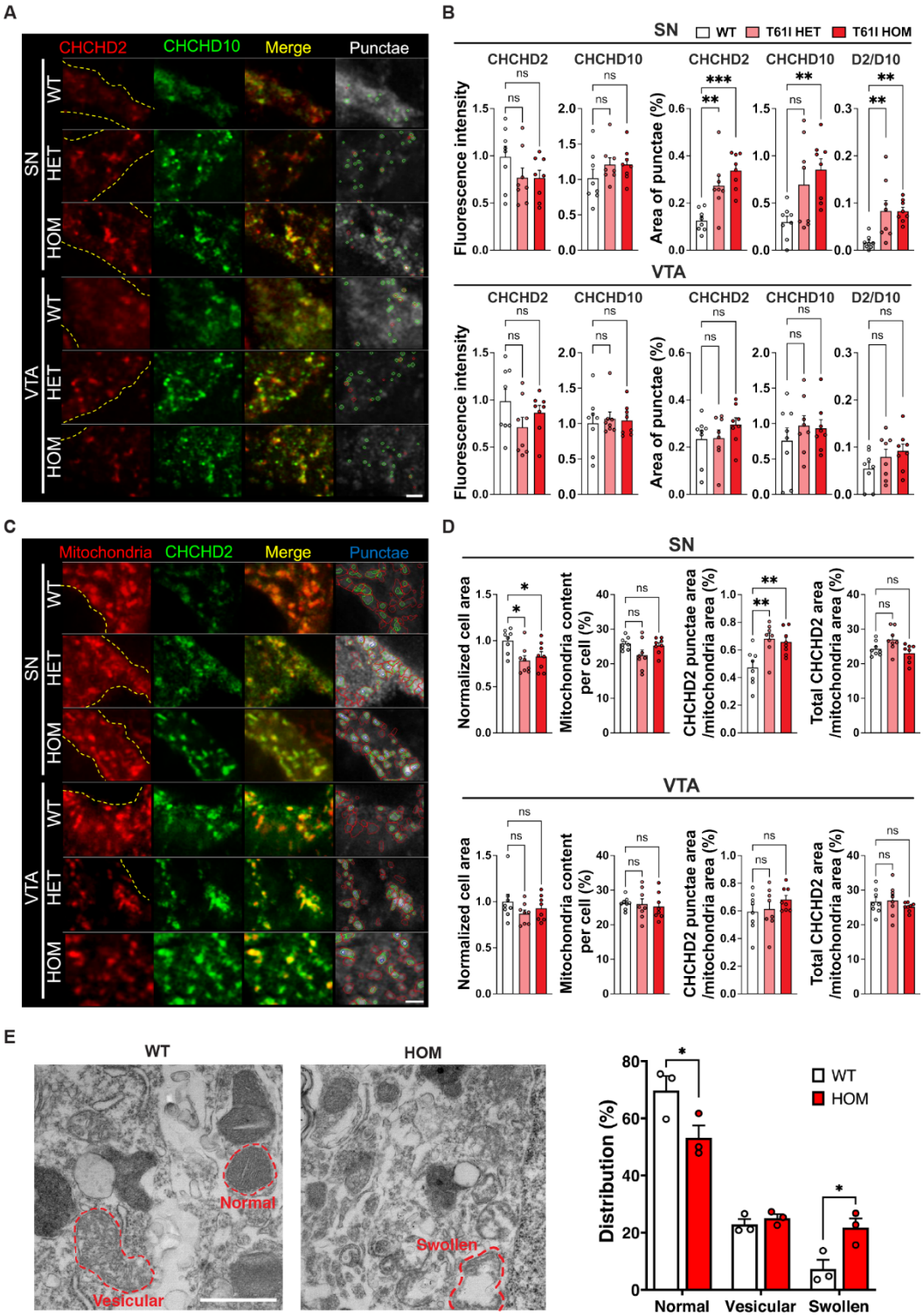

Figure 3.3: T61I point mutation preferentially increases accumulation of CHCHD2 and CHCHD10 in mitochondria in SN DA neurons. (A) Representative fluorescence images of

CHCHD2 (red), CHCHD10 (green), and merge in SN (top) and VTA (bottom) subregions in the midbrain of CHCHD2 T61I mice. Punctae was semi-automatically annotated by Cellprofiler. CHCHD2 denoted in red and CHCHD10 in green. The region of cell body is indicated with dotted lines, based on TH signal. **(B)** Quantification of CHCHD2 and CHCHD10 intensity, area of CHCHD2 and D10 punctae, and area of co-localizion between CHCHCHD2 and D10 punctae in SN (top panel) and VTA (bottom), normalized to the averaged cell area of each group. **(C)** Representative fluorescence images of mitochondria (PDH, red), CHCHD2 (green), and merge in SN (top) and VTA (bottom). PDH denoted in red, total CHCHD2 in green and CHCHD2 punctae in blue. The region of cell body is indicated with dotted lines, based on TH signal. **(D)** Quantification of cell area, mitochondrial content, CHCHD2 punctae area in the mitochondrial, and total CHCHD2 level in the mitochondria in SN (top panel) and VTA (bottom), normalized to averaged cell area of each group. In all fluorescence staining (A-D), n = 6-8 randomly selected TH-positive cells from 6 fields in each region in each mouse, 4 mice/genotype. Data represent mean ± SEM. **P* < 0.05, ***P* < 0.01, ****P* < 0.001 by one-way ANOVA with Tukey's *post hoc* test, Scale bars indicate 1μm. **(E)** Impact of T61I mutation on mitochondrial morphology. DA neurons were labeled with primary TH antibody followed by secondary gold particle-conjugated antibody. N = 71 – 189 mitochondria/mouse, 3 mice/genotype. Data represent mean ± SEM. ***P* < 0.01 by *t* test with Welch's correction. Images taken at 19,000X magnification, and scale bar indicates 1 μm.

As expected, the majority of CHCHD2 fluorescence including CHCHD2 punctae (identified based on their higher fluorescence), was within mitochondria (Fig. 3.3, D; SFig. 3.3, A). In contrast, the number of mitochondrial CHCHD2 punctae was increased specifically in the SN in T61I HOM mice but not in the VTA. Collectively, these results indicate that the CHCHD2 mutant leads to the preferential accumulation of CHCHD2 and CHCHD10 in mitochondria in SN DA neurons.

To gain insight into whether the accumulation of CHCHD2 punctae reflects a change in CHCHD2 protein solubility, for instance due to CHCHD2 aggregation, we performed western blots on cytosolic and mitochondrial fractions from total brain lysates of 13-month-old mice (SFig. 3.3, B). T61ICHCHD2 mice had relatively increased levels of insoluble versus soluble CHCHD2 in both cytosolic and mitochondrial fractions, with the latter being more prominent, suggesting aggregation of T61ICHCHD2 within mitochondria.

Mutant T61I CHCHD2 Disrupts Mitochondria in DA Neurons

The accumulation of T61I CHCHD2 mutant and CHCHD10 within mitochondria suggests potential disruption of mitochondria. To address whether mitochondrial cristae was affected by protein accumulation, we labeled DA neurons using immunogold staining and assessed the mitochondrial ultrastructure. Following the definition by Paredes and colleagues [57], we categorized mitochondrial morphology into 3 groups: normal, vesicular, and swollen. Compared with WT mice, T61I HOM mice showed a significant decrease in normal form and a significant increase in swollen form of mitochondria in DA neurons (Fig. 3.3, E), indicating mitochondrial damage by CHCHD2 T61I mutation.

Altered expression level of CHCHD2 in vulnerable DA neurons in PD

The change in the distribution and solubility of CHCHD2 in SNc DA neurons from T61ICHCHD2 mice suggests that changes in CHCHD2 level or conformation could contribute to disease pathophysiology. To determine whether CHCHD2 expression also changes in sporadic PD, we used spatial genomics (GeoMx WTA) to compare CHCHD2 gene expression in DA neurons in midbrain samples from patients with sporadic PD and age-matched human controls (Fig. 3.4, A). Interestingly, in controls, transcriptomic levels of both CHCHD2 and CHCHD10 were increased in more vulnerable DA neurons in the ventral tier of the SN (SNV), when compared with the more resilient DA neurons in the dorsal tier (SND). Considering that DA neurons in both mice and humans have increased levels of both CHCHD2 and CHCHD10 [50], these findings are consistent with the possibility that increased CHCHD2 contributes to the preferential vulnerability of SNV DA neurons.

Interestingly, the increased CHCHD2 gene expression in ventral tier DA neurons was no longer present in patients with early PD (ePD) who had a dramatic decrease in gene expression in DA neurons in the SNV, but not SND (Fig. 3.4, A), raising the possibility that these higher CHCHD2-expressing DA neurons were lost or that CHCHD2-expression in DA neurons decrease as they begin to degenerate. The latter possibility is supported by the finding that CHCHD2 expression is also decreased in SNV DA neurons form individuals with incidental Lewy bodies (ILBD) that have a normal complement of SNV DA neurons. Notably, this relationship disappeared in the late Lewy pathological stage of PD, where the remaining DA neurons in the SNV tended to have elevated levels of CHCHD2 expression, although the results were highly variable (coefficient of variation = 167.6%). The decrease in CHCHD2 level could reflect a downregulation of CHCHD2 expression early in PD, and the persistence of primarily higher CHCHD2-expressing DA neurons in late PD might indicate that those DA neurons with lower CHCHD2 ultimately die.

The finding of extensive α-synuclein aggregation in a patient with CHCHD2 T61I mutation suggests that mutant CHCHD2 may promote α-synuclein aggregation [46]. To gain insight into the relationship between mutant T61I CHCHD2 and synuclein, we first examined the relationship between CHCHD2 and SNCA gene expression by spatial transcriptomics. As with CHCHD2, SNCA expression in controls was higher in DA neurons in the most PD-vulnerable ventral tier (SNV, 238.80 ± 131.32) than those in the dorsal tier (SND, 130.78 ± 130.86, $P < 0.001$). Considering the known pathogenicity of increased WT α-synuclein [58], this suggests that increased α-synuclein levels may contribute to the preferential vulnerability of ventral tier DA neurons. Interestingly, when pooling all samples (Fig. 3.4, B), regression tests indicated positive linear associations between the level of SNCA and CHCHD2 (R2 = 0.270, F (1,226) = 83.74, $P < 0.001$) as well as between the level of SNCA and CHCHD10 (R2 = 0.279, F (1,226) = 87.51, $P < 0.001$), perhaps reflecting the co-aggregation of the two PD-associated proteins.

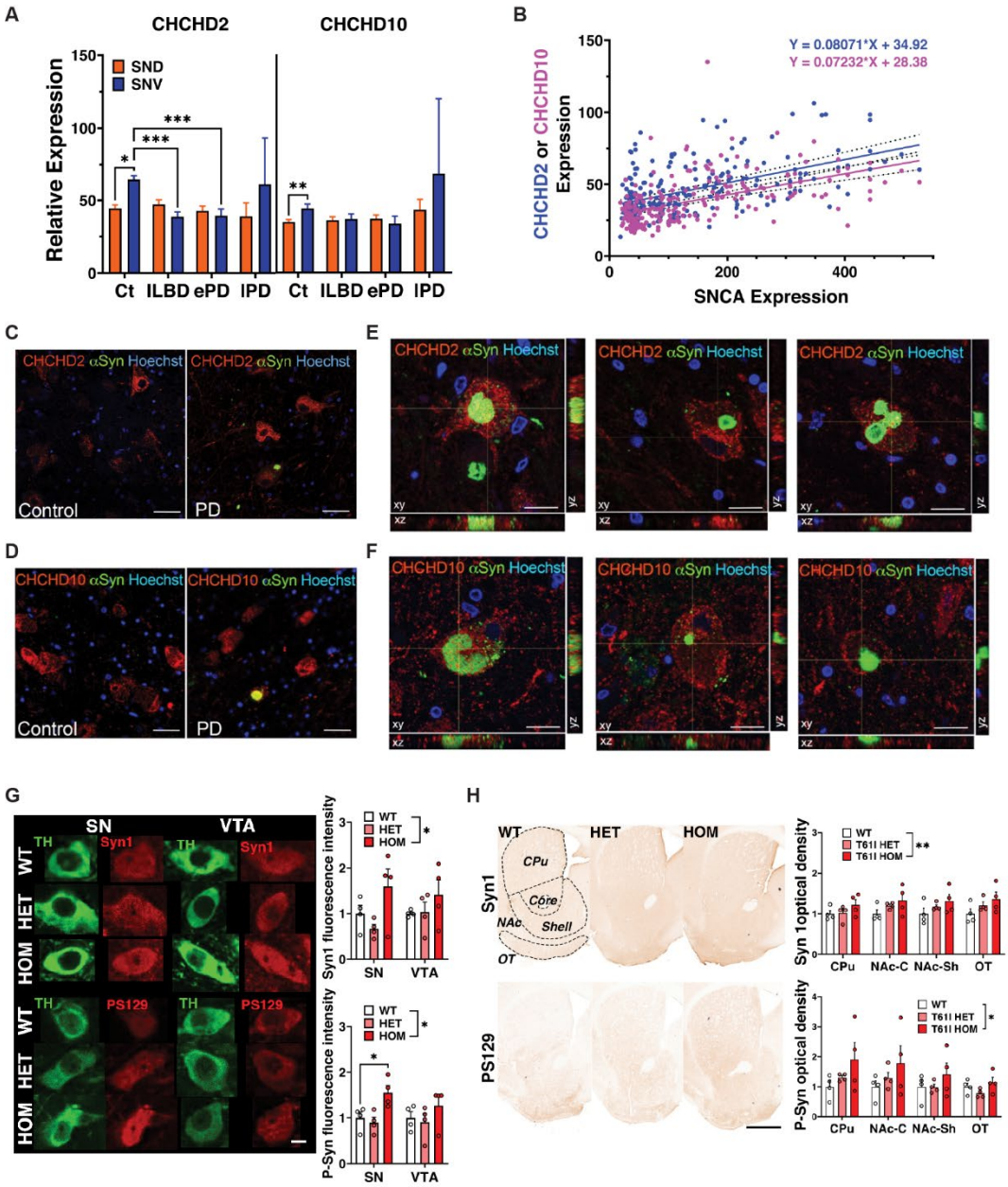

Figure 3.4: CHCHD2 T61I mice show increases in α-synuclein and phosphorylated synuclein level in the midbrain. (A) Transcriptomic levels of CHCHD2 and CHCHD10 in DA neurons of SND (dorsal tier of substantia nigra, orange) and SNV (ventral, blue) measured with GeoMx WTA show significant downregulation of CHCHD2 in the SNV of ILBD and ePD. Data represent mean ± SEM. Brown-Forsythe and Welch ANOVA tests were applied for data covariates with age, sex, and post-mortem delay. ****P* < 0.001. NC, normalized counts; Ct, control; ILBD, incidental Lewy body disease; ePD, PD with early Braak stage pathology; lPD, PD with late Braak stage pathology. **(B)** Moderate positive linear associations were revealed between expression levels of either CHCHD2 or CHCHD10 with SNCA in the SN by Spearman correlation. **(C)** CHCHD2 expression in control and PD SN DA neurons and **(E)** orthogonal views of the relative location of CHCHD2 in different staged αSyn aggregations. **(D)** CHCHD10 expression in control and PD SN DA neurons, and **(F)** orthogonal views of the relative location of CHCHD10 in

different staged αSyn aggregations. Scale bars represent 50 μm in (C, D), and 20 μm in (E, F). **(G)** Representative images and quantifications of TH (green) and P-syn (PS129, red) immunoreactivity in SN and VTA at 63X magnification in midbrain sections of WT, HET and HOM mice at 16 months. Syn1 and P-syn immunoreactivities increase in both total synuclein and p-Syn in midbrain DA neurons of HOM mice by two-way ANOVA with Tukey's *post hoc* test. Data represent mean ± SEM. **P* < 0.05. N = 4 sections/mouse, 4 mice/genotype. Scale bar indicates 10 μm. **(H)** Representative images and quantifications of α-synuclein (Syn1, top) and phosphorylated synuclein, P-syn (PS129, bottom), immunoreactivity in striatal sections of mice at 16 months. Syn1 and P-Syn areas in dorsal and ventral striatum are indicated with dotted lines. Significant increases in both Syn1 and p-Syn immunoreactivity were observed in HOM mice compared with WT by two-way ANOVA with Tukey's *post hoc* test. Data represent mean ± SEM. **P* < 0.05, ***P* < 0.01. N = 4 sections/mouse, 4 mice/genotype. Scale bar indicates 300 μm.

CHCHD2 and CHCHD10 accumulate in αSyn aggregates in SNc dopamine neurons in sporadic PD

To further examine the relationship between CHCHD2 and α-synuclein, we next compared CHCHD2 localization in SNc dopamine neurons from individuals with incidental Lewy bodies (ILB), patients with early and advanced sporadic PD, and age-matched controls. As expected, both CHCHD2 and its binding partner CHCHD10 had a predominantly punctate localization throughout the cytosol in SNc DA neurons from both control and PD patients (Fig. 3.4, C and D), consistent with a mitochondrial localization. Interestingly, in PD samples, there was also robust accumulation of CHCHD2 (n=74 Lewy bodies, Fig. 3.4, E) and CHCHD10 (n=88 Lewy bodies, Fig. 3.4, F) punctae within and/or surrounding early-stage Lewy bodies, suggesting that both CHCHD2 and CHCHD10 aggregate within Lewy bodies, presumably as part of degrading mitochondria that are observed in early Lewy bodies. In contrast, CHCHD2 and CHCHD10 were no longer visible in more mature Lewy bodies, consistent with Lewy bodies being a sink that degrades mitochondria including CHCHD2.

Given the above correlations between CHCHD2 and α-synuclein gene expression and the accumulation of CHCHD2 and CHCHD10 in Lewy bodies in pre-symptomatic and early PD, we next examined if α-synuclein accumulates and aggregates in the CHCHD2 T61I mutant mice. We first performed western blots on the cortex of 16-month-old mice. However, there was no change in α-synuclein levels in either the serially extracted Triton-soluble or SDS-soluble fractions (SFig. 3.4).

To assess if the T61I mutation impacts synuclein levels specifically in midbrain DA neurons, we next assessed α-synuclein and phosphorylated synuclein levels specifically in midbrain DA neurons using immunofluorescence (Fig. 3.4, G). Quantification revealed an increase in P-Syn levels in homozygous SNc DA neurons. Non-phosphorylated α-synuclein levels were also increased overall in homozygote midbrain DA neurons. Moreover, both α-synuclein and phosphorylated synuclein were increased in the striatum of homozygous T61I mice at 16 months by optical density, while heterozygotes did not reach significance (Fig. 3.4, H). Therefore, T61I homozygous mice accumulate increased

levels of both total and phosphorylated α-synuclein in both the cell body and striatum. However, further investigation is required to determine if SNc DA neurons in heterozygous T61I mice also accumulate increased α-synuclein at older age, and also whether the increase in the striatum reflects changes in midbrain DA axons versus striatal target neurons. Similarly, it will be important to clarify whether the lack of accumulation in cortical brain lysates truly reflects a selective predisposition to accumulate α-synuclein in midbrain DA neurons and the striatum, or simply reflects a lower sensitivity of the western blot approach to detect changes in α-synuclein level. Further studies are needed to understand the mechanisms by which mutant CHCHD2 affects synuclein levels in midbrain DA neurons.

CHCHD2 mutant mouse brains exhibit a metabolic shift toward glycolysis and PPP

The accumulation of T61I CHCHD2 mutant and CHCHD10 within mitochondria, as well as the disruption of mitochondrial morphology suggests that mutant T61I CHCHD2 mutant may disrupt mitochondrial function. Previous studies have highlighted a metabolic switch from mitochondrial respiration to glycolysis as a compensatory mechanism to sustain cellular ATP in the context of mitochondrial dysfunction [59]. Notably, recent work with a DA neuron-specific complex I deficiency mouse model revealed a robust upregulation of glycolytic genes in DA neurons by RNAseq [60]. Similarly, pronounced elevation of both glycolytic gene mRNA and protein levels were also found in the heart of CHCHD10 point mutant mice [61]. To determine if mutant CHCHD2 disrupts energy metabolism, we performed targeted and untargeted metabolomics where mice were infused with [U-^{13}C]glucose for 30 minutes before harvest.

Remarkably, female T61I heterozygous and homozygous mice at 19 months exhibited a robust dose-dependent increase in the total level of distal glycolytic metabolites including 3-phosphoglycerate (3PG), phosphoenolpyruvate (PEP) and pyruvate (Pyr) (Fig. 5, A and B). The fractional labeling with ^{13}C was also increased across essentially all glycolytic metabolites in homozygous mice versus controls, consistent with an overall increase in brain metabolism of glucose through glycolysis (Fig. 5, A and C). T61I heterozygous and homozygous mice also showed dose-dependent increases in the fractional labeling of PPP metabolites and in relative amounts of a subset of TCA cycle metabolites. However, the fractional labeling of TCA metabolites was only subtly increased in homozygous mice versus controls, suggesting that the accumulation of TCA metabolites occurs due to a decrease (rather than increase) in the flux of glucose metabolites toward respiration. This overall increase in glucose metabolism through glycolysis and the PPP relative to the TCA cycle is thus likely secondary to a primary disruption in mitochondrial respiration.

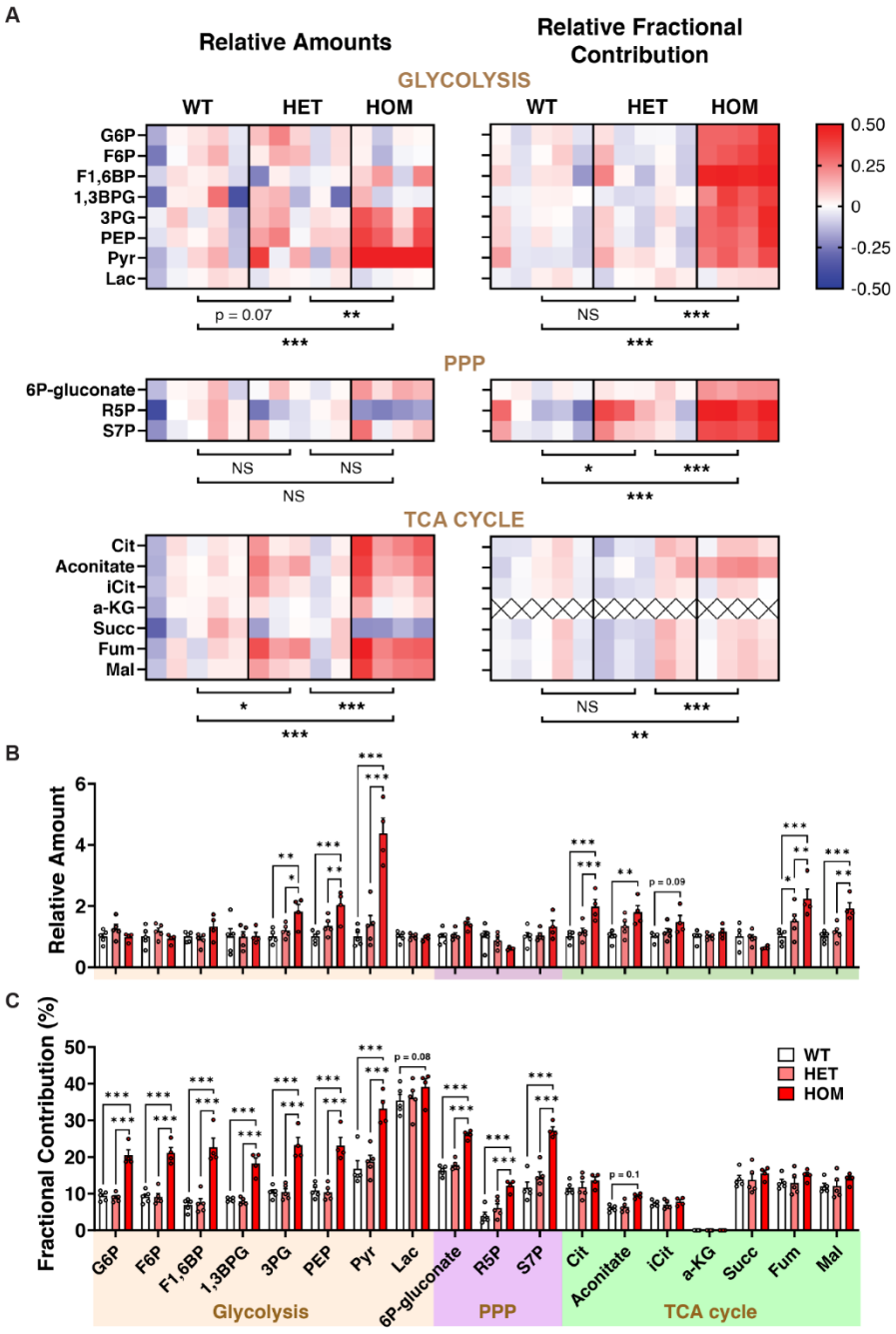

Figure 3.5: CHCHD2 mutant mouse brains exhibit a metabolic shift toward glycolysis and PPP. (A) Female CHCHD2 T61I mice at 19 months received tail vein injections of [U-^{13}C]glucose for 30 minutes before brains were harvested. Brain metabolite extract was analyzed by an ion chromatography-mass spectrometry (IC-MS) detector. Heat map shows relative total levels of metabolomics in the L column determined by non-targeted metabolomics, and fractional contribution of ^{13}C-glucose to each metabolite by targeted metabolomics on the R. Each square shows the log value of a metabolite level or fractional contribution in a mouse normalized to the mean of the WT group. **(B)** Bar graph of relative amounts of metabolites along glycolysis, PPP and TCA cycle. CHCHD2 T61I heterozygotes and homozygotes showed a dose-dependent

increase in distal glycolytic, PPP and TCA cycle metabolites compared with WT mice. **(C)** Bar graph of fractional contribution of metabolites. CHCHD2 T61I homozygous mice showed significantly higher labeling percentages in glycolytic and PPP metabolites compared with WT mice. G6P, glucose 6-phosphate; F6P, fructose 6-phosphate; F1,6BP, fructose 1,6-bisphosphate; 1,3BPG, 1,3-bisphosphoglycerate; 3PG, 3-phosphoglycerate; PEP, phosphoenolpyruvate; Pyr, pyruvate; Lac, lactate; R5P, ribose 5-phosphate; S7P, sedoheptulose 7-phosphate; Cit, citrate; iCit, isocitrate; a-KG, α-ketoglutarate; Succ, succinate; Fum, fumarate; Mal, malate. Data represent mean ± SEM. N = 5 WT, 5 HET and 4 HOM T61I female mice at 19 months. **P* < 0.05, ***P* < 0.01, ****P* < 0.001 by two-way ANOVA with Tukey's *post hoc* test.

Spatial transcriptomics revealed different impacts on glycolytic and respiratory chain genes in DA neurons in the VTA of CHCHD2 T61I versus CHCHD2 KO mice

To investigate how CHCHD2 impacts gene expression in DA neurons, we performed spatial genomics (Visium Spatial Gene Expression,10X Genomics) on midbrain sections from 16-month-old CHCHD2 T61I and from 13-month-old CHCHD2 KO mice. Disks demarcating areas of gene expression analysis were selected within the SN and VTA, based on containing at least one entire TH-positive neuron and also expressing characteristic DA genes (DAT, VMAT2, or TH) above a pre-set threshold level (SFig. 3.5, A and B). We first examined selected pathways, including glycolysis, pentose phosphate pathway, respiratory chain and integrated stress response. Both T61I CHCHD2 and knockout showed significant effects on the metabolic pathways (SFig. 3.5, C and D). The glycolytic pathway was downregulated in the VTA of CHCHD2 KO mice, while unaffected in CHCHD2 T61I mice (SFig. 3.5, E). In contrast, expression level of nearly every component in complex I and III was decreased in the VTA of CHCHD2 T61I mice, but had subtle effects in the KO mice (SFig. 3.5, F and G). Nonetheless, these distinctions were not observed in SN DA neurons (SFig. 3.6, A), perhaps due to the limited resolution of Visium in accurately characterizing the less densely populated cell bodies in the region.

We then performed untargeted analyses to identify individual hits and pathways in these mice. Genes ranking within the top 20 percent of significantly altered ones in either the SN or VTA of the CHCHD2 T61I mice were carefully reviewed (SFig. 3.6, B). Surprisingly, none of these genes was within the top 20 percent hits in the SN and VTA of CHCHD2 KO mice, and vice versa (SFig. 3.6, C). This implies T61I CHCHD2 exerts different mechanisms than that of CHCHD2 KO. Among genes with the most pronounced changes in CHCHD2 T61I mice (SFig. 3.6, B), we identified three shared hits in both the SN and VTA: Zfand6, Lrmda and Apobec1 (SFig. 3.6, D). Zfand6 (zinc finger AN1-type containing 6, also known as AWP1), is a key mediator of TNF-α signaling and negatively regulates NF-κB [62-64]. Little is known about Lrmda (leucine rich melanocyte differentiation associated, also known as C10orf11), but mutations in this gene cause oculocutaneous albinism. Apobec1 is a cytidine deaminase enzyme which edits transcripts in various tissues including macrophages and dendritic cells. Deletion of Apobec1 in microglia in mice can exacerbate age-related neurodegeneration [65]. These genes did not show similar trends in the CHCHD2 KO mice versus their littermate controls. Additionally, we

also performed pathway analysis on the CHCHD2 T61I mice using the GSEA tool, but none passed the false discovery threshold of 0.25.

Human spatial transcriptomics reproduces similar changes in selected genes in mouse SN DA neurons

To assess if gene expression changes in the SN and VTA of CHCHD2 T61I mice are replicated in the SNc in sporadic PD, we examined the expression levels of DEGs (differentially expressed genes) in incidental Lewy body disease patients (ILBD) versus healthy controls (SFig. 3.7). Since the demarcating disks included both DA neurons and surrounding cells in the mouse brains due to the limited resolution of Visium, we performed whole tissue analysis in the human samples without TH+ masking. Out of the 17 DEGs, only 8 were within our GeoMx human dataset assessing gene expression within SNV TH+ cells. Remarkedly, 7 of these genes exhibited changes in the same direction as observed in the mouse model, and one (Cox6a2) reached significance. This data supports the conclusion that CHCHD2 T61I point mutation leads to transcriptomic changes similar to those in sporadic PD.

Proteomics reveals robustly altered mitochondrial protein-protein interactions in the CHCHD2 T61I mice

To explore how mutations in CHCHD2 might impair energy metabolism and contribute to the aggregation of CHCHD2, we investigated the protein-protein interactions (PPI) of CHCHD2 in the brains of 13-month-old CHCHD2 T61I HET, T61I HOM, and CHCHD2 KO mice. We utilized co-fractionation coupled with mass spectrometry (CF-MS) to identify changes in protein complexes within whole cell and mitochondrial extracts from CHCHD2 point mutant and knockout (KO) mice brains (Fig. 3.6, A). We analyzed a total of 768 fractions using size-exclusion high-performance liquid chromatography (SEC-HPLC) followed by tandem liquid chromatography-mass spectrometry/mass spectrometry (LC-MS/MS). Following the fractionation experiments, we observed the molecular weights deduced from SEC chromatographic elution profiles were consistent. By employing hierarchical clustering on the elution profiles from both whole cell lysates and mitochondrial extracts, as determined by MS/MS, we successfully identified one-tenth of the mouse proteome and one-third of the mitochondrial proteins listed in the mouse MitoCarta database (Fig. 3.6, B). This analysis revealed distinct patterns of protein assemblies that consistently co-eluted in specific extracts. Notably, proteins involved in oxidative phosphorylation and linked to Parkinson’s disease were found exclusively in mitochondrial extracts, but not in whole cell lysates.

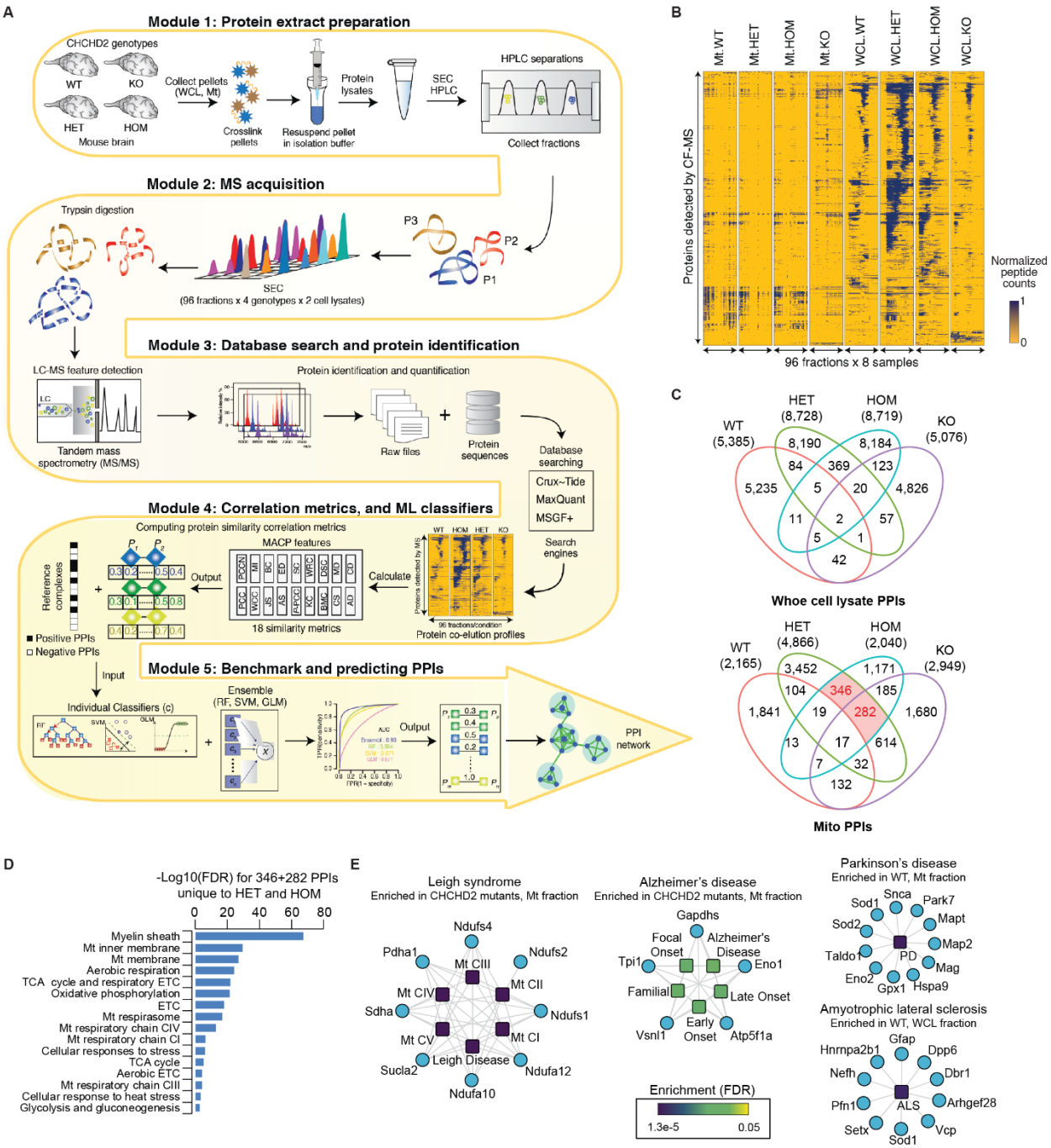

Figure 3.6: Co-fractionation mass spectrometry analysis of protein assemblies across various CHCHD2 genotypes. (A) Biochemical fractionation of whole cell lysates (WCL) and mitochondrial (mt) lysates from mouse brain with varying CHCHD2 genotypes was performed using high-performance size exclusion chromatography (SEC-HPLC). Protein fractions were subjected to tryptic digestion and analyzed by high performance liquid chromatography-tandem mass spectrometry (LC-MS/MS) to measure peptide spectral counts. The schematic details the computational scoring pipeline from our previous work in MACP. This pipeline includes calculating protein similarity (correlation) metrics for each CHCHD2 genotype, training integrative classifiers with machine learning using the CORUM mouse complex database as a training standard, and scoring co-fractionation data to predict high-confidence interactions. These predicted interactions

were clustered to define co-complex membership, and analyzed for pathobiological relevance. **(B)** Hierarchical clustering displaying changes in protein co-fractionation intensity profiles between mt and WCL as measured by LC-MS/MS. **(C)** Venn diagram illustrating the distribution of mouse protein interactions within the mt and WCL across different CHCHD2 genotypes. **(D)** Enrichment analysis of interacting proteins in mt mouse brain lysates from CHCHD2 heterozygous (HET) and homozygous (HOM) samples involved in annotated metabolic processes. **(E)** Enrichment analysis (FDR ≤ 5e-02) of protein assemblies in mt extracts from CHCHD2 point mutants, not found in wild-type, and also present in both whole cell and mitochondrial extracts of CHCHD2 wild-type but missing in mutants. These assemblies are linked to diseases such as Leigh syndrome, Parkinson's disease, amyotrophic lateral sclerosis, and Alzheimer's disease.

Utilizing our newly developed R/CRAN software [66], Macromolecular Assemblies from Co-elution Profiles (MACP), we calculated correlation scores for each co-fractionation experiment. We generated MS2 spectral count profiles across all fractions for each genotype within each cell extract, employing three distinct search engines (Tide, MSGF+, MaxQuant). These were then analyzed using 18 different elution profile similarity metrics (Fig. 3.6, A). By aggregating the biochemical correlation scores from these experiments, we assessed the accuracy of various machine learning classifiers —individual (RF, GLM, SVM) and ensemble— in predicting protein-protein interactions (PPIs) through five-fold cross-validation, referencing CORUM mouse protein complexes as our benchmark. The ensemble classifier demonstrated superior sensitivity over individual models, identifying a greater number of CORUM protein pairs without compromising specificity. Setting a PPI score threshold between 0.79 - 0.94 for whole cell lysate and 0.75 - 0.84 for mitochondrial fractions based on the auROC of the ensemble model, and after refining the dataset by filtering out unlikely connections (i.e., between outer mitochondrial membrane and matrix as well as between intermembrane space and matrix), MACP identified a robust set of 5,076 - 8,728 PPIs from whole cell lysate and 2,040 - 4,866 PPIs from mitochondrial fractions, involving 668 - 1,356 and 455 - 818 proteins, respectively (Fig. 3.6, C). Particularly, GO biological function analysis (Fig. 3.6, D) on mitochondrial fraction from CHCHD2 mutant-exclusive intersections (highlighted in Fig. 3.6, C) revealed significant enrichment (FDR = 5.0e-02) for metabolic processes, including mitochondrial respiration and glycolysis, among others.

We observed that the interactions from whole cell and mitochondrial extracts were predominantly unique to each genotype and lysate, featuring proteins mostly found in non-mitochondrial compartments of whole cell lysate samples. In contrast, mitochondrial subcellular compartments showed PPIs mainly involving matrix and inner mitochondrial membrane proteins. Mapping these mouse PPIs to their human equivalents expanded the known human interactome significantly, introducing thousands of new physical associations and enhancing our understanding of the non-mitochondrial and mitochondrial protein networks as compared to previous studies. Notably, protein assemblies identified in mitochondrial extracts from CHCHD2 point mutants, but not in wild-type, as well as those identified in both whole cell and mitochondrial extracts of CHCHD2 wild-type but not in mutants, showed a marked enrichment (FDR ≤ 5e-02) for

associations with diseases such as Leigh syndrome, Parkinson's disease, amyotrophic lateral sclerosis and Alzheimer's disease (Fig. 3.6, E).

Following the establishment of the PPI network for each genotype, the ClusterONE algorithm was employed to divide these networks into numerous distinct protein complexes within the mouse brain's whole cell and mitochondrial lysates. The components of these predicted complexes for each genotype were then consolidated into a gene set. This gene set was compared against the co-elution profiles to pinpoint differential complexes that showed enrichment in the CHCHD2 mutants or in wild-type (Fig. 3.7, A and C). We focused on identifying common proteins across complexes in each cluster, and observed decreased interactions with glycolytic enzymes (cluster 1) and increased interactions with ribosomal (cluster 2) and proteasomal (cluster 3) proteins in whole-cell lysates of both CHCHD2 T61I and KO mice (Fig. 3.7, B). Notably, a significant increase in respiratory chain component interactions was found in the mitochondrial fraction in both T61I and KO mice (Fig. 3.7, D), suggesting the crucial role of CHCHD2 in maintaining respiratory chain assembly. In examining distinct patterns in T61I HOM compared to T61I HET and KO mice (cluster 2), we highlighted Dnajc11, which plays an important role in maintaining mitochondrial cristae structure and may be associated with neurodegenerative diseases. We also observed a potential association between mutant CHCHD2 and other genes related to neurodegenerative diseases, including DJ-1 (Park7) in cluster 3, which leads to an autosomal recessive form of PD when mutated. Others include Chrnb4 in cluster 3 and Cldn17 in cluster 4 both associated with frontotemporal dementia, Nefh in cluster 5 with amyotrophic lateral sclerosis, and Vdac2 in cluster 6 with Alzheimer's disease. These findings revealed robust disruptions in cellular metabolism due to CHCHD2 dysfunction and suggested potential linkages of mitochondrial malfunction to neurodegeneration.

Complex I of homozygous CHCHD2 T61I mice shows normal activity

As both spatial transcriptomics and proteomics data suggest a disruption in respiratory chain complex I components, we tested complex I activity by measuring NADH consumption in 45 minutes (Fig. 3.7, E). Isolated mitochondria from female T61I homozygous mice at 5 months old showed trending higher activity compared with WT mice, but this difference was concealed at 11 months. This suggests the respiratory deficits may not result from blockages of a single step, but an overall down-regulated performance of the whole pathway.

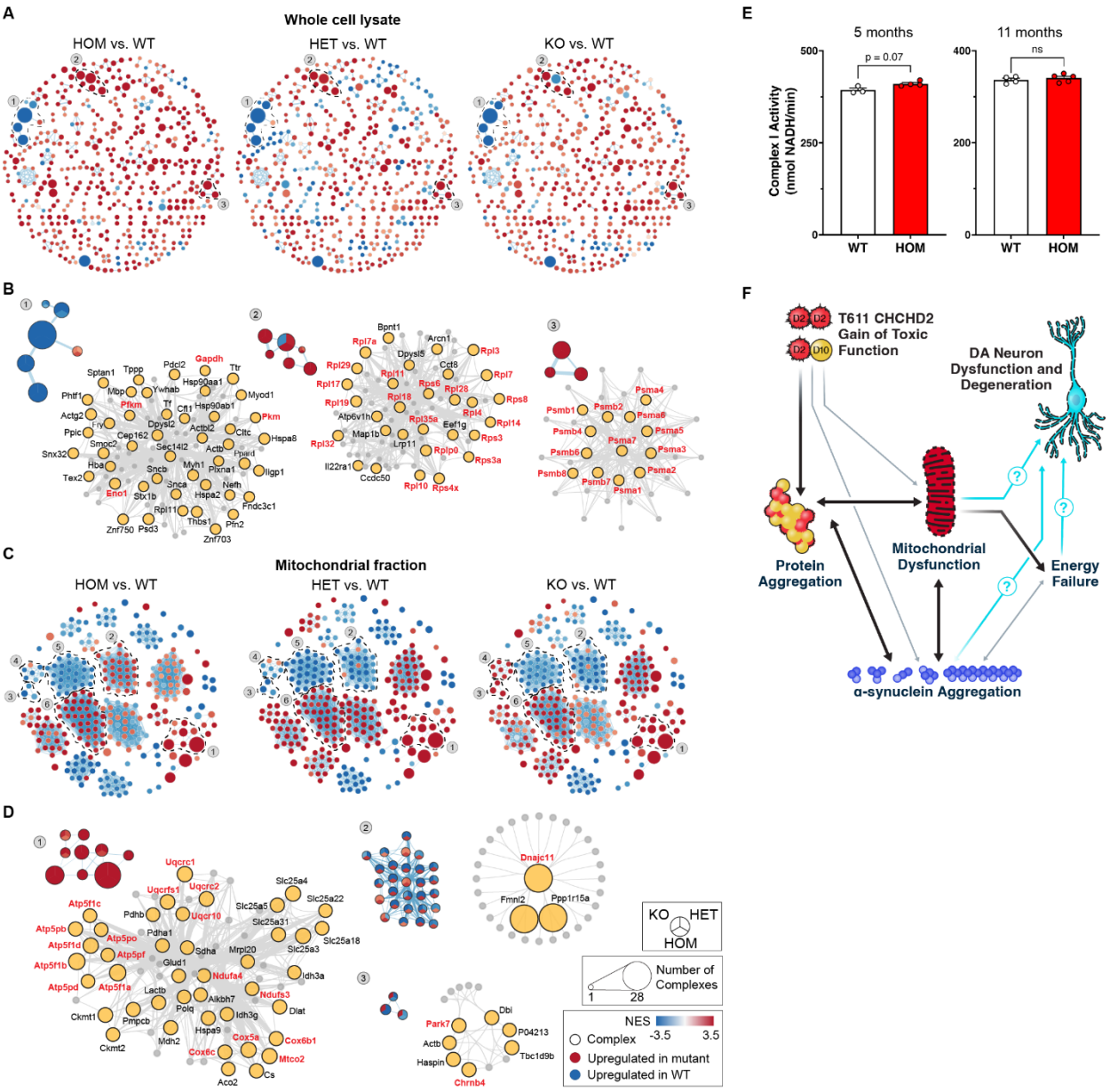

Figure 3.7: Differential analysis of predicted protein complexes in mouse brain WCL and mt lysates across different CHCHD2 genotypes. (A, C) Complexes in WCLs **(A)** and mt lysates **(C)** exhibit differential enrichment between CHCHD2 mutants and wild-type. **(B, D)** Displays of representative complexes (indicated by dotted circles with labels) showing increased interactions in WCLs **(B)** and mt lysates **(D)** of either CHCHD2 mutants or wild-type. The left panels in B and D show the proportion of interactions within each node, detected across various CHCHD2 genotypes or wild-type, with node size representing the number of interacting proteins predicted in each complex. The right panels in B and D provide detailed views of the physically associated proteins within each cluster.

3.4 Discussion

Our understanding about how mitochondrial dysfunction can cause PD is limited by the lack of robust phenotype in all of the reported mitochondria-based monogenic mouse

models of PD including Parkin KO, PINK1 KO and DJ-1 KO. This may not be surprising given that the mean lifespan of mice is 26-30 months, while Parkin, PINK1 and DJ-1 based PD usually begins after age 20 [67]. However, both Parkin and PINK1 PD have been reported in patients 5 or younger [68], suggesting that other fundamental differences between mice and humans may also contribute to the lack of robust phenotype.

In contrast, even though idiopathic PD typically doesn't start until the 60s, and most patients with T61I CHCHD2-associated PD to date have presented in their 50s [17], mutant T61I CHCHD2PM mice develop profound CHCHD2 aggregation by 16 months, resembling the aggregation reported in a CHCHD2 PD patient [46]. Interestingly, these CHCHD2 aggregates were reported to have decreased colocalization with a mitochondrial marker (ATP5A), and hence interpreted as accumulating in the cytosol, although the percentage localizing to the cytosol was not quantified. In contrast, in our mouse model, we observe near complete co-localization of CHCHD2 aggregates with mitochondria, perhaps suggesting that the aggregates first start in the mitochondria, but then a fraction escape to the cytosol. Alternatively, undefined technical or species differences may underlie this discrepancy. We hypothesize that the accumulation of CHCHD2 aggregates lead to disruption of mitochondrial morphology and mitochondrial protein-protein interactions, ultimately leading to mitochondrial dysfunction and a consequent metabolic shift that may be common features by which mitochondrial dysfunction causes different subtypes of both genetic and sporadic PD. Similarly, T61I CHCHD2 mice also show an accumulation of total and phosphorylated synuclein in midbrain DA neurons, mimicking changes that occur in both CHCHD2-PD [46] and idiopathic PD.

Two other similar CHCHD2 T61I knock-in mouse models have been reported recently, producing somewhat divergent results from ours. The T61I knock-in mouse reported by Shimizu *et al* demonstrated subtle impairments on rotarod in a very small size and decreased TH fluorescence signal in the SNc in the midbrain at 30 weeks, although did not directly assess dopamine neuron degeneration [53]. In contrast, the other T61I CHCHD2 mouse reported by Xu *et al* exhibited decreased body weight from 44 weeks, accompanied by a substantial decrease in mouse survival starting at 25 weeks, with 50% of heterozygotes dying at 43 weeks and 50% of homozygotes at 54 weeks, suggesting undetermined fundamental differences in these mice from our model. The weight loss and decreased mouse survival was accompanied by ≈30% decrease in the number of TH positive neurons in the SN but not VTA at 11 months, although stereology was not used and the sampling approach was not specified [69]. Notably, cell loss was not confirmed with another marker, raising the possibility that the decrease in TH neurons instead reflected downregulation of TH expression. Indeed, a substantial loss of TH neurons would be surprising given the subtle decrease in striatal TH optical density suggesting little if any loss of terminals, and would contrast with prior mitochondrial-based models targeting DA neurons where axonal loss precedes neuronal death [60]. Notably, a third study involving transgenic overexpression of human T61I CHCHD2 on a background of

wt CHCHD2 using a prion promoter [70] also reports a decrease in TH cell counts in the SN with no change in the VTA, assessed by immunofluorescence and a subtle decrease in striatal TH intensity, perhaps reflecting increased toxicity of higher levels of the mutant T61I CHCHD2, although the quantification methods are not provided, and it's also again unclear if this reflects downregulation of TH rather than true DA neuron loss.

We hypothesize that T61ICHCHD2 ultimately promotes neurodegeneration by disrupting mitochondrial respiration. Although this remains to be proven, several lines of evidence from our mouse model support this hypothesis. First, CHCHD2 is primarily a mitochondrial cristae protein, and we show that the T61ICHCHD2 mutation promotes both the accumulation of CHCHD2 in the mitochondria in DA neurons. Second, T61ICHCHD2 disrupts the morphology of mitochondria in DA neurons, suggesting that their function is likely compromised. Third, spatial genomics reveals subtle but widespread decreases in the expression of mitochondrial complex I and III genes in midbrain DA neurons. Fourth, untargeted metabolomics reveal an accumulation of both TCA and glycolytic metabolites consistent with respiratory chain dysfunction, with increased fractional labeling of glycolytic metabolites again consistent with a primary disruption of respiratory chain function. Fifth, whole mouse calorimetry studies reveal proportionally more reliance on carbohydrates relative to fat, also consistent with a respiratory chain deficit. Last, analysis of mitochondrial protein-protein interactions in brain lysates shows a broad disruption of interactions between respiratory chain proteins in the mouse brain.

We hypothesize the aggregation of CHCHD2 plays a causative role in the disruption of respiratory and other mitochondrial protein-protein interactions in CHCHD2 mutant mice. An alternate possibility is that a primary disruption of mitochondrial respiratory chain protein-protein interactions by T61ICHCHD2 leads to the disruption of respiratory chain functions, and the aggregation and accumulation of both T61ICHCHD2 and CHCHD10 are both secondary processes that do not influence against the degeneration process. Similarly, we hypothesize that the metabolic dysfunction leads directly to the DA neuron dysfunction and neurodegeneration in humans, but these steps also need to be established.

Our proteomic analyses also reveal other potentially important interactions. Among these, multiple changes in the PD protein DJ-1 were observed, raising the possibility of a mechanistic connection between DJ1 and PD. Interestingly, a fraction of both CHCHD2 and DJ-1 have been observed in both the nucleus and the mitochondria. DJ-1 was recently reported to directly bind to the CHCHD2 promoter and negatively regulate its expression [71]. In addition, Woo and colleagues also observed a decrease in DJ-1 solubility in the midbrain of CHCHD2 T61I by western blotting [70]. CHCHD2 and DJ-1 both can function in the integrated stress response and mitochondrial homeostasis, particularly in response to oxidative stress [72, 73]. It is possible that DJ-1 and CHCHD2 normally act together to maintain mitochondrial quality control in a mutually dependent pathway, which is disrupted by the T61I mutation.

Mitochondrial dysfunction and increased α-synuclein both cause rare monogenic forms of PD, and both also occur in idiopathic PD. In addition to producing prominent changes in mitochondria and energy metabolism, our T61I CHCHD2 mouse model also produces increased levels of both total and phosphorylated-129 synuclein, consistent with findings in the other two CHCHD2 KI mouse models [53, 69]. Combined with the prominent α-synuclein aggregation observed in a patient with T61I CHCHD2, this provides compelling evidence that a PD-causing mitochondrial mutation can cause synuclein aggregation. This is important in strengthening a causative link between mitochondrial dysfunction and typical later onset PD, especially because the lack of Lewy bodies in most patients with Parkin-based PD has led many investigators to conclude that autosomal recessive forms of PD are distinct from sporadic PD.

Our model system also provides opportunity to study selective vulnerability. We previously showed that midbrain DA neurons have elevated levels of CHCHD2 versus other neuron types in vivo and in vitro, relative to several other neuron types [50], suggesting a potential mechanism for selective vulnerability. Here, we show that SNc DA neurons preferentially accumulate CHCHD2 aggregates versus VTA DA neurons, although no difference in the level of CHCHD2 was observed between SNc and VTA DA neurons. Interestingly, we also show that gene expression of CHCHD2 is elevated specifically in vulnerable SN DA neurons in the ventral tier of the SNc, relative to levels in the dorsal tier. In contrast, this differential was not detected in either pre-symptomatic PD, incidental Lewy bodies where there is no detectable loss of DA neurons or in early PD, suggesting that it is unlikely to reflect the death of DA neurons with higher CHCHD2. Instead, it may reflect a downregulation of CHCHD2 levels in DA neurons as the disease progresses, which could indicate that it normally protects or is toxic. However, we also observed that CHCHD2, together with mitochondria, are engulfed in early Lewy bodies, and presumably degraded as they are no longer evident in more mature Lewy bodies. How this process of mitochondrial degradation influences CHCHD2-specific and overall mitochondrial function is unknown. The relationship of CHCHD2 to its binding partner CHCHD10 is also of particular interest. Mutation of CHCHD10 can produce ALS/FTD or myopathy, and our proteomics studies also revealed hits associated with AD, ALS and FTD, perhaps suggesting a shared pathophysiologic mechanism between PD and these disorders.

3.5 Methods

Animals

CHCHD2 p.T61I mice were generated using EUCOMM's conditional-ready embryonic stem (ES) cells. Two single-guide RNAs (5'-GCCTCTGAACCTGGCCCATTTGG-3' and 5'-TCCTGAACCCTATTTAGTTTTGG-3') respectively targeting immediate upstream of exon 2 and immediate downstream of exon 3 were used to remove entire exon 2 and 3, and the point mutation was delivered by a donor vector via homologous recombination. ES cells were injected to blastocytes and transferred to recipient females. Mice were maintained on a C57Bl/6 background (The Jackson Laboratory, 000664)

Mice were group-housed in a colony maintained with a standard 12 hours light/dark cycle and given food and water ad libitum. All animal experimental procedures were conducted according to the Guide for the Care and Use of Laboratory Animals, as adopted by the National Institutes of Health, and with approval of the University of California, San Francisco, Institutional Animal Care and Use Committee. Animal care and use in this research are covered under the UCSF ‘‘Assurance of Compliance with PHS Policy on Humane Care and Use of Laboratory Animals by Awardee Institutions’’ number A3400-01.

qPCR Genotyping

CHCHD2 p.T61I genotyping was done by qPCR followed by endpoint allelic discrimination. A product size of 322 bp was amplified using the forward primer (5’-TGAAGATGGCCCAGATCTG-3’) and the reverse primer (5’-CTGAAGCCCCCAGTGAT-3’). Allelic discrimination was done automatically by Applied Biosystem’s SDS 2.4 software using the WT probe (5’ JOE-TTAGATGGCTACCACCGCG-3’ Iowa Black) and the MT probe (5’ 6-FAM-TTAGATGGCGATCACCGCG-3’ Iowa Black).

Behavioral Testing

General locomotor activity was measured by the open field test using standard procedure [74]. Mice were placed in the center of a clear acrylic chamber and allowed to explore freely for 15 min. Horizontal and vertical movements were detected using photobeams lining the perimeter of the chamber, and ambulatory and fine movements were separately recorded. Fine movements were defined as breaking the same 2 photobeams repeatedly, while ambulatory movements were defined as breaking 3 or more.

Muscle strength was measured by the inverted grid hang test. Each mouse was first placed with all four paws firmly grasping on a wire grid, which was then inverted so the mouse is hanging over a cage filled with bedding. The latency to fall was recorded, and the maximum latency is 180 s. Mice were tested for 3 trials with an interval of 1 h between each trial.

Motor coordination was measured using a rotarod (Med Associates Inc) as described previously [75]. Fall from the rotating rod was automatically detected by infrared beams, and the maximum latency was 5 min. 5 mice of the same gender were tested simultaneously in each trial. On the first day, mice were trained to run on a rotating rod at 16 rpm (training phase). Mice were tested on 3 trials with an intertrial interval between 15 and 20 min. On the second and third day of testing, mice were placed on the rod rotating at an accelerating speed from 4 to 40 rpm. The rotation speed increased by 7.2 rpm every 60 s. Mice were tested on 2 sessions of 3 trials with an intertrial interval between 15 and 20 min, and a 2 h interval between the AM and PM sessions.

Anxiety-related locomotion was measured using an elevated plus maze (Kinder Scientific) consisting 2 open arms and 2 closed arms elevated 63 cm above the floor. Mice were given at least 1 h to acclimate to the testing room before mice freely exploring the maze

for 10 min. The time, distance, and entries into the open and closed arms were calculated based on infrared photobeam breaks.

Electrophysiology

Mice were deeply anesthetized with isoflurane and then decapitated. Horizontal brain slices (150 μm) were prepared using a vibratome (Campden Instruments 7000smz-2). Slices were prepared in ice cold Ringer solution (in mM: 119 NaCl, 2.5 KCl, 1.3 $MgSO_4$, 1.0 NaH_2PO_4, 2.5 $CaCl_2$, 26.2 $NaHCO_3$, and 11 glucose saturated with 95% O_2-5% CO_2) and allowed to recover at 33°C for at least 1 hr. Slices were visualized under an Axio Examiner A1 equipped with Dodt and IR optics, using a Zeiss Axiocam 506 mono and Neurolucida (MBF Biosciences) software. Whole cell recordings were made at 33°C using 4-5 MΩ pipettes filled with (in mM): 123 K-gluconate, 10 HEPES, 0.2 EGTA, 8 NaCl, 2 MgATP, 0.3 Na_3GTP, and 0.1% biocytin (pH 7.2, osmolarity adjusted to 275 mOsm/L). Recordings were made using Sutter IPA and SutterPatch software (Sutter Instruments), filtered at 5 kHz and collected at 10 kHz. For all current clamp experiments I = 0. Liquid junction potentials were not corrected during recordings. The reported firing rates are averages of the spontaneous firing rate over the first 2 minutes of whole cell access. I_h magnitude was measured as the difference between the initial capacitative response to a voltage step from -60 to -120 mV and the final current during the same 800 ms step. Coefficient of Variation was calculated over 100 interspike intervals to evaluate the regularity of firing. Input and series resistances were monitored with hyperpolarizing pulses (0.1 Hz) throughout each experiment. All neurons were filled with biocytin during recording, slices were fixed (4% formaldehyde for 2 hr), and then immunocytochemically processed for TH (I can add methods if necessary). Agonists, antagonists, salts, ATP, and GTP were obtained from MilliporeSigma. Quinpirole effects were statistically evaluated in each neuron by binning data into 30 s data points and comparing the last 8 baseline data points to the last 8 data points during drug application. All but 2 neurons recorded in current clamp were quiescent during quinpirole testing; the two firing neurons were excluded from the figure. Both were from WT mice and in both cases quinpirole decreased the spontaneous firing rate.

Striatal Catecholamines Analysis

Mice were deeply anesthetized with avertin and perfused with cold phosphate-buffered saline (PBS). Brains were rapidly removed, flash-frozen in a dry ice isopentane bath, and stored at -80°C before further processing. The striatal region was dissected from half of a brain cut in the sagittal plane, and then trimmed precisely with a cryostat (CryoStar NX50). After the dorsal striatum was fully exposed, punches were made with a pipette tip cut into 1 mm in diameter, and then flash-frozen and stored at -80°C. Catecholamine levels were measured by the Vanderbilt Neurochemistry Core by HPLC coupled to an electrochemical detector [76].

Immunohistochemistry and Immunofluorescence Staining

Mice were deeply anesthetized with avertin and perfused with cold PBS followed by 4% paraformaldehyde (PFA). Brains were dissected out, postfixed in PFA overnight and

stored in 30% sucrose cryoprotectant at 4°C. Brains were cut in the coronal plane into 40 µm-thick sections with a sliding microtome (Leica SM2000R).

For immunofluorescence, brain sections were washed with PBS and transferred in blocking solution containing 0.2% Triton X-100 with 4% BSA for 1 h. Sections were then incubated overnight at 4°C with the appropriate primary antibody. Primary antibodies used: mouse and rabbit anti-CHCHD2 (Proteintech, 19424-1-AP and 66302-1-Ig, 1:1000); rabbit anti-CHCHD10 (Proteintech, 25671-1-AP, 1:1000); mouse anti-PDH (Abcam, 110333, 1:1000); mouse, rabbit and sheep anti-Tyrosine hydroxylase (Millipore, MAB152, MAB318 and MAB1542, 1:1000); mouse anti-α-synuclein (BD Transduction Laboratories, 610787, 1:500); rabbit anti-phosphorylated α-synuclein (phosphor S129; Abcam ab51253, 1:300). Sections were then washed with PBS with 0.2% Triton X-100 and incubated for 2 h at room temperature with the corresponding secondary antibodies: Alexa Fluor 488, 594 or 647 anti-mouse, anti-rabbit or anti-sheep IgG (Invitrogen, A32723, A11012 and A21448, 1:500).

For peroxidase staining, sections were quenched with 3% hydrogen peroxide and 10% methanol in PBS. Sections were then blocked in 10% bovine calf serum with 0.4% Triton X-100. Sections were incubated overnight with rabbit anti-TH (1:1000), mouse anti-α-synuclein (1:500) or rabbit anti-phosphorylated α-synuclein (1:300), followed by biotinylated goat anti-rabbit or anti-mouse IgG (Vector Laboratories PK-6101 and PK-6102, 1:300) for 2 h, and then streptavidin-conjugated horseradish peroxidase (HRP) (1:300) for another 2 h. Immunostaining was visualized by developing in 3,3'-diaminobenzidine (DAB, Sigma D12384) and 0.003% hydrogen peroxide solution for 3-5 min.

Brain sections were imaged with a laser scanning confocal microscope (Zeiss LSM880 with Airyscan) or a slide scanner (Leica Aperio Versa). Quantification of fluorescence and area was performed blinded to genotype with ImageJ or CellProfiler.

Stereology

Total numbers of TH-positive neurons were quantified blinded to genotype. Region selection of SN and VTA was done under 5× magnification following the definition by Fu and colleagues [77]. Sections were imaged at 63× using a Zeiss Imager microscope (Carl Zeiss Axio Imager A1) equipped with an XYZ computer-controlled motorized stage and an EOS rebel T5i Digital Camera (Canon), and cell counts were performed using MBF Bioscience's Stereo Investigator. Counting frame size was 60 × 60 µm and systematic random sampling (SRS) grid was 130 × 130 µm, with a section interval of 6.

Quantifications by Cellprofiler

Acquired images were first segmented to resolve individual cells, by manually drawing each cell using the Fiji rectangle selection tools. Individual cell image files were then saved in the input folder and batch processed in CellProfiler [v4.2.5].

α-Synuclein Extraction and Western Blot Analysis

Protein was extracted from flash-frozen brains as described by Stojkovska and Mazzuli [78]. Briefly, homogenized tissues were extracted by agitating in 1% Triton X-100-containing lysis buffer on ice-water slurry for 30 min. 3 freeze/thaw cycles were adopted to facilitate homogenization. Lysate was ultracentrifuged for 30 min at 4°C, and the supernatant was collected as “Triton-soluble fraction”. The pellet was further extracted with SDS lysis buffer, sonicated, and centrifuged for 30 min at 21°C. The supernatant was collected as “SDS-soluble fraction”. Protein concentration was measured using Pierce BCA assay (ThermoFisher, 23227).

15 µg of total protein from the Triton fraction and 25 µg from the SDS fraction were loaded on to polyacrylamide gels (Bio-Rad, 4569033) and electrophoresis was carried out using standard SDS-PAGE procedures. Protein was then transferred from the gel on to a PVDF membrane (Invitrogen, IB24001) using the iBlot™ 2 rapid transfer system (Invitrogen, IB21001). The leftover gel after transfer was stained by Coomassie brilliant blue and served as a loading control later. The PVDF membranes were fixed in 0.4% PFA for 30 min at 20°C before blocked for 1 h in a 1:1 mixture of 1X phosphate-buffered saline (PBS) and Li-Cor’s Odyssey PBS blocking buffer (P/N 927-40000). Membrane was incubated overnight with primary antibodies: mouse anti-α-synuclein (BD Transduction Laboratories, 610787, 1:1000), rabbit anti-phosphorylated α-synuclein (phosphor S129; Abcam ab51253, 1:500) and rabbit-anti-Actb (Abcam, ab115777, 1:2500). After incubation in secondary antibodies, Alexa Fluor 647 anti-mouse (Invitrogen, A31571, 1:10000) and Alexa Fluor 488 anti-rabbit (Invitrogen, A11008, 1:10000), membrane was imaged by Bio-Rad’s ChemiDoc Imaging System. Quantification was done by ImageJ.

Subcellular Fractionation

Cells were harvested with a scraper, washed in PBS, homogenized using a glass pestle in isolation medium (250 mM sucrose, 1 mM EDTA, and 10 mM Tris–MOPS, pH 7.4), and then centrifuged at 600 g for 10 minutes at 4°C to pellet nuclei and undisrupted cells. The resulting supernatant was centrifuged at 9000 g for 10 minutes at 4°C, separating the supernatant (containing cytosol) from the pellet. The pellet was resuspended in isolation medium and subjected to 3 additional rounds of centrifugation at 9000 g for 10 minutes at 4°C and the final pellet, containing mitochondria, was retained.

For the isolation of soluble (S) and insoluble (I) fractions from the mitochondrial and cytosolic samples, both fractions were incubated on ice with 1% Triton X-100 for 30 minutes and then centrifuged at 20000 g for 10 minutes at 4°C. After removal of the supernatant (S fraction), the pellet was incubated in SDS buffer for 30 minutes and centrifuged for 10 minutes at 20000 g yielding the insoluble fraction (I fraction).

Immunoprecipitation (IP) and Western Blot Analysis

The whole cell extract from murine brain tissue was incubated with RIPA buffer [79], and a protease inhibitor cocktail (PIC). Subsequently, 3 µl of the designated antibody was incorporated. After stirring for 1 hour at 4°C, 100 µl of µMACS Protein A magnetic beads (Miltenyi Biotec) was added, followed by further agitation for 4 hours at 4°C. The mixture

was then processed through μMACS columns (Miltenyi Biotec), undergoing two washes with 1 ml of RIPA buffer (0.1% concentration) containing PIC, and a final wash with 1 ml of RIPA buffer devoid of detergents. Proteins were eluted in 2x Laemmli buffer, and analyzed via western blotting.

Electron Microscopy

Mice were deeply anesthetized with avertin and perfused with cold PBS followed by 4% paraformaldehyde (PFA) and 0.5% glutaraldehyde. Brains were removed and postfixed in the same fixative solution overnight and stored at 4°C. Samples were sectioned into 100 μm thickness with a vibratome. Before immunogold labeling, brain sections were washed with 0.1M phosphate buffer for 3 times, reduced by 1% sodium borohydride for 30 minutes, and incubated in 25% sucrose cryoprotectant for 30 minutes. After 4 more washes, brain sections were flash-frozen with isopentane and freeze-thawed 3 cycles to increase permeability. Sections were blocked in 0.1M phosphate buffer with 0.3% BSAc and 0.05% sodium azide, incubated overnight at 4°C with the rabbit anti-TH primary antibody (Millipore AB152) and then with 0.8 nm gold particle goat anti-rabbit antibody (EMS 25100) overnight. Sections were post-fixed for 10-minutes in 1.5% glutaraldehyde solution at room temperature. After 2 washes with 0.1M phosphate buffer and 5 washes with ddH_2O, silver enhancement was done for 7 minutes at room temperature (Nanoprobes, 2012).

Post-Mortem Human Substantia Nigra

Tissue samples from pathologically confirmed incidental Lewy body disease (ILBD, n=5), early PD (n=9), and late PD (n=8), and controls without the neurological or neuropathological disease (n=10) were obtained from the New South Wales (NSW) Brain Banks (Supplementary Table 1). The study was approved by the University of Sydney Human Research Ethics Committee (2021/845). All cases with PD were levodopa-responsive and fulfilled the UK Brain Bank Clinical Criteria for the clinical diagnosis [80] with no other neurodegenerative conditions. Controls had no Lewy pathology, while ILBD and PD cases were staged using the regional location of the Lewy pathology [81, 82]. Formalin-fixed paraffin-embedded (FFPE) sections from controls, ILBD (Braak stage I-II), early PD cases (Braak stage IV), and late PD cases (Braak stage VI) were used to examine the expression of CHCHD2, CHCHD10, and the locational association of their proteins with the intracellular αSyn aggregations in the DA neurons.

Human Tissue Preparation and Immunofluorescence Staining

FFPE blocks of human midbrains containing substantia nigra (SN) were cut on a rotary microtome (HistoCore MULTICUT R Rotary, Leica Biosystems) at 6 μm. Sections were mounted on Fisher Scientific (12-550-15) for GeoMx Human Whole Transcriptome Atlas (WTA, nanostring) according to the manufacturer's instruction or on Series 2 adhesive microscope slides (Trajan Scientific Medical, AU) for immunofluorescence. Before staining, sections were de-waxed and rehydrated with HistoChoice® Clearing Agent

(Sigma, H2779) and gradient concentrations of ethanol. Each antibody was tested with immunohistochemistry to decide the optional solution for heat-induced antigen retrieval. For this immunofluorescence approach, Tris-EDTA (pH 9.0) and formic acid (70% for 20 min) were applied in a programmable antigen retrieval cooker (Aptum Bio Retriever 2100, Aptum Biologics Ltd, UK). Sections were blocked with Human BD Fc Block (BD Pharmingen , 564219, 1:50) for 30 mins at room temperature, then TrueBlack® Background Suppressor (Biotium, 23012A) for 1 hr at RT. Primary antibodies (either CHCHD2 or CHCHD10 with αSyn and mitochondrial markers) were diluted in blocking buffer (2% donkey serum, 1% BSA, 0.1% fish gelatine, 0.3% Triton X-100, 0.1% Tween-20, and 0.02% NaN_3 in PBS) for section incubation at RT for one overnight, followed by the corresponding Alexa Fluor secondary antibodies with Hoechst nucleus counterstaining (bisBenzimide H 33342 trihydrochloride, Sigma, B2261, 1µg/ml) at RT for 2 h. Sections were further incubated in Alexa flour 790 conjugated TH antibody in blocking buffer at RT for 2 h before being treated with TrueBlack® Lipofuscin Autofluorescence Quencher (Biotium, 23007). Slides were mounted with EverBrite™ mounting medium (Biotium, 23001) and sealed with Biotium's CoverGrip™ Coverslip Sealant (23005). Negative controls were performed for each staining batch, omitting primary or secondary antibodies.

Metabolomics

Mice were fasted overnight prior to anesthetizing with isoflurane. The mice then received a 200 µl bolus of [13-C]glucose solution (Cambridge Isotope Labs, CLM-1396-1) via intraperitoneal injection, followed by tail vein infusion at a rate of 150 µl/h. After infusion, mice were decapitated and the brains rapidly removed and flash-frozen in a dry-iced isopentane bath. Metabolites were extracted from homogenized brains by incubation in 80% methanol at -80°C for 20 min, followed by centrifugation at 14,000 g for 15 min. Metabolite supernatants were dried in a Labconco CentriVap prior to storage at -80C. Samples were quantified at the UCLA Metabolomics Core.

Spatial transcriptomics

Mouse

Spatial transcriptomics were acquired with Visium spatial gene expression kits (10X Genomics). Sample preparation, sample imaging, and library generation were completed in accordance with 10X Spatial Gene Expression protocols. Briefly, fresh brain tissue was flash frozen in a dry ice isopentane bath. The brain tissue was then embedded in Optimal Cutting Temperature (OCT) compound (Tissue-Tek 62550-12). 10 µm-thin section from the midbrain was made with a cryostat (CryoStar NX50) and then mounted onto a 10X spatial gene expression slide. Sections were stained with TH, NeuN, and Hoechst 33342 before imaging on a Leica Aperio Versa slide scanner. The cDNA libraries were generated at the Gladstone Genomics Core and sequenced at the UCSF Center for Advanced Technology on an Illumina NovaSeq 600 on an SP flow cell. Alignment of the sequencing data with spatial data from the Visium slide was completed with the 10X Space Ranger software. Two anatomical regions of interest, SN and VTA, and a control

region, thalamus, were identified. RNA capture areas corresponding to each anatomical region were selected for analysis based on their spatial proximity to the anatomical regions and on the expression of known genetic markers. SN and VTA genetic markers included TH, DAT, and VMAT2; thalamus markers included Prkcd, Ptpn3, and Synpo2. Demarcation of SN and VTA was done according to Fu *et al* [77]. SN and VTA capture areas also had to contain at least one complete DA neuron soma. Gene rankings for hit analysis were established using the fold change score (FCS) and signal-to-noise score (SNS). Equations for these scores are given as:

$$SNS = \frac{\mu_{HOM} - \mu_{WT}}{\sigma_{HOM} + \sigma_{WT}} \times (-Log_{10}P)$$

$$FCS = Log_2\left(\frac{\mu_{HOM}}{\mu_{WT}}\right) \times (-Log_{10}P)$$

where μ is the average gene expression, σ is the standard deviation, and P is the p-value derived from a t-test. Genes with a p-value < 0.05 that also appeared in the top 20% for both scoring metrics were highlighted as differentially expressed genes of interest.

Human

FFPE tissue slices from the substantia nigra pars compacta (SNc) and Locus Coeruleus (LC) from a Control subject and PD patient were each (matched SNc & LC per capture window) analysed using 10X Visium Cytassist and sequenced on the Illumina NovaSeq 6000. Raw fastq read files were demultiplexed using 10X Genomics' spaceranger mkfastq pipeline and a feature-barcode matrices were generated using "spaceranger count". Spatial transcriptomic analysis was performed using Giotto. Each capture window contained 14329 spots (55 μm). Genes were considered that contained > 1 count within at least 50 spots. Spots were retained that contained at least 500 gene expression features. Raw counts were normalized for total library size, scaled (scaling factor =6000), log-transformed, and then scaled (z-score) for genes and cells.

Co-Fractionation Coupled with Mass Spectrometry (CF-MS)

Whole cell extracts (WCE) and mitochondrial extracts (mt) totaling 500 μg each were obtained from the brains of CHCHD2 WT, CHCHD2 T61 heterozygous and homozygous, and CHCHD2 KO mice. These samples were cross-linked using dithiobis (succinimidyl propionate) (DSP) and then subjected to size exclusion chromatography (SEC) employing an Agilent 1100 HPLC system equipped with a 300 × 7.8 mm BioSep-4000 Column (Phenomenex), in accordance with a protocol recently described in the literature [66]. This procedure yielded 96 fractions for each extract per genotype. These fractions were subsequently digested with trypsin and analyzed via an Easy-nanoflow liquid chromatography 1200 (Easy nLC; Proxeon) system connected to an Orbitrap Exploris mass spectrometer (Thermo Fisher Scientific). The method for processing the digested samples, the chromatographic separation, and the settings for the comprehensive scanning of mass spectrometry spectra are detailed as previously [66].

Immunoprecipitation Coupled with Mass Spectrometry (IP-MS)

The brains of CHCHD2 WT, CHCHD2 T61 heterozygous and homozygous, and CHCHD2 KO mice were lysed in RIPA buffer (containing 150 mM NaCl, 50 mM Tris-HCl pH 7.5, 0.1% SDS, 1% sodium deoxycholate, 1% NP-40, and 1 mM EDTA), and enriched with a 1X protease inhibitor cocktail (PIC). Lysates were centrifuged at 13,000 x g for 10 minutes at 4°C, and the resulting supernatant was subsequently incubated with a CHCHD2-specific antibody (Proteintech, 19424-1-AP) for 2 h at 4°C. This was followed by overnight incubation with μMACS Protein A magnetic microbeads (Miltenyi Biotec) at 4°C. The microbeads were washed and eluted in μMACS columns pre-equilibrated with RIPA and PIC. The beads underwent two washes in RIPA buffer with 0.1% NP-40 detergent and PIC, and another in a detergent-free buffer as we previously described [83]. Protein digestion was performed directly on the column using either sequencing-grade trypsin gold (Promega) or mass spectrometry grade proteases chymotrypsin (Thermo Fisher Scientific) overnight at room temperature, with digestion halted by adding 0.1% (v/v) formic acid. The peptide mix was then purified using ZipTip C18 tips (Millipore), air-dried, and resuspended in 0.1% formic acid for mass spectrometry analysis, as previously described [83].

Liquid Chromatography Tandem Mass Spectrometry (LC-MS/MS)

NanoLC connected to an Orbitrap Exploris mass spectrometer (Thermo Fisher Scientific) was used for the analysis of all samples. The peptide separation was carried out using a Proxeon EASY nLC 1200 System (Thermo Fisher Scientific) fitted with a custom-made C18 column (15 cm x 150 μm ID) packed with HxSil C18 3 μm Resin 100 Å (Hamilton). A gradient of water/acetonitrile/0.1% formic acid was employed for chromatography. The samples were injected onto the column and run for 95 minutes at a flow rate of 0.60 μl/min. The peptide separation began with 1% acetonitrile, increasing to 3% in the first 2 minutes, followed by a linear gradient from 3% to 23% acetonitrile over 74 minutes, then a steep increase from 24% to 80% acetonitrile over 10 minutes, and finally a 10-minute wash at 80% acetonitrile. The eluted peptides were ionized using positive nanoelectrospray ionization (NSI) and directly introduced into the mass spectrometer with an ion source temperature set at 250°C and an ion spray voltage of 2.1 kV. Full-scan MS spectra (m/z 350–2000) were captured in Orbitrap Exploris at a resolution of 240,000 (m/z 400). The automatic gain control was set to 1e6 for full FTMS scans and 5e4 for MS/MS scans. Ions with intensities above 1500 counts underwent fragmentation in the linear ion trap. The top 15 most intense ions with charge states of ≥2 was sequentially isolated and fragmented using normalized collision energy of 30%, activation Q of 0.250, and an activation time of 10 ms. Ions selected for MS/MS were excluded from further selection for 30 seconds. The Orbitrap Exploris mass spectrometer was operated using Thermo XCalibur software.

LC-MS/MS Analysis

Raw spectral files from IP-MS or size exclusion chromatography-high performance liquid chromatography (SEC-HPLC) fractionation-MS experiments were converted into mzXML format using ReAdW software and then searched against the canonical mouse protein

sequences from the UniProt database. To enhance the sensitivity and accuracy of peptide identification, the mzXML files underwent searches against these mouse protein sequences utilizing peptide-spectrum matches from three distinct search engines: Tide (from the Crux suite version 4.1), MS-GF+ (version 2017.01.13), and MaxQuant (version 1.6.7.0) for CF-MS, while Tide and MS-GF+ for IP-MS experiments. These searches aimed to maintain a false discovery rate (FDR) below 0.1% for Tide and MS-GF+ or 1% for MaxQuant, both for peptide and protein identifications. The results from Tide and MS-GF+ were further refined using Percolator1. MaxQuant searches were conducted with a 4.5 ppm tolerance for precursor mass in the main search, a 20ppm tolerance for fragment ion or peptide mass in the first search, and allowance for up to two missed cleavages. Tide searches were set with a 10ppm tolerance for fragment ion mass and one missed cleavage, while MS-GF+ searches allowed a 20ppm tolerance for precursor mass with a percolator peptide Q value threshold set at 0.1. Across all searches, carbamidomethylation of cysteine was treated as a fixed modification, with methionine oxidation and protein N-terminal acetylation permitted as variable modifications.

Computational Scoring to Predict Protein-Protein Interactions (PPIs) from CF-MS Datasets

For predicting endogenous protein interactions from CF-MS experiments using whole cell lysate (WCL) and mitochondrial (mt) extracts, the MACP algorithm [83] was employed. The preprocessing steps undertaken included: (1) Averaging Log2-transformed MaxQuant MS1 ion intensities together with spectral counts from Tide and MS-GF+; (2) Excluding proteins identified in only one fraction; (3) Imputing zeros for missing proteins not detected by MS, due to either low abundance or absence in the mouse tissues; and (4) Adjusting for fraction bias and discrepancies in sample injection through row- and column-wise normalization, accounting for the variation in peptide abundance across fractions. Subsequently, the protein elution profile matrix from each search engine for a given sample was independently analyzed for PPI scoring. This analysis employed 17 distinct correlation metrics to calculate pairwise protein profile similarities, with details of each profile feature have been described in our recent study [66]. The results from each search engine were then integrated using a random forest (RF) classifier, which had been trained using PPIs from curated mouse complexes in the CORUM4 and IntAct5 databases. Scores for each protein pair across different search engines were merged to compute an average RF score. The model's prediction performance was evaluated through 10-fold cross-validation against an independent set of PPIs, establishing an RF cut-off score of > 0.5. Protein pairs scoring below this 0.5 threshold were excluded from consideration.

Multimeric Protein Complex Predictions from PPI Network

High-confidence PPIs identified through CF-MS experiments across different genotypes were analyzed using the ClusterONE (Clustering with Overlapping Neighborhood Expansion) algorithm to delineate complex memberships. The optimization of ClusterONE involved various combinations of parameter adjustments (density, d; overlap,

o) alongside a suite of evaluation metrics (accuracy, maximum matching ratio, overlap) as we previously described [66]. In brief, the predicted complexes were compared against known CORUM and IntAct mouse protein complexes using a range of density (0.2-0.45) and overlap (0.5-0.8) settings across the evaluation metrics. The parameter settings that yielded the highest composite score—representing the sum of accuracy, overlap, and maximum matching ratio—were deemed most effective for identifying high-quality protein complexes. The interactions among proteins across the four genotypes, along with the predicted macromolecular complexes from the PPI networks derived from CF-MS datasets, were visualized using Cytoscape7 software (ver. 3.9.1).

Differential protein complex analyses

To assess the complex rewiring among the four genotypes, we utilized coelution profiles of the predicted protein complex subunits. Gene set enrichment analysis (GSEA) was performed, treating each complex identified within the four genotypes as a gene set. We then compared the coelution profiles of each subunit within these gene sets across the genotypes.

Complex I activity assay

A detailed protocol for characterizing isolated mitochondria can be found at https://doi.org/10.17504/protocols.io.e6nvwdz87lmk/v1. A piece of mouse cerebrum containing the midbrain was flash-frozen and pulverized for mitochondrial isolation. The mass of isolated mitochondria was measured using a Pierce BCA protein assay kit. To measure enzyme activity of complex I, 10 µg of crude mitochondria preps was dispensed into a 96-well plate containing 50 mM pH 7.4 potassium phosphate buffer, 2 mM potassium cyanide, 2.5 mg/mL bovine serum albumin, 5 mM $MgCl_2$, 2 µM Antimycin A, 100 µM decylubiquinone, and 300 µM K_2NADH, with or without 1 µM rotenone. Immediately after combining mitochondria with the above reagents, 340 nm absorbance was measured for 45 min on a Spectramax M4 plate reader.

3.6 Supplementary Figures

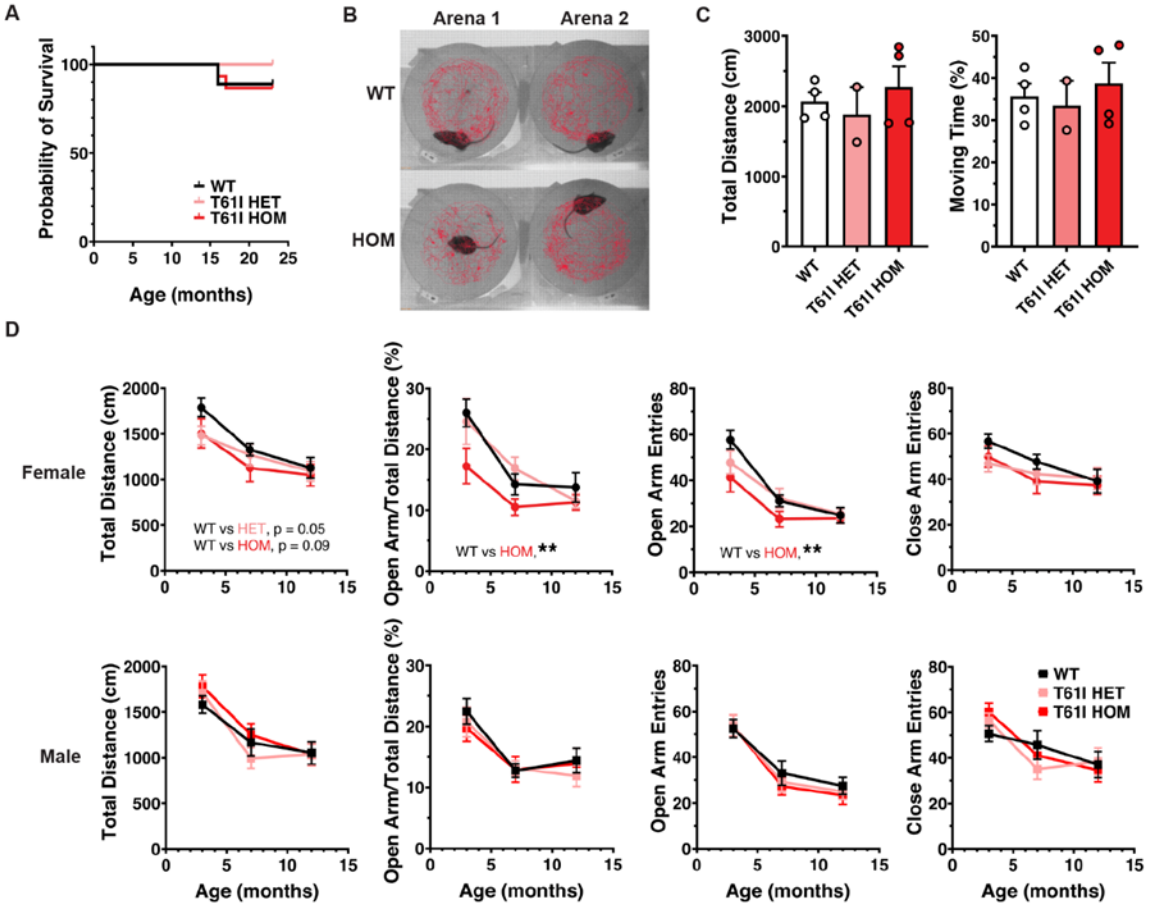

SFigure 3.1: CHCHD2 T61I mice exhibit normal survival and general locomotor activity through 23 months but increased anxiety. (A) Survival probability was not different in a second cohort of T61I mice through 23 months of age (Kaplan-Meier survival curve, n = 9 WT, 8 HET and 15 HOM). **(B)** Representative track visualization of homozygous T61I male mice at 23 months (4 WT, 2 HET and 4 HOM) in the open field test. **(C)** Quantifications of total distance and percentage moving time in the open field test using Ethovision. **(D)** Total movement, open arm/total distance, open arm entries and closed arm entries of T61I mice in the elevated plus maze. Female HOM showed trending lower total distance (WT vs HOM $P = 0.089$) and significantly decreased open arm/total distance percentage (WT vs HOM $P < 0.008$, **) and open arm entries (WT vs HOM $P < 0.004$, **) in the elevated plus maze. N = 16 WT, 16 HET and 13 HOM (female), or 14 WT, 18 HET and 17 HOM (male). In all behavioral studies (B-D), data represent mean ± SEM. **$P < 0.01$ by linear mixed effects analysis.

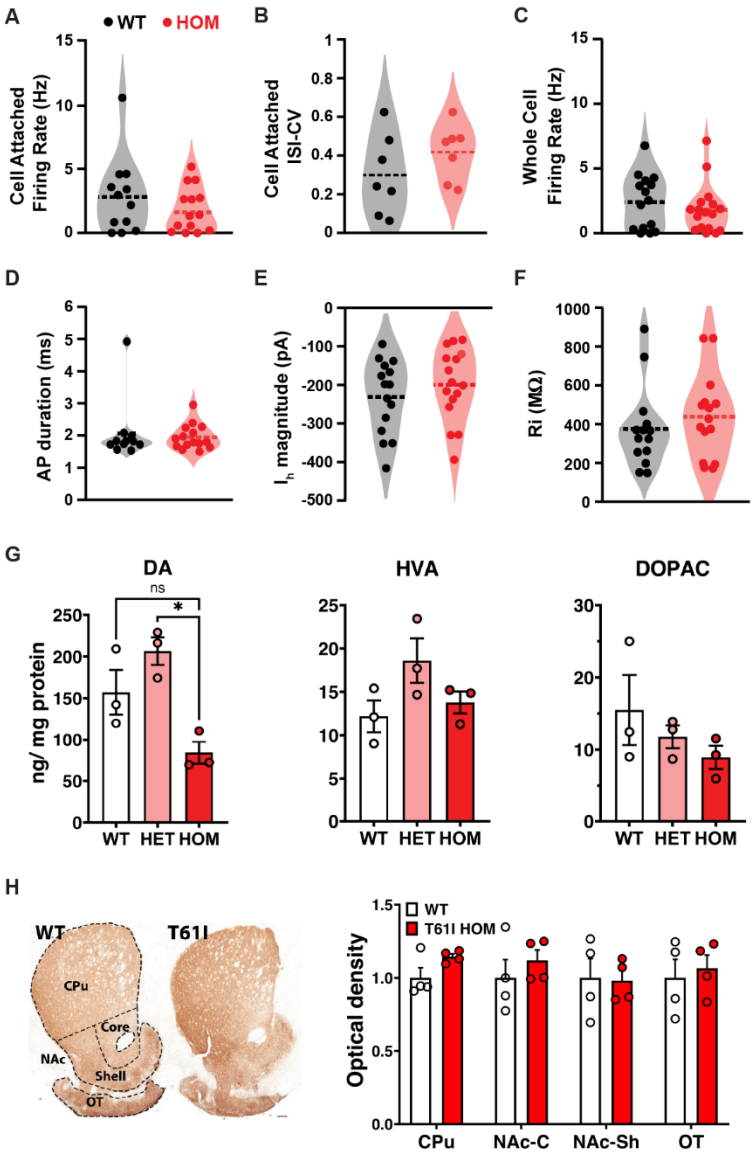

SFigure 3.2: Most physiological properties of SNc DA neurons and dopamine level are not strongly altered in CHCHD2 T61I mice. (A, B) Spontaneous firing rate and firing regularity were measured in cell attached mode. ISI-CV, coefficient of variation of interspike intervals. **(C)** Spontaneous firing rate was also measured in current clamp mode immediately after whole cell access was established. **(D)** Spontaneous AP waveforms collected in whole cell current clamp configuration. AP duration was measured from threshold to recrossing threshold during repolarization. AP, action potential. **(E)** I_h magnitude was measured in whole cell voltage clamp configuration, Vholding = -60 stepping to -120 mV. **(F)** Input resistance was measured in whole cell current clamp mode. N = 5 WT and 4 HOM male mice at 23 months. Data represent mean ± SEM or with kernel density estimations. For all data parametric assumptions were tested to choose between t-test (parametric) or permutation (non-parametric) analysis. *P < 0.05. **(G)** HPLC of CPu punches from flash-frozen brain tissues at 16 months showed trending lower DA level in T61I HOM mice (P = 0.071). Data represent mean ± SEM. N = 3 mice/genotype. *P < 0.05 by one-way ANOVA with Dunnett's *post hoc* test. **(H)** Representative images of TH immunoreactivity in striatal sections at 23 months. DA neuron projection areas in dorsal and

ventral striatum are indicated with dotted lines. CPu, caudate putamen; NAc, nucleus accumbens; OT, olfactory tubercule. Quantification for TH immunoreactivity showed no difference in WT, HET and HOM by two-way ANOVA with Tukey's *post hoc* test. N = 4 animals/group. Data represent mean ± SEM. Scale bar indicates 300 µm.

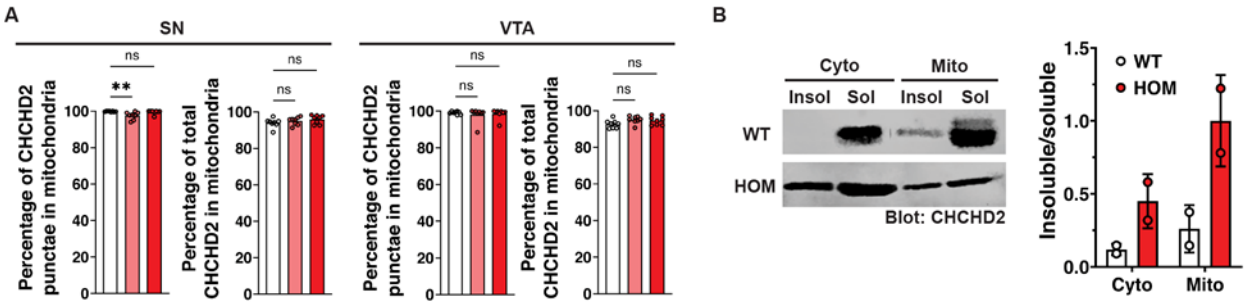

SFigure 3.3: Soluble and insoluble T61I CHCHD2 localizes to mitochondria. (A) Proportion of CHCHD2 punctae and total CHCHD2 that localizes to the mitochondria in the SN and VTA. N = 6 - 8 randomly selected TH-positive cells from 6 fields in each region in each mouse, 2 mice/gender/genotype. Data represent mean ± SEM. **P* < 0.05, ***P* < 0.01, ****P* < 0.001 by one-way ANOVA with Tukey's *post hoc* test. **(B)** Representative image of CHCHD2 western blot (left panel). CHCHD2 T61I mutation increased insolubility particularly in the mitochondrial fraction of brain lysate (right panel). N = 2 mice per genotype at 16 months from 2 independent experiments.

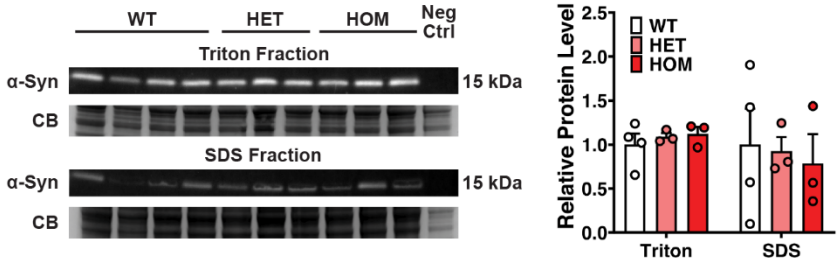

SFigure 3.4: T61I CHCHD2 mutant does not lead to changes in total and phosphorylated α-synuclein expression in the cortex. Gel images (left) and quantification (right) of western blot against α-synuclein in Triton-soluble and SDS-soluble fractions of frontal cortex lysate showed no changes in T61I mice at 16 months. A negative control (α-synuclein KO mouse) was included. CB, Coomassie brilliant blue staining as a loading control. α-synuclein level was normalized to total protein content by Coomassie brilliant blue staining. N = 4 WT, 3 HET and 3 HOM. Data represent mean ± SEM.

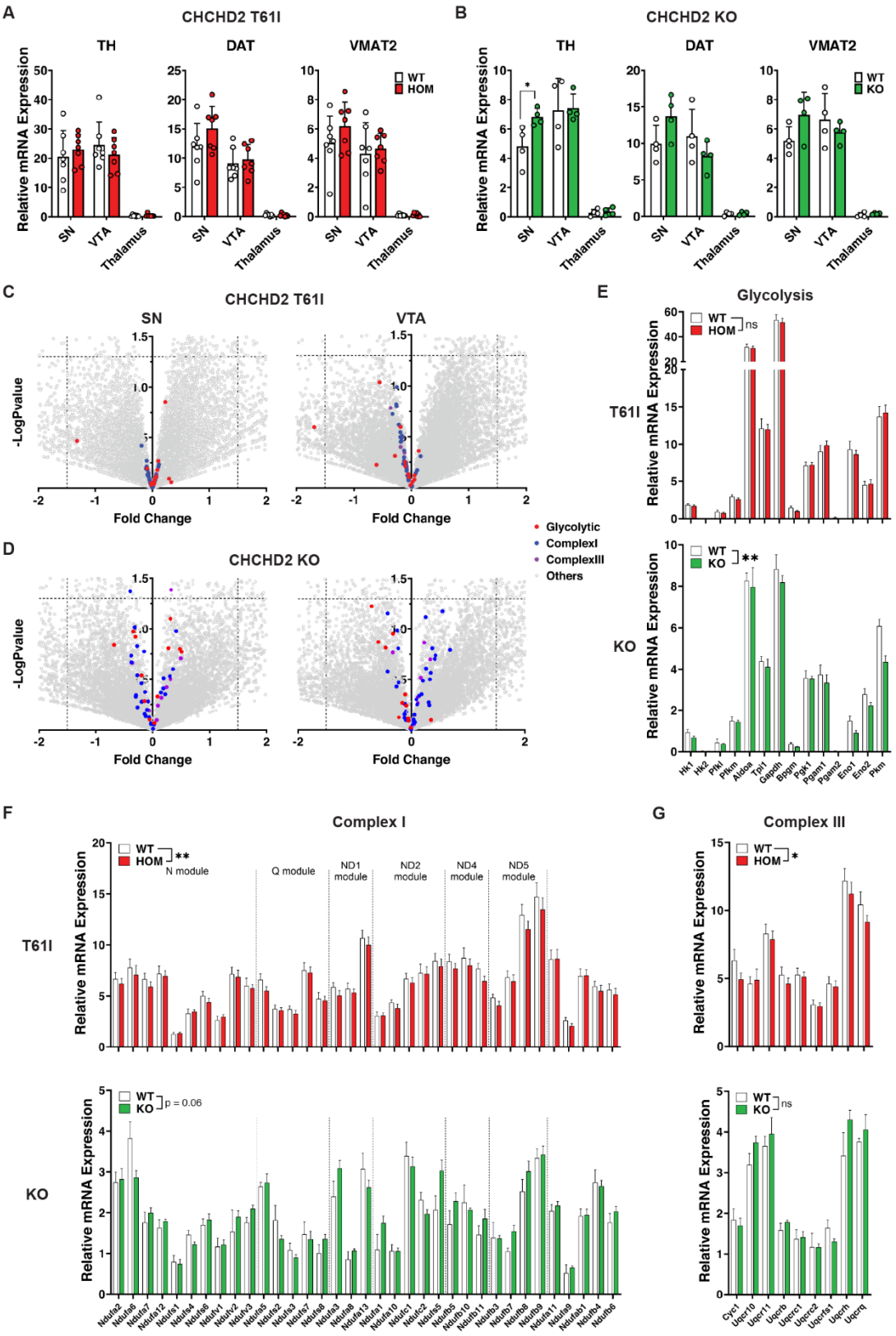

SFigure 3.5: T61I CHCHD2 VTA DA neurons have decreased expression of Complex I and III genes by Spatial Transcriptomics. Snap-frozen brain sections of CHCHD2 T61I and KO mice

were analyzed by the Visium spatial transcriptomics kit. **(A, B)** Expression of DA neuron markers are confined to spatial regions. A, CHCHD2 T61I; B, CHCHD2 KO. **(C, D)** Volcano plots showing selected metabolic pathways including glycolytic, complex I and complex III genes in the SN (left) and VTA (right) of CHCHD2 T61I (C) and KO (D) mice. **(E)** Bar graphs of glycolytic gene expression of CHCHD2 T61I (up) and CHCHD2 KO (down) mice. The CHCHD2 KO mice showed a significant downregulation of glycolytic genes. **(F)** Bar graphs of complex I component expression of CHCHD2 T61I (up) and CHCHD2 KO (down) mice. CHCHD2 T61I mice exhibited decreased level of nearly all complex I subunits. **(G)** Bar graphs of complex III component expression of CHCHD2 T61I (up) and CHCHD2 KO (down) mice. CHCHD2 T61I mice showed decreased expression of almost all complex III subunits. N = 7 homozygous CHCHD2 T61I mice and 7 littermate controls at 16 months and 4 homozygous CHCHD2 KO and 4 littermate controls at 13 months. In all bar graphs (A, B, E-G), data represent mean ± SEM. **P* < 0.05, ***P* < 0.01 by 2-way ANOVA with Sidak *post hoc* test.

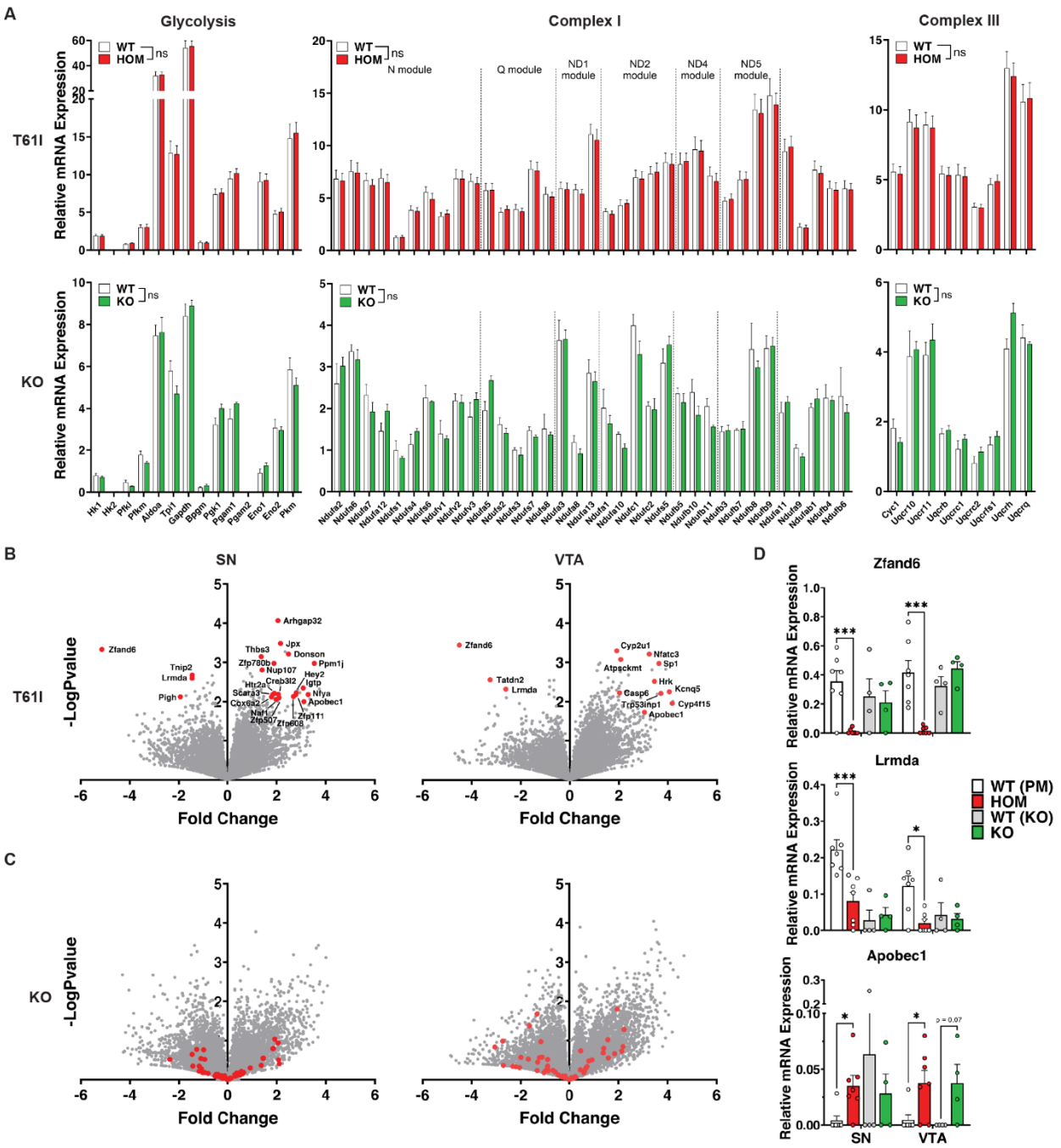

SFigure 3.6: Distinct mechanisms are implied by individual hits observed in CHCHD2 T61I and KO mice. Spatial transcriptomics analyses on snap-frozen brain sections of CHCHD2 T61I and KO mice. **(A)** Changes in metabolic pathways were not replicated in SN DA neurons in CHCHD2 T61I (up) and KO (down) mice. **(B)** Volcano plots highlighting the top 20 percent individual hits in the SN (left) and VTA (right) of CHCHD2 T61I mice. **(C)** Volcano plots highlighting the individual hits identified in the T61I mice in the SN (left) and VTA (right) of CHCHD2 KO mice. None of the hits was within the top 20 percent in the KO mice. **(D)** Bar graphs of the 3 common hits in the SN and VTA of the T61I mice, which were unaffected in the CHCHD2 KO mice. N = 7 homozygous CHCHD2 T61I mice and 7 littermate controls at 16 months and 4 homozygous

CHCHD2 KO and 4 littermate controls at 13 months. Data represent mean ± SEM in all bar graphs (A, D). *P < 0.05, ***P < 0.001 by unpaired t-test in D.

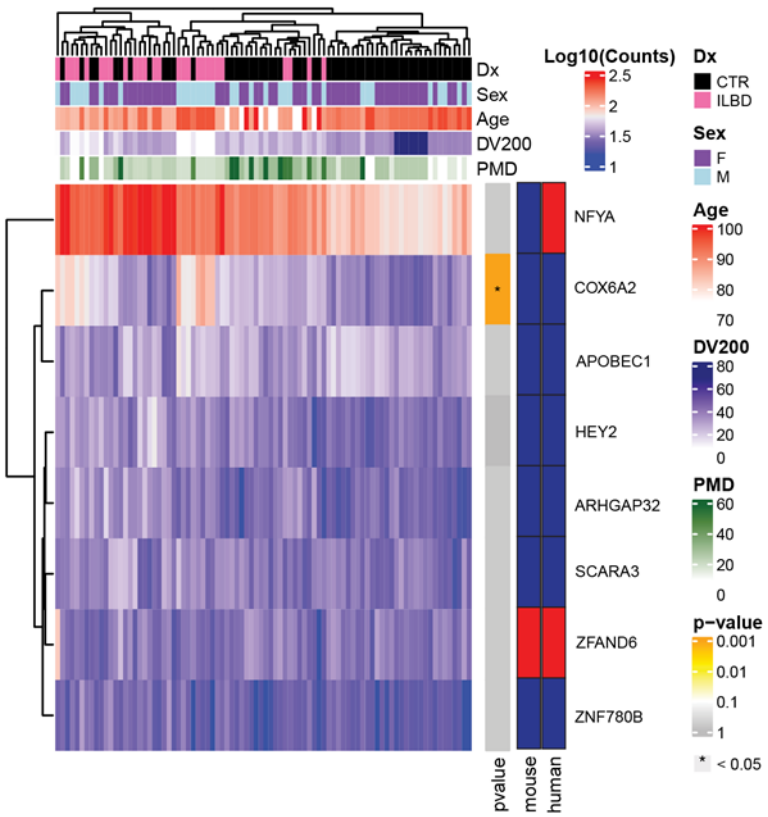

SFigure 3.7: Differentially expressed genes in the CHCHD2 T61I mice are altered in similar trends in sporadic PD. Heatmap of normalized gene expression (per region of interest) values from GeoMx spatial transcriptomic analysis of human SNc ventral tier dopamine neurons (TH+) within 8 DEG's and identified within the CHCHD2 T61I mouse model. 'Limma voom' methodology was used to assess differential gene expression between control and PD samples. PMD, post-mortem delay; DV200, RNA integrity number equivalent. *P < 0.05.

Chapter 4: Concluding Remarks

The world is experiencing an inevitable trend of population aging, which is a major risk factor for numerous diseases, including neurodegenerative diseases such as Alzheimer's disease and Parkinson's disease. Currently, there are few, if any, effective treatments available for age-related neurodegenerative diseases [84]. Among the various factors contributing to aging, mitochondrial dysfunction has emerged a key hallmark [85]. Since mitochondria are central in the regulation of energy and metabolic homeostasis, understanding whether energy failure is a direct contributor to neurodegenerative diseases is crucial. Additionally, the role of glycolysis in the progression of energy failure is significant. Growing evidence indicates a notable metabolic reprogramming toward glycolysis in several tissues [86-88], including in Alzheimer's and Parkinson's disease. This thesis, through two projects, aims to improve our understanding of the mechanisms through which cells maintain energy balance and the causative relationship between energy failure and neurodegeneration.

In chapter 2, we developed two complementary CRISPRi screenings involving the concurrent inhibition or activation of *HIF1A* on top of a library to delineate its mechanism. This approach enables the identification of HIF1-dependent genes and their downstream/upstream position relative to HIF1, and provides valuable insight into HIF1's normoxic repression of mitochondrial respiration. We discovered the HIF1 pathway diverts the substrate flux toward lactate even under normoxia, and may be required for the direct entry of pyruvate into the TCA cycle, contrary to the common assumption of its inactivation. Additionally, the identification of tau and other glycolytic enzymes as necessary components in HIF1's substrate divergence suggests a strong association between energy failure and neurodegenerative diseases. These findings fill in knowledge gaps regarding the mechanisms of intracellular energy homeostasis, emphasizing the central role of HIF1 in the intersection between glycolysis and respiration, and highlighting the potential of targeting HIF1 and tau for therapeutic interventions for a broad spectrum of energy failure-related diseases.

In chapter 3, we generated a new mouse model with a point mutation in the Parkinsonian gene CHCHD2, which recapitulates the hallmarks of sporadic Parkinson's disease in humans. This model exhibits protein aggregation selectively in the substantia nigra (SN), a region particularly vulnerable to PD progression, where a specific subpopulation of dopaminergic (DA) neurons degenerates first. Using spatial transcriptomics and proteomics, we observed that the protein accumulation primarily impacts mitochondria, leading to a robust metabolic shift toward glycolysis. Furthermore, the mice exhibit phosphorylation and likely aggregation of α-synuclein in the DA neurons, another hallmark of sporadic PD in humans, observed for the first time in monogenic PD mouse models. These findings address two major elusive questions in PD research: the causal link between mitochondrial failure and PD pathogenesis, and the selective vulnerability of SN DA neurons.

In summary, this thesis advances our understanding of energy metabolism, a universal function in all cell types of the body crucial for maintaining a healthy lifespan. It also highlights a fundamental cause of Parkinson's disease development. I believe this study makes a meaningful contribution to human society, with the potential to significantly impact the development of therapeutic interventions.

References

1. Amorim, J.A., et al., *Mitochondrial and metabolic dysfunction in ageing and age-related diseases.* Nat Rev Endocrinol, 2022. **18**(4): p. 243-258.
2. Wallace, D.C., *A mitochondrial paradigm of metabolic and degenerative diseases, aging, and cancer: a dawn for evolutionary medicine.* Annu Rev Genet, 2005. **39**: p. 359-407.
3. Guo, J., et al., *Aging and aging-related diseases: from molecular mechanisms to interventions and treatments.* Signal Transduct Target Ther, 2022. **7**(1): p. 391.
4. Yellen, G., *Fueling thought: Management of glycolysis and oxidative phosphorylation in neuronal metabolism.* J Cell Biol, 2018. **217**(7): p. 2235-2246.
5. Kang, H., et al., *PARIS reprograms glucose metabolism by HIF-1alpha induction in dopaminergic neurodegeneration.* Biochem Biophys Res Commun, 2018. **495**(4): p. 2498-2504.
6. Zhang, X., N. Alshakhshir, and L. Zhao, *Glycolytic Metabolism, Brain Resilience, and Alzheimer's Disease.* Front Neurosci, 2021. **15**: p. 662242.
7. Collaborators, G.B.D.P.s.D., *Global, regional, and national burden of Parkinson's disease, 1990-2016: a systematic analysis for the Global Burden of Disease Study 2016.* Lancet Neurol, 2018. **17**(11): p. 939-953.
8. Chen, C., D.M. Turnbull, and A.K. Reeve, *Mitochondrial Dysfunction in Parkinson's Disease-Cause or Consequence?* Biology (Basel), 2019. **8**(2).
9. Bolam, J.P. and E.K. Pissadaki, *Living on the edge with too many mouths to feed: why dopamine neurons die.* Mov Disord, 2012. **27**(12): p. 1478-83.
10. Surmeier, D.J., J.A. Obeso, and G.M. Halliday, *Selective neuronal vulnerability in Parkinson disease.* Nat Rev Neurosci, 2017. **18**(2): p. 101-113.
11. Haddad, D. and K. Nakamura, *Understanding the susceptibility of dopamine neurons to mitochondrial stressors in Parkinson's disease.* FEBS Lett, 2015. **589**(24 Pt A): p. 3702-13.
12. Tanner, C.M., et al., *Rotenone, paraquat, and Parkinson's disease.* Environ Health Perspect, 2011. **119**(6): p. 866-72.
13. Przedborski, S., et al., *The parkinsonian toxin 1-methyl-4-phenyl-1,2,3,6-tetrahydropyridine (MPTP): a technical review of its utility and safety.* J Neurochem, 2001. **76**(5): p. 1265-74.
14. Kitada, T., et al., *Mutations in the parkin gene cause autosomal recessive juvenile parkinsonism.* Nature, 1998. **392**(6676): p. 605-8.
15. Valente, E.M., et al., *Hereditary early-onset Parkinson's disease caused by mutations in PINK1.* Science, 2004. **304**(5674): p. 1158-60.
16. Bonifati, V., et al., *Mutations in the DJ-1 gene associated with autosomal recessive early-onset parkinsonism.* Science, 2003. **299**(5604): p. 256-9.
17. Funayama, M., et al., *CHCHD2 mutations in autosomal dominant late-onset Parkinson's disease: a genome-wide linkage and sequencing study.* Lancet Neurol, 2015. **14**(3): p. 274-82.
18. Kruger, R., et al., *Ala30Pro mutation in the gene encoding alpha-synuclein in Parkinson's disease.* Nat Genet, 1998. **18**(2): p. 106-8.
19. Polymeropoulos, M.H., et al., *Mutation in the alpha-synuclein gene identified in families with Parkinson's disease.* Science, 1997. **276**(5321): p. 2045-7.

20. Zarranz, J.J., et al., *The new mutation, E46K, of alpha-synuclein causes Parkinson and Lewy body dementia.* Ann Neurol, 2004. **55**(2): p. 164-73.
21. Zimprich, A., et al., *Mutations in LRRK2 cause autosomal-dominant parkinsonism with pleomorphic pathology.* Neuron, 2004. **44**(4): p. 601-7.
22. Schapira, A.H., et al., *Mitochondrial complex I deficiency in Parkinson's disease.* J Neurochem, 1990. **54**(3): p. 823-7.
23. Elstner, M., et al., *Expression analysis of dopaminergic neurons in Parkinson's disease and aging links transcriptional dysregulation of energy metabolism to cell death.* Acta Neuropathol, 2011. **122**(1): p. 75-86.
24. Zheng, B., et al., *PGC-1alpha, a potential therapeutic target for early intervention in Parkinson's disease.* Sci Transl Med, 2010. **2**(52): p. 52ra73.
25. Bender, A., et al., *High levels of mitochondrial DNA deletions in substantia nigra neurons in aging and Parkinson disease.* Nat Genet, 2006. **38**(5): p. 515-7.
26. Mendelsohn, B.A., et al., *A high-throughput screen of real-time ATP levels in individual cells reveals mechanisms of energy failure.* PLoS Biol, 2018. **16**(8): p. e2004624.
27. Bennett, N.K., et al., *Defining the ATPome reveals cross-optimization of metabolic pathways.* Nat Commun, 2020. **11**(1): p. 4319.
28. Iyer, N.V., et al., *Cellular and developmental control of O2 homeostasis by hypoxia-inducible factor 1 alpha.* Genes Dev, 1998. **12**(2): p. 149-62.
29. Kim, J.W., et al., *HIF-1-mediated expression of pyruvate dehydrogenase kinase: a metabolic switch required for cellular adaptation to hypoxia.* Cell Metab, 2006. **3**(3): p. 177-85.
30. Papandreou, I., et al., *HIF-1 mediates adaptation to hypoxia by actively downregulating mitochondrial oxygen consumption.* Cell Metab, 2006. **3**(3): p. 187-97.
31. Courtnay, R., et al., *Cancer metabolism and the Warburg effect: the role of HIF-1 and PI3K.* Mol Biol Rep, 2015. **42**(4): p. 841-51.
32. Semenza, G.L., et al., *Hypoxia-inducible nuclear factors bind to an enhancer element located 3' to the human erythropoietin gene.* Proc Natl Acad Sci U S A, 1991. **88**(13): p. 5680-4.
33. Firth, J.D., B.L. Ebert, and P.J. Ratcliffe, *Hypoxic regulation of lactate dehydrogenase A. Interaction between hypoxia-inducible factor 1 and cAMP response elements.* J Biol Chem, 1995. **270**(36): p. 21021-7.
34. Masoud, G.N. and W. Li, *HIF-1alpha pathway: role, regulation and intervention for cancer therapy.* Acta Pharm Sin B, 2015. **5**(5): p. 378-89.
35. Semenza, G.L., *Hypoxia-inducible factor 1 and cardiovascular disease.* Annu Rev Physiol, 2014. **76**: p. 39-56.
36. Trayhurn, P., B. Wang, and I.S. Wood, *Hypoxia in adipose tissue: a basis for the dysregulation of tissue function in obesity?* Br J Nutr, 2008. **100**(2): p. 227-35.
37. Burtscher, J., et al., *Hypoxia and brain aging: Neurodegeneration or neuroprotection?* Ageing Res Rev, 2021. **68**: p. 101343.
38. Yeo, E.J., *Hypoxia and aging.* Exp Mol Med, 2019. **51**(6): p. 1-15.
39. Ullah, M.S., A.J. Davies, and A.P. Halestrap, *The plasma membrane lactate transporter MCT4, but not MCT1, is up-regulated by hypoxia through a HIF-1alpha-dependent mechanism.* J Biol Chem, 2006. **281**(14): p. 9030-7.

40. Wang, D., et al., *Hypoxia induces lactate secretion and glycolytic efflux by downregulating mitochondrial pyruvate carrier levels in human umbilical vein endothelial cells.* Mol Med Rep, 2018. **18**(2): p. 1710-1717.
41. Zhu, Y., et al., *The long noncoding RNA glycoLINC assembles a lower glycolytic metabolon to promote glycolysis.* Mol Cell, 2022. **82**(3): p. 542-554 e6.
42. Kierans, S.J., et al., *Hypoxia induces a glycolytic complex in intestinal epithelial cells independent of HIF-1-driven glycolytic gene expression.* Proc Natl Acad Sci U S A, 2023. **120**(35): p. e2208117120.
43. Tracy, T.E., et al., *Tau interactome maps synaptic and mitochondrial processes associated with neurodegeneration.* Cell, 2022. **185**(4): p. 712-728 e14.
44. Huang, X., L. Zhao, and R. Peng, *Hypoxia-Inducible Factor 1 and Mitochondria: An Intimate Connection.* Biomolecules, 2022. **13**(1).
45. Ahlskog, J.E., *Parkin and PINK1 parkinsonism may represent nigral mitochondrial cytopathies distinct from Lewy body Parkinson's disease.* Parkinsonism Relat Disord, 2009. **15**(10): p. 721-7.
46. Ikeda, A., et al., *Mutations in CHCHD2 cause alpha-synuclein aggregation.* Hum Mol Genet, 2019. **28**(23): p. 3895-3911.
47. Huang, X., et al., *CHCHD2 accumulates in distressed mitochondria and facilitates oligomerization of CHCHD10.* Hum Mol Genet, 2018. **27**(22): p. 3881-3900.
48. Meng, H., et al., *Loss of Parkinson's disease-associated protein CHCHD2 affects mitochondrial crista structure and destabilizes cytochrome c.* Nat Commun, 2017. **8**: p. 15500.
49. Zhou, W., et al., *PD-linked CHCHD2 mutations impair CHCHD10 and MICOS complex leading to mitochondria dysfunction.* Hum Mol Genet, 2019. **28**(7): p. 1100-1116.
50. Nguyen, M.K., et al., *Mouse midbrain dopaminergic neurons survive loss of the PD-associated mitochondrial protein CHCHD2.* Hum Mol Genet, 2022. **31**(9): p. 1500-1518.
51. Sato, S., et al., *Homeostatic p62 levels and inclusion body formation in CHCHD2 knockout mice.* Hum Mol Genet, 2021. **30**(6): p. 443-453.
52. Anderson, C.J., et al., *ALS/FTD mutant CHCHD10 mice reveal a tissue-specific toxic gain-of-function and mitochondrial stress response.* Acta Neuropathol, 2019. **138**(1): p. 103-121.
53. Torii, S., et al., *Involvement of casein kinase 1 epsilon/delta (Csnk1e/d) in the pathogenesis of familial Parkinson's disease caused by CHCHD2.* EMBO Mol Med, 2023. **15**(9): p. e17451.
54. Hikima, T., et al., *Activity-dependent somatodendritic dopamine release in the substantia nigra autoinhibits the releasing neuron.* Cell Rep, 2021. **35**(1): p. 108951.
55. Burstein, S.R., et al., *In vitro and in vivo studies of the ALS-FTLD protein CHCHD10 reveal novel mitochondrial topology and protein interactions.* Hum Mol Genet, 2018. **27**(1): p. 160-177.
56. Straub, I.R., et al., *Loss of CHCHD10-CHCHD2 complexes required for respiration underlies the pathogenicity of a CHCHD10 mutation in ALS.* Hum Mol Genet, 2018. **27**(1): p. 178-189.

57. Eustaquio, T., et al., *Electron microscopy techniques employed to explore mitochondrial defects in the developing rat brain following ketamine treatment.* Exp Cell Res, 2018. **373**(1-2): p. 164-170.
58. Stefanis, L., *alpha-Synuclein in Parkinson's disease.* Cold Spring Harb Perspect Med, 2012. **2**(2): p. a009399.
59. Motori, E., et al., *Neuronal metabolic rewiring promotes resilience to neurodegeneration caused by mitochondrial dysfunction.* Sci Adv, 2020. **6**(35): p. eaba8271.
60. Gonzalez-Rodriguez, P., et al., *Disruption of mitochondrial complex I induces progressive parkinsonism.* Nature, 2021. **599**(7886): p. 650-656.
61. Sayles, N.M., et al., *Mutant CHCHD10 causes an extensive metabolic rewiring that precedes OXPHOS dysfunction in a murine model of mitochondrial cardiomyopathy.* Cell Rep, 2022. **38**(10): p. 110475.
62. Chang, E.J., et al., *AWP1 binds to tumor necrosis factor receptor-associated factor 2 (TRAF2) and is involved in TRAF2-mediated nuclear factor-kappaB signaling.* Int J Biochem Cell Biol, 2011. **43**(11): p. 1612-20.
63. Diatchenko, L., et al., *Identification of novel mediators of NF-kappaB through genome-wide survey of monocyte adherence-induced genes.* J Leukoc Biol, 2005. **78**(6): p. 1366-77.
64. Fenner, B.J., M. Scannell, and J.H. Prehn, *Identification of polyubiquitin binding proteins involved in NF-kappaB signaling using protein arrays.* Biochim Biophys Acta, 2009. **1794**(7): p. 1010-6.
65. Cole, D.C., et al., *Loss of APOBEC1 RNA-editing function in microglia exacerbates age-related CNS pathophysiology.* Proc Natl Acad Sci U S A, 2017. **114**(50): p. 13272-13277.
66. Zilocchi, M., et al., *Co-fractionation-mass spectrometry to characterize native mitochondrial protein assemblies in mammalian neurons and brain.* Nat Protoc, 2023. **18**(12): p. 3918-3973.
67. Marder, K.S., et al., *Predictors of parkin mutations in early-onset Parkinson disease: the consortium on risk for early-onset Parkinson disease study.* Arch Neurol, 2010. **67**(6): p. 731-8.
68. Al-Rumayyan, A., C. Klein, and M. Alfadhel, *Early-Onset Parkinsonism: Case Report and Review of the Literature.* Pediatr Neurol, 2017. **67**: p. 102-106 e1.
69. Fan, L., et al., *CHCHD2 p.Thr61Ile knock-in mice exhibit motor defects and neuropathological features of Parkinson's disease.* Brain Pathol, 2023. **33**(3): p. e13124.
70. Kee, T.R., et al., *Pathological characterization of a novel mouse model expressing the PD-linked CHCHD2-T61I mutation.* Hum Mol Genet, 2022. **31**(23): p. 3987-4005.
71. Cheng, F., et al., *DJ-1 is dispensable for human stem cell homeostasis.* Protein Cell, 2019. **10**(11): p. 846-853.
72. Ariga, H., et al., *Neuroprotective function of DJ-1 in Parkinson's disease.* Oxid Med Cell Longev, 2013. **2013**: p. 683920.
73. Clark, E.H., et al., *Targeting mitophagy in Parkinson's disease.* J Biol Chem, 2021. **296**: p. 100209.

74. Johnson, E.C.B., et al., *Behavioral and neural network abnormalities in human APP transgenic mice resemble those of App knock-in mice and are modulated by familial Alzheimer's disease mutations but not by inhibition of BACE1.* Mol Neurodegener, 2020. **15**(1): p. 53.
75. Deacon, R.M., *Measuring motor coordination in mice.* J Vis Exp, 2013(75): p. e2609.
76. Hnasko, T.S., et al., *Vesicular glutamate transport promotes dopamine storage and glutamate corelease in vivo.* Neuron, 2010. **65**(5): p. 643-56.
77. Fu, Y., et al., *A cytoarchitectonic and chemoarchitectonic analysis of the dopamine cell groups in the substantia nigra, ventral tegmental area, and retrorubral field in the mouse.* Brain Struct Funct, 2012. **217**(2): p. 591-612.
78. Stojkovska, I. and J.R. Mazzulli, *Detection of pathological alpha-synuclein aggregates in human iPSC-derived neurons and tissue.* STAR Protoc, 2021. **2**(1): p. 100372.
79. Moutaoufik, M.T., et al., *Rewiring of the Human Mitochondrial Interactome during Neuronal Reprogramming Reveals Regulators of the Respirasome and Neurogenesis.* iScience, 2019. **19**: p. 1114-1132.
80. Gibbels, E., *[Hitler's Parkinson syndrome. A posthumous motility analysis of film records of the German Weekly News 1940-1945].* Nervenarzt, 1988. **59**(9): p. 521-8.
81. Braak, H., et al., *Staging of brain pathology related to sporadic Parkinson's disease.* Neurobiol Aging, 2003. **24**(2): p. 197-211.
82. Halliday, G.M., K. Del Tredici, and H. Braak, *Critical appraisal of brain pathology staging related to presymptomatic and symptomatic cases of sporadic Parkinson's disease.* J Neural Transm Suppl, 2006(70): p. 99-103.
83. Malty, R.H., et al., *A Map of Human Mitochondrial Protein Interactions Linked to Neurodegeneration Reveals New Mechanisms of Redox Homeostasis and NF-kappaB Signaling.* Cell Syst, 2017. **5**(6): p. 564-577 e12.
84. Hou, Y., et al., *Ageing as a risk factor for neurodegenerative disease.* Nat Rev Neurol, 2019. **15**(10): p. 565-581.
85. Srivastava, S., *The Mitochondrial Basis of Aging and Age-Related Disorders.* Genes (Basel), 2017. **8**(12).
86. Feng, Z., et al., *Reprogramming of energy metabolism as a driver of aging.* Oncotarget, 2016. **7**(13): p. 15410-20.
87. Ma, Y. and J. Li, *Metabolic shifts during aging and pathology.* Compr Physiol, 2015. **5**(2): p. 667-86.
88. Ravera, S., et al., *Discrete Changes in Glucose Metabolism Define Aging.* Sci Rep, 2019. **9**(1): p. 10347.